Electronic properties of novel topological quantum materials studied by angle-resolved photoemission spectroscopy (ARPES)

by

Yun Wu

A dissertation submitted to the graduate faculty
in partial fulfillment of the requirements for the degree of
DOCTOR OF PHILOSOPHY

Major: Condensed Matter Physics

Program of Study Committee:
Adam Kaminski, Major Professor
Paul C. Canfield
Patricia A. Thiel
Jigang Wang
Sanjeevi Sivasankar

Iowa State University

Ames, Iowa

2016

DEDICATION

To my dear parents, lovely wife, and precious boy.

TABLE OF CONTENTS

LIST OF TABLES

LIST OF FIGURES

ACKNOWLEDGEMENTS

I would like to express my sincere gratitude to those who have helped me along my life and especially my PhD career. Without all the support, I would not have had such a wonderful five years in Ames, whose spring is green with life, summer is hot with passion, fall is rich and colorful, and winter is white and peaceful.

First of all, I would like to offer my special thanks to my advisor Dr. Adam Kaminski. His desire for perfection and eager for novel techniques have ensured the success of our lab and my completion of PhD study. His guidance in ARPES research has led me into this wonderful world of electronic structures. Not only does he provide great insights to keep us on the frontiers of current research, but also give us unlimited freedom to pursue the topics that we are interested in. Whenever I feel lost, his saying that"we have tons of samples" would help me lift my spirit and open my eyes for the beauty (of a sample) that has not caught my attention before. Just as Auguste Rodin stated: "Beauty is everywhere. It is not that she is lacking to our eye, but our eyes which fail to perceive her". Besides the great guidance in research, his unconditional support for me to explore new path in my career has helped me to learn the true desire of myself. To him, I owe my deepest gratitude.

I would like to thank Dr. Paul C. Canfield for providing great feedbacks for all the publications, from which I have learned a lot. Furthermore, sharing his professional experience and providing guidance for my future career would surely benefit me throughout my whole life.

I would also like to thank other committee members: Dr. Patricia A. Thiel, Dr. Jigang Wang, and Dr. Sanjeevi Sivasankar. Without their help, I could not have finished this work. My special thanks are extended to Dr. Ralph E. Napolitano, who stepped in at the last minute to ensure the success of my final thesis defense.

I would like express my great appreciation to all the group members. Dr. Rui Jiang, Dr. Daixiang Mou, and Dr. Rejendra Dhaka have helped me learn how to use the laboratory-based and the synchrotron radiation-based ARPES systems and how to interpret the ARPES results. I am especially indebted to Dr. Rui Jiang for the laptop that he has left me with, without which I could not have finished all the work and this thesis so swiftly. Dr. Lunan Huang has helped me explore new possibilities in my career. Benjamin Schrunk has helped me understand mechanics and many interesting topics in research as well as daily life.

I would like express my thanks to Dr. Sergey L. Bud'ko for the transport measurements support and great feedbacks on the publications. Without the high quality samples from Na Hyun Jo, Dr. Tai Kong, Dr. Gil Drachuck, Udhara Kaluarachchi, and Dr. Eundeok Mun, I could not have finished this thesis. The support of band structure calculations and theory from Dr. Lin-Lin Wang, Dr. Duane D. Johnson, Dr. Yongbin Lee, Dr. Xin Zhao, Dr. Masayuki Ochi, Dr. Nandini Trivedi, Dr. Ryotaro Arita, Dr. Mohit Randeria, Dr. Yuan-Ming Lu, and Timothy McCormick has ensured the wonderful work presented in this thesis. The collaborations with Dr. Kewei Sun and Dr. Matthew Kramer in SEM experiments, and the collaborators in Princeton University in ARPES measurements have benefited me a lot. Also I owe my thanks to all the professors in graduate courses: Dr. German Valencia, and *et al*, and all the friends who have always been there to support me.

My special thanks are extended to my parents Degao Wu and Chunyu Tong, my sisters Xiurong Wu and Xiuli Wu for their unconditional support and love.

Lastly but most importantly, I owe my heart to my lovely wife Xu Ding, and my precious boy Jensen D. Wu (Zhanxi Wu) who came into our world just a few hours after my PhD thesis defense.

ABSTRACT

The discovery of quantum Hall effect has motivated the use of topology instead of broken symmetry to classify the states of matter. Quantum spin Hall effect has been proposed to have a separation of spin currents as an analogue of the charge currents separation in quantum Hall effect, leading us to the era of topological insulators. Three-dimensional analogue of the Dirac state in graphene has brought us the three-dimensional Dirac states. Materials with three-dimensional Dirac states could potentially be the parent compounds for Weyl semimetals and topological insulators when time-reversal or space inversion symmetry is broken. In addition to the single Dirac point linking the two dispersion cones in the Dirac/Weyl semimetals, Dirac points can form a line in the momentum space, resulting in a topological node line semimetal. These fascinating novel topological quantum materials could provide us platforms for studying the relativistic physics in condensed matter systems and potentially lead to design of new electronic devices that run faster and consume less power than traditional, silicon based transistors.

In this thesis, we present the electronic properties of novel topological quantum materials studied by angle-resolved photoemission spectroscopy (ARPES). In Chapter 1, we will lay the ground for understanding the topological quantum states in these materials. Chapter 2 will provide an introduction to the ARPES used in research presented in this thesis. ARPES results of unpublished projects such as $Bi_2Rh_3S_2$, unpublished data such as $PtSn_4$, and other materials such as $CrAuTe_4$ will be discussed along with the description of the ARPES systems in Chapter 2. In Chapter 3, we will present the study of topological insulator (or more precisely, topological semimetal) candidate LaBi, where the Dirac cone at the Γ point is buried deeply inside the bulk spectrum and asymmetric massive states are acquired for top and bottom Dirac cones. Chapter 4 elucidates the three-dimensional Dirac state in Cd_3As_2 using fine tuning incident photon energies with energy step ~ 0.15 eV, which provides k_z dispersion with ultrahigh energy

and momentum resolutions. Type-II Weyl semimetal candidate WTe_2 displays a surprising temperature-induced Lifshitz transition. Furthermore, both “normal” and “topological” states have been observed in this material due to the fact that the electronic structure is very sensitive to strain and pressure. Detailed electronic structure of WTe_2 including the surface Fermi arcs and three-dimensional bulk states will be discussed in detail in Chapter 5. In the last chapter (Chapter 6), we will present an unusual Dirac node arc structure in $PtSn_4$ showing arcs instead of closed loops of Dirac nodes. The materials presented in this thesis are just a fraction of the known novel topological quantum materials, and more are yet to be discovered.

CHAPTER 1. INTRODUCTION

Topological quantum materials have attracted great interest since the discovery of the quantum Hall effect. Topology has been introduced for classifying the states of matter in addition to the "old fashioned" symmetry breaking. In this chapter, we will give an overview of the discovery of novel topological quantum materials such as the quantum Hall system, topological insulators, three-dimensional Dirac/Weyl semimetals, and the Dirac node line semimetals. After introducing the quantum Hall effect in graphene, we will discuss the difference between trivial insulators and quantum Hall insulators. Generalization of the quantum Hall effect to quantum spin Hall effect (topological insulator) requires, in general, strong spin-orbit coupling and band inversion. Extension of the two-dimensional Dirac states to three-dimensional systems leads to Dirac/Weyl semimetals and topological node line semimetals. We will use plentiful examples and schematics to better illustrate the properties of the topological states in these systems and to better understand the unique signatures such as Fermi arc states in an intuitive way. More details can be found in the corresponding references.

1.1 Quantum Hall Effect

Before 1980, atoms and electrons forming different states of matter, such as crystalline solids and magnets, can be classified by the symmetries they spontaneously break [1]. The crystalline solids break the continuous translational symmetry of free space; thus, the atom has to be moved by a finite distance to reach the next possible position. The magnets break the continuous rotational symmetry of free space; thus, the magnetic moments have to be aligned along certain directions. However, the quantum Hall state, discovered in 1980 [2], provided the first example of a quantum state that cannot be described by spontaneous symmetry breaking.

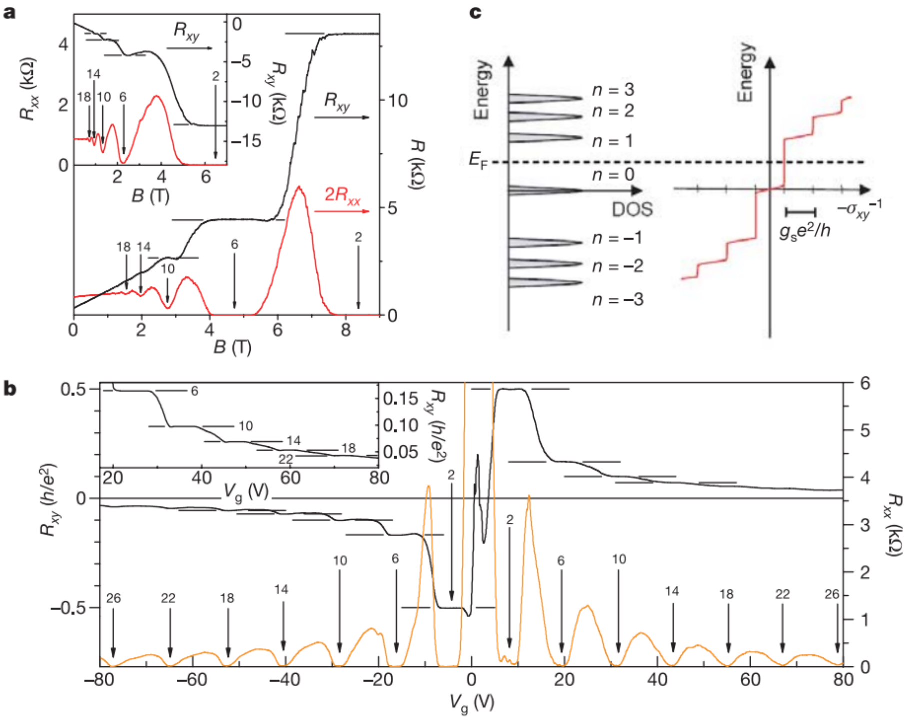

Figure 1.1 Quantized magnetoresistance and Hall resistance of a graphene device. (a) Hall resistance (black) and magnetoresistance (red) measured in the device at T = 30 mK and V_g = 15 V. The vertical arrows and the numbers on them indicate the values of B and the corresponding filling factor ν of the quantum Hall states. The horizontal lines correspond to $\nu h/e^2$ values. The inset shows the quantum Hall effect for a hole gas at V_g = -4 V, measured at 1.6 K. (b) Hall resistance (black) and magnetoresistance (orange) as a function of gate voltage at fixed magnetic field $B = 9$ T, measured at $T = 1.6$ K. The same convention as in (a) is used here. The upper inset shows a detailed view of high-filling-factor plateaux measured at 30 mK. (c) A schematic diagram of the Landau level density of states (DOS) and the corresponding quantum Hall conductance as a function of energy. (From Ref. [3]).

When placed in an environment of strong magnetic fields and low temperatures, a two-dimensional electron system will undergo the quantum Hall transition, i.e., the Hall conductance σ will become quantized:

$$\sigma = \nu \frac{e^2}{h} \tag{1.1}$$

where e is the electric charge, h is the Planck's constant, and ν is the number of quantized Landau levels that are completely filled. Since there is a gap between the filled and empty

Landau levels, the system behaves like an insulator if the Fermi energy E_F resides in the gap. However, unlike a conventional insulator, the filled Landau levels in a quantum Hall system can be continuously tuned. For example, in graphene the filled Landau levels can be tuned by varying either the applied gate voltages or magnetic fields as shown in Fig. 1.1. Fig. 1.1(c) shows a schematic diagram of the Landau level density of states (DOS) and the corresponding quantum Hall conductance as a function of energy. The Landau level index n is shown next to the DOS peak. We can see that by changing the applied gate voltage on the graphene device, the Fermi energy E_F can be tuned to cross the Landau levels, resulting in plateaus in the Hall resistance as shown in Figs. 1.1(a) and (b) [4, 3]. Furthermore, by tuning the gate voltage, two-dimensional electron and hole gas systems can be created, and both systems show quantum Hall effect as presented in the insets of panels (a) and (b). Surprisingly, the quantum Hall effect in graphene can even be observed at room temperature [5].

As explained by Thouless, Kohmoto, Nightingale, and den Nijs (TKNN) [6], the major difference between a quantum Hall state and an ordinary insulator is a matter of topology. The topological invariant, i.e., Chern invariant, can be understood in terms of the Berry phase [7] associated with the Bloch wave functions $|u_m(\mathbf{k})\rangle$. By taking the line integral of $\mathcal{A}_m = i\langle u_m|\Delta_k|u_m\rangle$ or the surface integral of the Berry flux (defined as $\mathcal{F}_m = \Delta \times \mathcal{A}_m$), the Berry phase can be calculated if there are no accidental degeneracies when $\mathbf{k}$ changed around a closed loop. Thus, the Chern invariant is the total Berry flux in the Brillouin zone

$$n_m = \frac{1}{2\pi}\int d^2\mathbf{k}\mathcal{F}_m \tag{1.2}$$

The total Chern number, $n = \sum_{m=1}^{N} n_m$, is the sum over all occupied bands m, which is invariant even if there are degeneracies between occupied bands, provided that the gap separating the occupied and empty bands remains finite. TKNN showed that the Hall conductance, calculated using the Kubo formula, has the same form, so that ν in Eq. 1.1 is identical to n. The Chern number n is a topological invariant; thus, when the Hamiltonian varies smoothly, the Chern number does not change.

To illustrate the difference between an ordinary insulator state and a quantum Hall state in a more intuitive way, we have shown the insulating and quantum Hall states in Fig. 1.2.

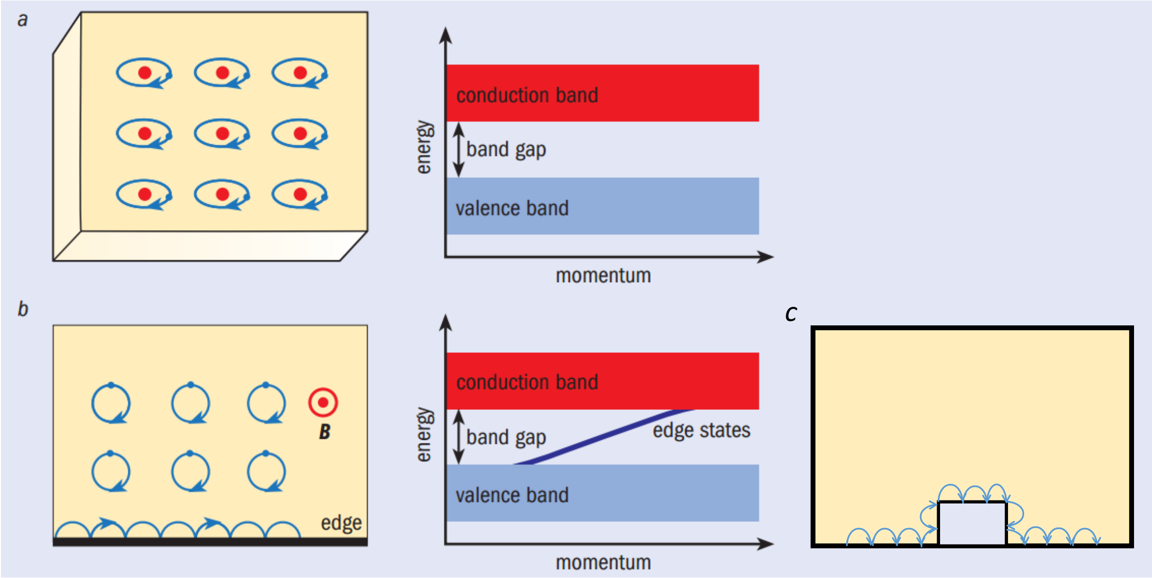

Figure 1.2 Electronic states of matter. (a) The insulating state is characterized by an energy gap separating the occupied and empty electronic states, which is a consequence of the quantization of the energy of atomic orbitals. (b) In the quantum Hall effect, the circular motion of electrons in a magnetic field, **B**, is interrupted by the sample boundary. At the edge, electrons execute "skipping orbits" as shown, ultimately leading to perfect conduction in one direction along the edge. (From Ref. [8]). (c) In the quantum Hall effect, the motion of the electrons will not be blocked by the disorder on the edge (light blue rectangular box) due to lack of back-scattering channel.

Fig. 1.2(a) shows the typical state of an insulator, where the electrons are confined due to the quantization of the atomic orbitals. Therefore, the completely empty conduction bands and completely filled valence bands are separated by a band gap and there is no conducting channel in between. On the other hand, in the quantum Hall state as shown in Fig. 1.2(b), the electrons in the bulk under a magnetic field, **B**, will be confined to the circular motions. Therefore, the bulk of the material would be insulating. However, at the edge of the system, the circular motion of the electrons are interrupted by the sample boundary. Thus, the electrons striking the boundary would bounce off and execute only half orbitals as shown at the bottom of Fig. 1.2(b), leading to perfect conduction in one direction along the edge. Due to this constrained one-direction propagation of the electrons in the quantum Hall system, there is a robustness in such system against non-magnetic disorder because there are no states available for backscattering [8]. When an edge-state electron encounters a non-magnetic disorder on the edge, it simply takes a detour and still keeps going in the same direction since there is no way for it to turn back [as shown in Fig. 1.2(c)]. This special edge state is said to be protected by the time reversal symmetry. This dissipationless transport mechanism could be extremely useful for semiconductor devices if it is not limited by the requirement of a high magnetic field [9].

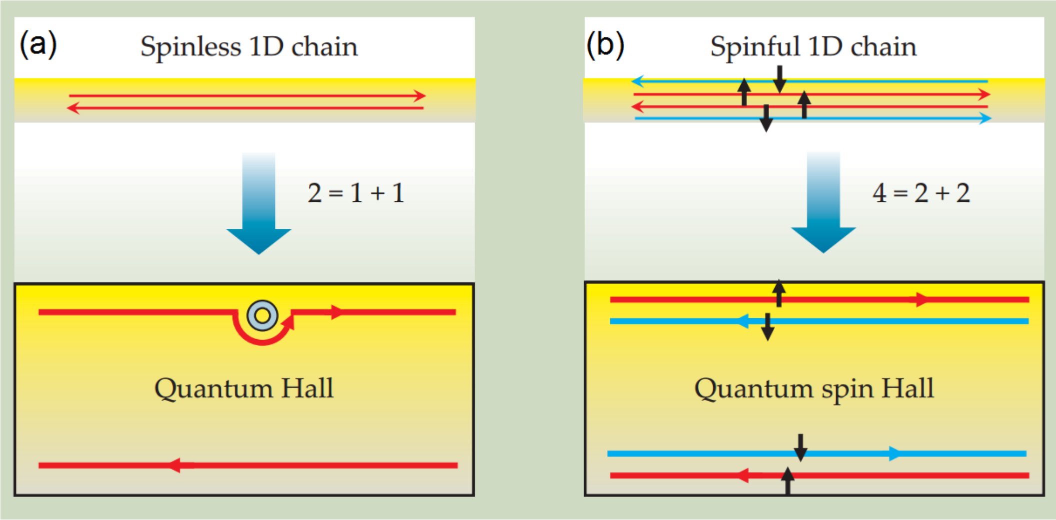

Figure 1.3 Spatial separation of the electronic states. Spatial separation is at the heart of both the quantum Hall (QH) and the quantum spin Hall (QSH) effects. (a) A spinless one-dimensional system has both a forward and a backward mover. Those two basic degrees of freedom are spatially separated in a QH bar, as illustrated by the symbolic equation "$2 = 1 + 1$". The upper edge contains only a forward mover and the lower edge has only a backward mover. The states are robust: They will go around an impurity without scattering. (b) A spinful 1D system has four basic channels, which are spatially separated in a QSH bar: The upper edge contains a forward mover with up spin and a backward mover with down spin, and conversely for the lower edge. That separation is illustrated by the symbolic equation "$4 = 2 + 2$". (From Ref. [9]).

To generalize the quantum Hall effect to a non-magnetic field case, it is important to understand the effect of applying a magnetic field in the quantum Hall transition. As shown in Fig. 1.3, in a one-dimensional world without considering spin, there are only forward and backward motions. When a strong magnetic field is applied to a two-dimensional gas of electrons at a low temperature, the electrons travel only along the edges of the system, i.e., two counterflows of electrons are spatially separated to the top and bottom edges. This can be understood as a simple charge transport separation. On the other hand, in a real one-dimensional world, the electrons propagating along one direction are composed of both spin-up and -down states. Thus, one way to mimic the charge transport separation is to have a spin transport separation. We can have the spin-up forward moving electrons and spin-down backward moving electrons stay on the top edge and the opposite case at the bottom edge. Therefore, we will have a net forward spin transport along the top edge and backward spin transport along the bottom edge. This is a quantum spin Hall state that is protected by the time reversal symmetry and immune to the non-magnetic impurities. Since there can only be odd numbers of spin-up or -down states on one edge, the quantum spin Hall state is characterized by a so-called Z_2 topological quantum number. Therefore, the quantum spin Hall insulator is synonymously referred to as a topological insulator [9]. The following section will present more details about topological insulators.

1.2 Topological Insulators

In order to realize the quantum spin Hall state, opposite spin states have to propagate in opposite directions. Such a coupling between the spin and the orbital motion is a relativistic effect most pronounced in heavy elements such as Bi, Te, and many others. In 2006, two-dimensional topological insulator states have been proposed to exist in mercury telluride (HgTe) quantum wells beyond a critical thickness [10, 11].

In common semiconductors, the spin-orbit coupling is weak and the conduction and valence bands are formed from the electrons in *s* orbitals and *p* orbitals, respectively. However, the spin-orbit coupling in heavy elements, such as Hg and Te, is large enough to push the *p*-orbital band above the *s*-orbital band, i.e., the bands are inverted. On the other hand, the CdTe layer has a weak spin-orbit coupling. Thus, by changing the thickness of the HgTe layer, the strength of the spin-orbit coupling in the quantum well can be continuously tuned, which can lead to a quantum phase transition. Fig. 1.4 shows the quantum phase transition of HgTe quantum wells from an ordinary insulator to a quantum spin Hall insulator (topological insulator) beyond the critical thickness of $d_c = 6.5$ nm. In the thin quantum well with HgTe layer thickness less than the critical value d_c, the quantum well is in the insulating state, i.e., there is a gap between the

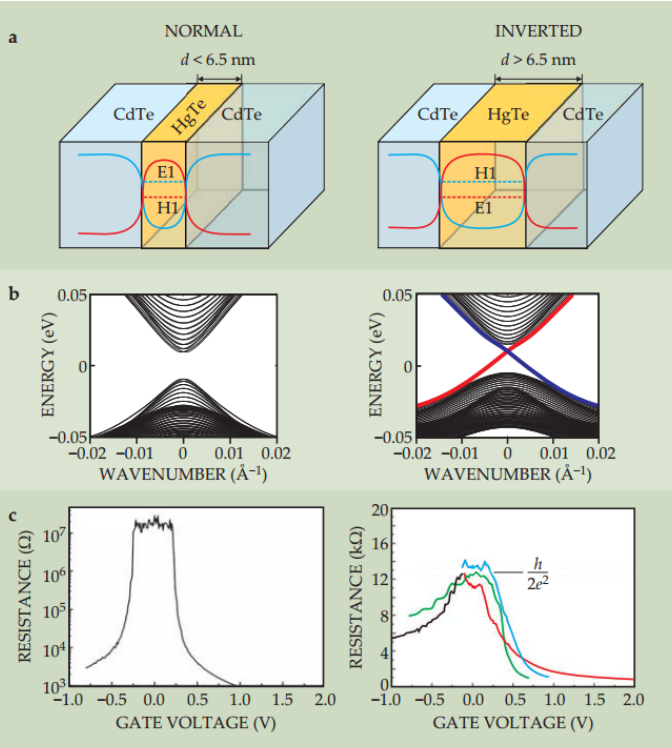

Figure 1.4 HgTe quantum wells beyond a critical thickness are two-dimensional topological insulators. (a) The behavior of a HgTe-CdTe quantum well depends on the thickness d of the HgTe layer. Here the blue curve shows the potential-energy well experienced by electrons in the conduction band; the red curve is the barrier for holes in the valence band. For thin quantum wells ($d < d_c$), the energy of the lowest-energy conduction subband (E1) is higher than that of the highest-energy valence (H1). But for $d > d_c$, those electron and hole bands are inverted. (b) The band dispersion in the quantum wells. The thin quantum well has an insulating energy gap, but inside the gap of the thick quantum well there are conducting edge states (shown by red and blue lines). (c) Transport measurements demonstrating the insulating state in the thin quantum well and the quantum spin Hall state in the thick quantum well. (From Ref. [9]).

lowest-energy conduction band (E1) and the highest-energy valence band (H1). As the thickness of the HgTe layer increases, the spin-orbit coupling strength also increases and leads to a band inversion in the quantum well, i.e., the valence band H1 is above the conduction band E1. As shown in Fig. 1.4(b), the inverted bands result in one pair of edge states carrying opposite spins and dispersing from valence band to conduction band (the red and blue lines) [9]. These two conducting channels, each contributes one quantum of conductance, e^2/h, have been observed in the quantum wells grown by molecular-beam epitaxy [12] as shown in Fig.

1.4(c). The insulating state in the thin quantum well and the quantized resistance (or quantized conductance) in the thick quantum well have demonstrated the topological phase transition in this system.

It is amazing that the quantum spin Hall state can be realized in a simple two-dimensional system, the natural question then is how we can extend this into a three-dimensional case. One way to achieve that is to stack layers of the two-dimensional quantum spin Hall insulators, which will lead to a weak topological insulator. In a weak topological insulator, the Fermi surface encloses *even* number of Dirac points in the Brillouin zone; while in a strong topological insulator, the Fermi surface encloses *odd* number of Dirac points [11]. $Bi_{1-x}Sb_x$ was the first three-dimensional material predicted to be an actual strong topological insulator [11] and was soon verified as such by angle-resolved photoemission spectroscopy (ARPES) [13]. However, due to the alloying disorder, complex surface state, and small bulk band gap in $Bi_{1-x}Sb_x$, it is hard to to be utilized as a model system for studying topological quantum phenomena. The second generation topological insulators, Bi_2Se_3, Bi_2Te_3, and Sb_2Te_3 were theoretically predicted [14] and experimentally confirmed to possess a single surface Dirac cone at the center of the Brillouin zone by ARPES measurements [15, 16, 17]. As presented in Fig. 1.3(b), the electrons with specific spins can only move along specific directions (spin-momentum locking) on the edge of a quantum spin Hall insulator (topological insulator). In order to verify that the spin of the electrons in the surface Dirac cone is “locked” to its momentum, spin-resolved ARPES measurements are required.

Fig. 1.5 shows the Fermi surface and band dispersion measured from spin- and angle-resolved photoemission spectroscopy. Fig. 1.5(a) shows the Fermi surface of $Bi_{2-\delta}Ca_\delta Se_3$ with a circular shape and the band dispersion in (c) shows a single Dirac cone structure. Similar structure can be seen in Bi_2Te_3 as shown in panels (b) and (d). By analyzing the spin-polarization of photoelectrons emitted at a binding energy of 20 meV in Bi_2Te_3, it is evident that there is no clear spin polarization signal in the x and z directions [panel (f)]. On the other hand, clear y direction polarization signals of equal magnitude and opposite sign are observed for surface-edge electrons of opposite momentum [panel (e)], demonstrating the one-to-one correspondence between the spin and momentum direction, i.e., spin-momentum locking. Fig.

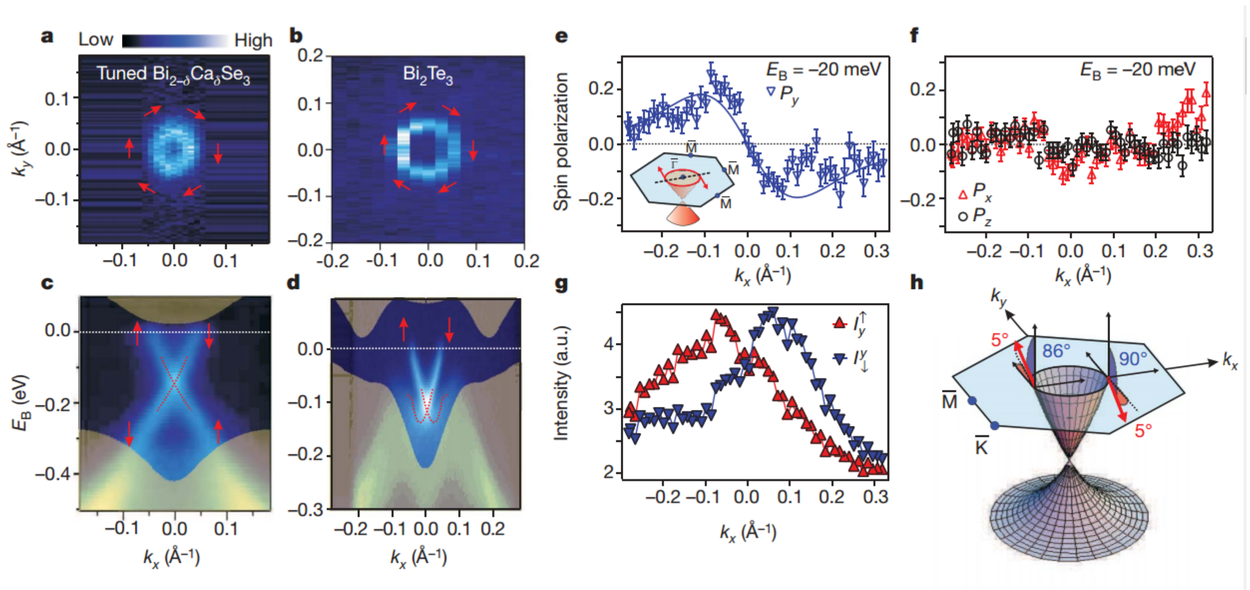

Figure 1.5 Spin-momentum locking of spin-helical Dirac electrons in topological insulators. (a) ARPES intensity map at E_F of the (111) surface of tuned $Bi_{2-\delta}Ca_\delta Se_3$ and (b) the (111) surface of Bi_2Te_3. Red arrows denote the direction of spin around the Fermi surface. (c) ARPES dispersion of tuned $Bi_{2-\delta}Ca_\delta Se_3$ and (d) Bi_2Te_3 along the k_x cut. The dotted red lines are guides to the eye. (e) Measured y component of spin polarization along the Γ-M direction at E_B =-20 meV, which only cuts through the surface states. (f) Measured x (red triangles) and z (black circles) components of spin polarization along the Γ-M direction at E_B =-20 meV. (g) Spin-resolved spectra obtained from the y component spin polarization data. (h) Fitted values of the spin polarization vector $\mathbf{P}$. (From Ref. [15]).

1.5(h) shows a schematic view of the spin-momentum-locking effect in the helical Dirac electrons with experimental angular uncertainties [15]. Interestingly, hexagonal warping effect has been discussed [18] and warped helical spin texture has been observed from circular dichroism ARPES measurements [19]. Compared to the first generation topological insulator, the second generation of these materials such as Bi_2Se_3, has several advantages: (1) the materials are stoichiometric single crystals; thus, they do not have alloying disorder; (2) the surface state is nearly idealized single Dirac cone, which is ideal for studying the topological phenomena; (3) the fairly large band gap ($\sim$ 300 meV) is suitable even for room temperature measurements and because of that these materials have potential for industrial applications [20].

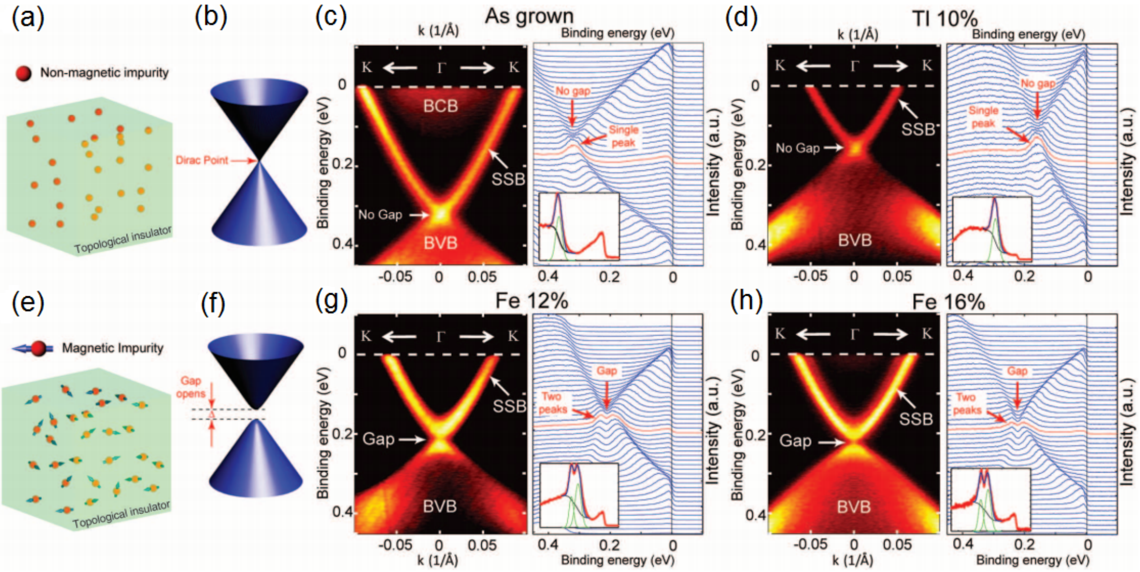

Figure 1.6 Non-magnetic and magnetic doping in a topological insulator. (a) and (b) A non-magnetically doped topological insulator with a Dirac point connecting the upper and lower Dirac cones same as in the undoped case. (c) Band structure along the K-Γ-K direction of undoped Bi_2Se_3. Right subpanel shows the energy distribution curves (EDCs). The red curve indicates the EDC at the Γ point. (d) Band structure for a Tl-doped sample, $(Bi_{0.9}Tl_{0.1})_2Se_3$. (e) and (f) A magnetically doped topological insulator with a gap separating the upper and lower Dirac cones. (g) and (h) Band structure of two Fe-doped samples from two growth batches with melt composition $(Bi_{0.88}Fe_{0.12})_2Se_{3.7}$ and $(Bi_{0.84}Fe_{0.16})_2Se_{3.7}$, respectively. The EDCs indicate a gap formation. (From Ref. [16]).

Due to its spin-momentum-locking effect, the surface Dirac states in the topological insulators are protected by the time-reversal symmetry, i.e., there is no channel for back scattering. Therefore, only time-reversal symmetry breaking sources, such as magnetic field or magnetic impurities can change these fermions from massless to massive states in the topological insulators [21, 22].

Fig. 1.6 shows the electronic structure of Bi_2Se_3 with non-magnetic and magnetic doping. Figs. 1.6(a)–(d) show that with a non-magnetic doping (such as Tl), the system does not violate the time-reversal symmetry. Thus, the dopant Tl only introduces holes into the system, moving the chemical potential down (i.e., the energy location of the Dirac point moves up, closer to the chemical potential). The electronic structure itself (i.e., the shape of the Dirac cone) does not change in this case. However, when a magnetic dopant, such as Fe, is introduced to the system, a gap would appear to separate the upper and lower Dirac cones. As shown in panels (g) and (h), a gap formation can be clearly seen in the energy distribution curves. This demonstrates that the Fermi energy and the energy gap at the surface Dirac point in the topological insulator can be continuously tuned; thus, providing a means to control the surface electric transport, and that indeed could be of great importance for industrial applications [16].

Intuitively, the transition of Dirac electrons from massless to massive states would be symmetric for the upper and lower cones under the influence of the time-reversal symmetry breaking sources. However, in topological insulator candidate (or more precisely, topological semimetal candidate), LaBi, an asymmetric mass acquisition was observed. Interestingly, the surface Dirac cone is buried deeply inside the bulk state and there are no external time-reversal symmetry breaking sources to induce the mass acquisition. We will discuss these observations in more detail in Chapter 3.

1.3 Three-dimensional Dirac Semimetals

As massless Dirac states have been realized in two-dimensional materials (such as graphene) and on the surface of three-dimensional topological insulators (such as Bi_2Se_3), searching for bulk (three-dimensional) Dirac states has attracted great interest. In a two-dimensional massless relativistic electronic system, the minimum model Hamiltonian can be written as $H(\mathbf{k}) = \hbar v(k_x\sigma_x + k_y\sigma_y)$, where v is the relativistic electron velocity, k is the momentum, and σ are Pauli matrices.

$$\sigma_x = \begin{pmatrix} 0 & 1 \\ 1 & 0 \end{pmatrix}, \quad \sigma_y = \begin{pmatrix} 0 & -i \\ i & 0 \end{pmatrix}, \quad \sigma_z = \begin{pmatrix} 1 & 0 \\ 0 & -1 \end{pmatrix} \tag{1.3}$$

The point-like degeneracies between the conduction and valence bands are responsible for many important properties of graphene such as high electron mobility and conductivity. However, the Dirac points are not robust against perturbations proportional to σ_z, which will open a gap in the energy dispersion. Fortunately, the spin-orbit coupling in graphene is not strong enough to significantly double the number of states and open a gap at the Dirac point due to carbon atoms in this system being very light [23].

The analogous Hamiltonian in three dimension can be expressed as $H(\mathbf{k}) = \hbar v_{ij} k_i \sigma_j$. If the determinant of v_{ij} is not equal to zero, $H(\mathbf{k})$ is robust against perturbations and is called a Weyl Hamiltonian because it describes two linearly dispersing bands that are degenerate at a (Weyl) point [24]. In materials with both time-reversal and space inversion symmetries, the Weyl points must come together in pairs, and be degenerate in energy to form symmetry protected three-dimensional Dirac points or annihilate each other. This can be simply illustrated by choosing an arbitrary Weyl node at momentum $\mathbf{k}$. The time-reversal symmetry requires that another Weyl node with the *same* chirality must be present at $-\mathbf{k}$. On the other hand, the inversion symmetry requires that a node of *opposite* chirality must be present at $-\mathbf{k}$. This implies that in the presence of both time-reversal and inversion symmetry, there will exist a pair of opposite-chirality Weyl nodes at the same crystal momentum, i.e., they may annihilate each other instead of forming bulk Dirac points. Therefore, these Dirac points need to be protected by extra crystal symmetry to avoid the annihilation of Weyl fermions with opposite chirality [25]. It has been theoretically predicted that a topological three-dimensional Dirac point can be viewed as a composite of two sets of Weyl fermions where broken time-reversal or space inversion symmetry can lead to a topological insulator phase or a Weyl semimetal phase with surface Fermi-arc states [26]. Thus, bulk Dirac semimetal materials with strong spin-orbit coupling are of great interest since they can serve as parent compounds for other topological quantum materials [24]. Three-dimensional Dirac semimetals with bulk Dirac points protected by crystal symmetry have been proposed to exist in β-cristobalite BiO_2 [24] and A_3Bi ($A =$ Na, K, Rb) [27]. ARPES measurements on $NaBi_3$ and Cd_3As_2 have demonstrated the existence of Dirac dispersions along all three dimensions in the momentum space [26, 28, 29, 30, 31, 32].

Fig. 1.7 shows the crystal structure and ARPES intensity of Cd_3As_2. Figs. 1.7(a) and (b) show the crystal structure of Cd_3As_2, which has a tetragonal unit cell and the arsenic ions are approximately cubic close-packed and Cd ions are tetrahedrally coordinated. Fig. 1.7(d) shows the corresponding Brillouin zone, where the center of the Brillouin zone is the Γ point, the centers of the top and bottom square surfaces are the Z points, and other high-symmetry points are noted. In band structure calculations, Cd_3As_2 shows band inversion but the spin-orbit interaction cannot open up a full energy gap between the inverted bulk conduction and

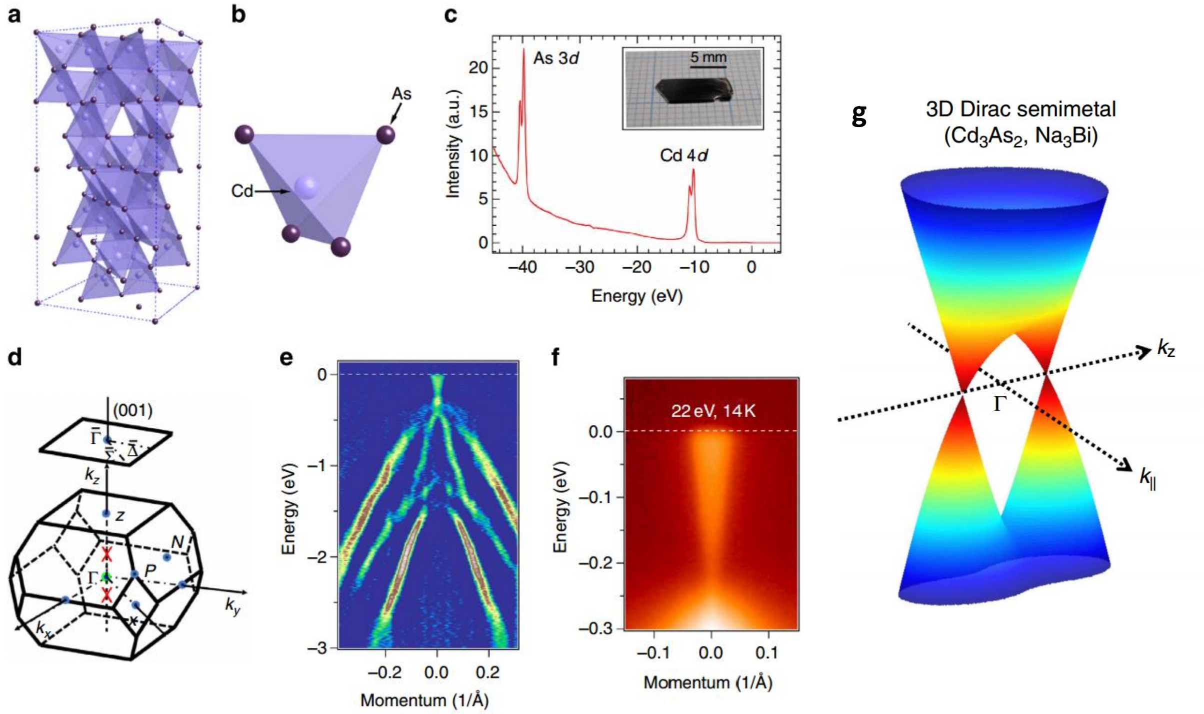

Figure 1.7 Brillouin zone symmetry and three-dimensional Dirac cone in Cd_3As_2 (a) Cd_3As_2 crystallizes in a tetragonal body centered structure. (b) The basic structure unit is a four corner-sharing $CdAs_3$-trigonal pyramid. (c) Core-level spectroscopic measurement where Cd $4d$ and As $3d$ peaks are observed. (d) The bulk Brillouin zone and the projected surface Brillouin zone along the (001) direction. The red crossings mark the locations of the two Dirac band-touchings, which are protected by the crystalline C_4 symmetry along the k_z axis. (e) Second derivative image of ARPES dispersion map of Cd_3As_2. (f) ARPES intensity of Cd_3As_2 near the Fermi level at the surface Brillouin zone center Γ point. (g) Cartoon view of the dispersion of three-dimensional Dirac semimetal. (From Ref. [29]).

valence bands due to its $\mathcal{C}_4$ rotational symmetry along the k_z direction [24, 26]. Two symmetry protected bulk Dirac points have been predicted to exist at two special $\mathbf{k}$ points along the Γ-Z direction in the momentum space [two red crosses in Fig. 1.7(d)]. Figs. 1.7(e) and (f) show the band dispersion of Cd_3As_2 measured at the photon energy of 22 eV and temperature of 14 K, where a Dirac cone structure can be clearly seen within the binding energy of 300 meV. The cartoon view of the dispersion of three-dimensional Dirac semimetal is shown Fig. 1.7(g) with two Dirac points visualized along the k_z direction, which are protected by the $\mathcal{C}_4$ rotation symmetry [29].

As we will discuss in detail in Chapter 2, ARPES measurements carried out at one single photon energy can only probe the k_x and k_y dispersion at specific k_z location. To demonstrate that the band dispersion in Cd_3As_2 is indeed relativistic in all three dimensions and the two Dirac points are located along the k_z direction, detailed photon energy dependence measurements are needed. Although multiple ARPES measurements have carried out the photon energy dependence measurements [29, 30, 31, 32], fine details are still missing in the band dispersion along the k_z direction due to the typical large photon energy steps (a couple of eVs) used in the synchrotron radiation centers. Thus, to better illustrate the three-dimensional Dirac states in Cd_3As_2, we will show detailed ARPES measurements with photon energy steps of ~ 0.15 eV in Chapter 4, .

1.4 Weyl Semimetals

As discussed in the previous section, a three-dimensional Dirac point may exist under crystal symmetry protection, while the Weyl points are more immune to perturbations in general. The Hamiltonian of a Weyl semimetal phase can be expanded as

$$H_{\pm} = \pm\hbar v(k_x\sigma_x + k_y\sigma_y + k_z\sigma_z) \tag{1.4}$$

where ± is the associated chirality for a pair of Weyl nodes, which measures the relative handedness of the three momenta and the Pauli matrices associated in the above equation. The Weyl node can be interpreted as a sink/source, or a monopole of Berry flux. A general property of Weyl fermions realized in band structures is that the Weyl nodes must come in pairs with opposite chirality and the net chirality in the Brillouin zone be zero. As discussed in Section 1.3, when both time-reversal and inversion symmetries are present, the Weyl nodes with opposite chirality will degenerate and annihilate. If there is an extra crystal symmetry protection against the annihilation of the Weyl points, we will have a three-dimensional Dirac semimetal instead. Thus, in order to realize a Weyl semimetal phase, either the time-reversal or inversion symmetry should be broken. The minimal case of just a pair of opposite chirality Weyl nodes requires that the time-reversal symmetry must be broken, which can be achieved

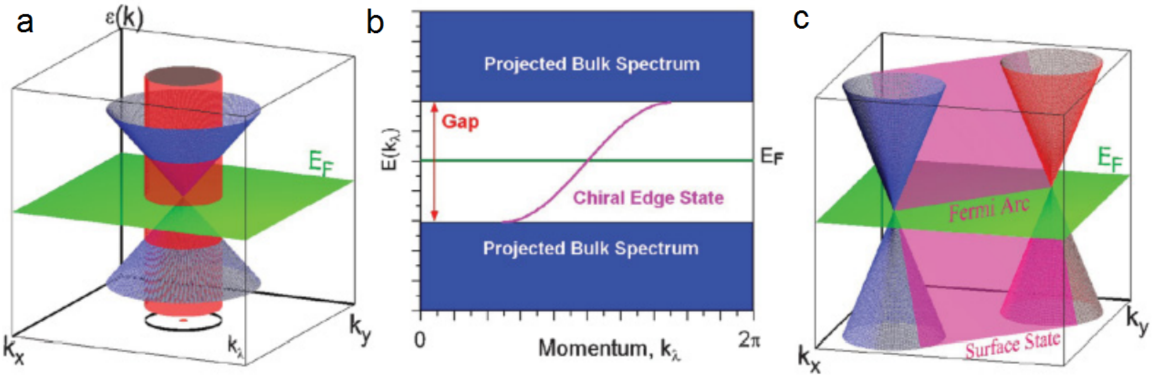

Figure 1.8 Fermi arc surface states in Weyl semimetals. (a) A cylinder encloses the Weyl node with the base defines a one-dimensional circular Brillouin zone . (b) The cylinder unrolled onto a plane gives the spectrum of the two-dimensional subsystem with a boundary. On top of the bulk spectrum, a chiral state appears due to the nonzero Chern number. (c) Meaning of the surface states back in the three-dimensional system. The chiral state appears as a surface connecting the original Dirac cone to a second one, and the intersection between this plane and the Fermi level gives a Fermi arc connecting the Weyl points. (From Ref. [35]).

by magnetic order in the crystal [33] . When inversion symmetry is broken, there are at least two pairs of Weyl nodes present in the system [34].

The band structure of Weyl semimetals has led to two interesting physical properties. One is the chiral magnetic effect [36], which is not the main focus of this thesis. The other is an unusual type of surface state Fermi arc that is present in the system. This is indeed a unique signature of Weyl semimetals [35]. Fig. 1.8 shows the formation of the Fermi arc surface state in an intuitive way. Considering a cylinder enclosing the Weyl node [Fig. 1.8(a)], due to its nonzero Chern number, this cylinder would behave like a two-dimensional quantum Hall system. Thus, there will be a one-dimensional chiral edge state on the energy momentum spectra of this cylinder when unrolled onto a plane [Fig. 1.8(b)]. Apparently, this one-dimensional chiral edge state would cross the Fermi energy E_F at a single point on the Fermi surface. Therefore, by considering all the cylinders enclosing the Weyl node with varying radius from zero to infinity, there will be continuous surface state crossing points at the Fermi level until the cylinder encloses two Weyl nodes with opposite chirality at the same time, leading to zero Chern number of this system. In the end, a surface state Fermi arc starting from one Weyl node and ends at the other Weyl node with opposite chirality will be present as shown in Fig. 1.8(c). If one considers both top and bottom surfaces of a Weyl semimetal sample, a closed Fermi surface would be recovered. Thus, a thin slab of a semimetal may be viewed as a two-dimensional system with a closed Fermi surface. As the thickness increases, two halves of the Fermi surface are spatially separated to opposite sides of the sample [35]. Although multiple ARPES measurements have confirmed the existence of the Fermi arcs on the surface of the Weyl semimetals [37, 38, 39, 40, 41], yet no direct evidence have been found to support the notion of closed surface Fermi arc state formed by both top and bottom surface of the sample.

In search of the Weyl semimetal phase in real materials, iridium pyrochlores, which are strongly correlated magnetic materials, were the first compounds proposed to possess 24 Weyl nodes [35]. A more simplified Weyl semimetal phase with only two Weyl points was proposed to exist in a topological insulator multilayer heterostructure. However, so far no ARPES measurements have provided direct evidence of Fermi arcs on the Fermi surface of these materials. On the other hand, a family of noncentrosymmetric transition-metal monophosphides have been predicted to be Weyl semimetals [42, 43] and direct observation of Fermi arcs have been reported [37, 38, 39, 40, 41].

Fig. 1.9 shows the topology and electronic structure of TaAs. TaAs is a semimetallic material that crystallizes in a body-centered tetragonal lattice system [Fig. 1.9(a)]. The crystal has group space #109, which does not have space inversion symmetry. Thus, the broken space inversion symmetry satisfies the condition for realizing Weyl semimetallic phase in TaAs. Without spin-orbit coupling, first-principles band structure calculations show that there are bulk bands touching each other close to the Fermi level as shown in the blue box in Fig. 1.9(c). These conduction and valence bands interpenetrate each other to form four one-dimensional line nodes (closed loops) located at the k_x and k_y planes. Upon the inclusion of spin-orbit coupling, the line nodes gap out and reduce to six Weyl nodes that are off the $k_x = 0$ and $k_y = 0$ mirror planes. Total of 24 Weyl nodes are shown in Fig. 1.9(f) based on the band structure calculations considering the spin-orbit coupling. Figs. 1.9(g) and (h) shows the Fermi surface from band structure calculations and ARPES measurements, respectively. The Fermi arc that extends out from one Weyl node and ends at the other Weyl node with opposite chirality can

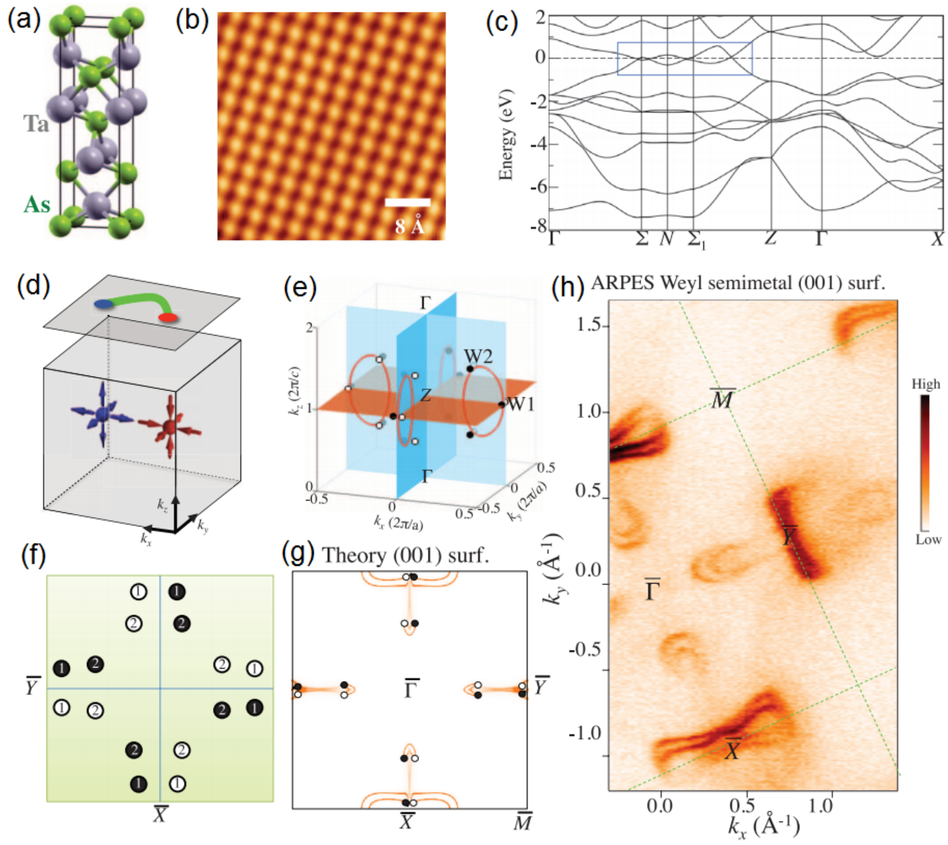

Figure 1.9 Topology and electronic structure of TaAs. (a) Body-centered tetragonal structure of TaAs. The lattice of TaAs does not have space inversion symmetry. (b) STM topographic image of TaAs's (001) surface. (c) First-principles band structure calculations of TaAs without spin-orbit coupling. (d) Illustration of the simplest Weyl semimetal state that has two single Weyl nodes with opposite (± 1) chiral charges in the bulk. (e) In the absence of spin-orbit coupling, there are two line nodes on the k_y mirror plane. In the presence of spin-orbit coupling, each line node reduces into six Weyl nodes. (f) A schematic showing the projected Weyl nodes and their projected chiral charges. (g) Theoretically calculated band structure of the Fermi surface on the (001) surface of TaAs. (h) The ARPES-measured Fermi surface of the (001) cleaving plane of TaAs. (From Ref. [37]).

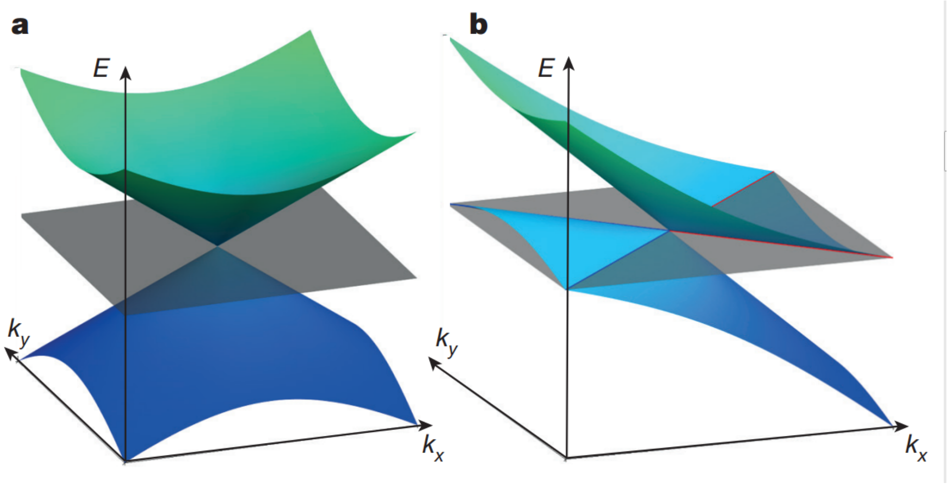

Figure 1.10 Two types of Weyl semimetals. (a) Type-I Weyl point with a point-like Fermi surface. (b) A type-II Weyl point appears as the contact point between electron and hole pockets. The grey plane corresponds to the position of the Fermi level, and the blue (red) lines mark the boundaries of the hole (electron) pockets. (From Ref. [44]).

be clearly seen in the ARPES-intensity and is consistent with the calculations. These results strongly support the existence of Fermi arcs on the surface of TaAs [37].

Interestingly, the family of noncentrosymmetric transition metal monophosphides [42, 43] are now often referred to as the type-I Weyl semimetals. In type-I Weyl semimetals, the conduction and valence bands touch at single points on the Fermi level, forming a point-like Fermi surface at the Weyl point [Fig. 1.10(a)]. Another type of Weyl semimetal, type-II Weyl semimetal has been proposed, where the Weyl points exist at the boundaries between electron and hole pockets as shown in Fig. 1.10(b) [44]. W(Mo)Te_2 family were the first predicted to be type-II Weyl semimetals [44, 45, 46].

Fig. 1.11 shows the data of $MoTe_2$ from ARPES measurements and band structure calculations. The $MoTe_2$ samples cleave between two adjacent Te layers, which breaks the inversion symmetry and gives rise to two chemically similar, but structurally different cleaving planes A and B as shown in Fig. 1.11(d). Fig. 1.11(a) shows the Fermi surface measured by 6.7 eV photons for surface termination A. The hole bands at the center of the Brillouin zone have a “butterfly” shape. The electron pockets shaped like ovals are located on each side of the butterfly. There are also two banana-like hole pockets partially overlapping the oval electron

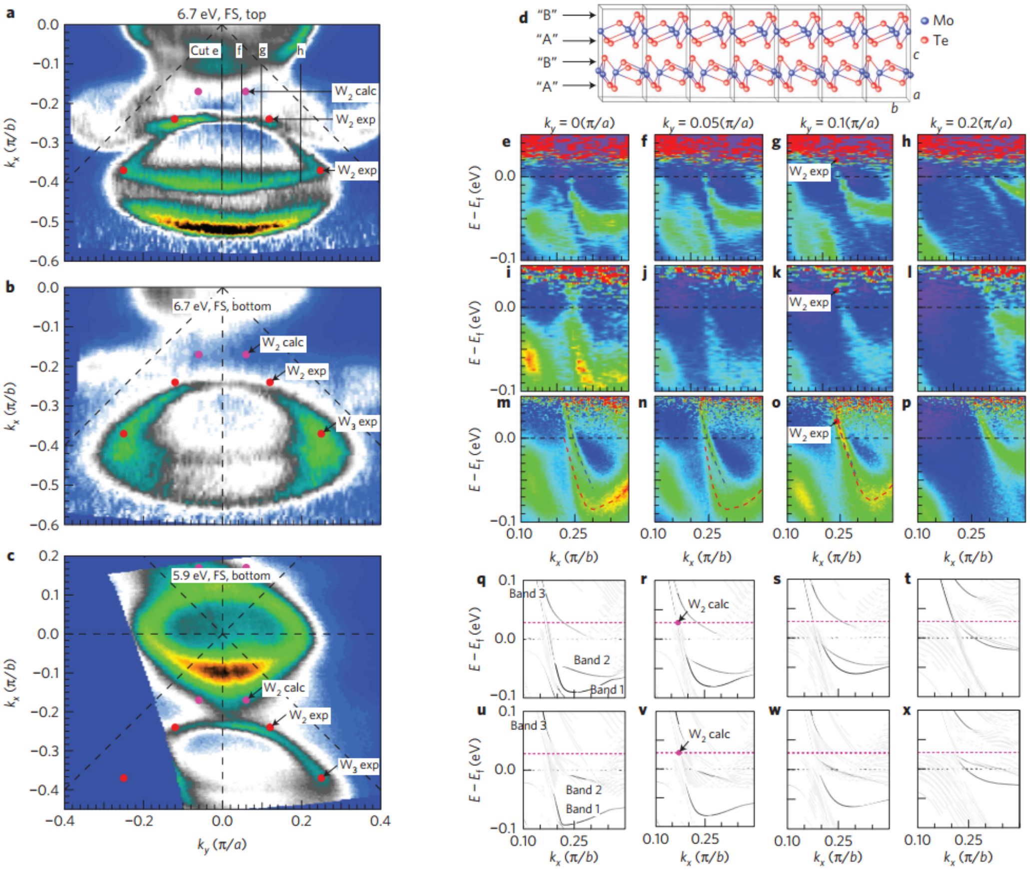

Figure 1.11 Identification of Weyl points and Fermi arcs from experimental data in MoTe$_2$. (a) Constant-energy contour at E_F, measured by 6.7 eV photons for surface termination A. DFT-predicted and measured locations for Weyl points are marked. (b) The same as (a) except for surface termination B. (c) The same as (b) except for using 5.9 eV photons. (d) Schematic drawing of the crystal structure of a single unit cell layer with two different possible surface terminations. (e)–(h), (i)–(l), and (m)–(p) Energy dispersion for (a)–(c) along the black lines, respectively. (q)–(t) and (u)–(x) Calculated band dispersion for surface termination A and B, respectively. (From Ref. [47]).

pockets. Since the A and B terminations are different, the electronic structure of each termination is expected to be slightly different [as demonstrated in Figs. 1.11(a) and (b)] due to the different length of the Mo–Te bonds. The data along the k_x direction are shown in Figs. 1.11(e)–(p) along with results of calculations [Figs. 1.11(q)–(x)] for the two surface terminations. The data in Figs. 1.11(m)–(p) best illustrate the formation of the W$_2$ points, which shows that the hole band (red dashed line) and electron band (blue dashed line) move closer as we move away from the symmetry line and merge at a point located $\sim$ 20 meV above E_F marked by a red dot in Fig. 1.11(o). These results demonstrate the formation of type-II Weyl points in $MoTe_2$.

In addition to the laser ARPES measurements carried out at high temperature to detect Weyl points located above E_F in $MoTe_2$ [47], pump-probe ARPES has also been utilized to to populate unoccupied states by exciting low lying electrons in $Mo_xW_{1-x}Te_2$ [48]. However, strong evidence for the existence of Fermi arcs in another type-II Weyl semimetal WTe_2 is still lacking. In Chapter 5, we will discussed the detailed electron properties of WTe_2, including the temperature-induced Lifshitz transition, the Fermi arcs on the surface, and the strong three-dimensionality of the bulk electronic structure in this material.

1.5 Dirac Node Line Semimetals

As we have seen in previous sections, the conduction and valence bands can touch at distinct points, leading to the symmetry protected Dirac or Weyl semimetallic states in the material. Another type of special band touching is the case of Dirac node lines, where the conduction and valence bands are touching along a closed curve. The Dirac node lines can either take the form of extended lines running across the Brillouin zone with ends meet at the zone boundary [49], or wind into closed loops inside the Brillouin zone [50], or even form a node chain with several loops connected to each other [51]. Interestingly, when the symmetry protection is broken in a topological node line semimetal, the node line can be fully gapped leading to a trivial electronic structure, or gapped into several node points leading to Dirac or Weyl semimetallic states. As we have discussed in Section 1.4, TaAs was a node line semimetal in first principles calculations without considering spin-orbit coupling. When the spin-orbit coupling in TaAs is turned on, the node lines break into three pairs of Weyl nodes. Thus, topological node line semimetals could potentially be the parent compound of other topological semimetallic states, which can be precisely tuned by symmetry breaking [52]. Searching for topological node line semimetals have attracted great interest.

Multiple groups have proposed the Dirac node line structure to exist in graphene networks [54], rare earth monopnictides [55], and *et al.* ARPES measurements on $PbTaSe_2$ [53] and

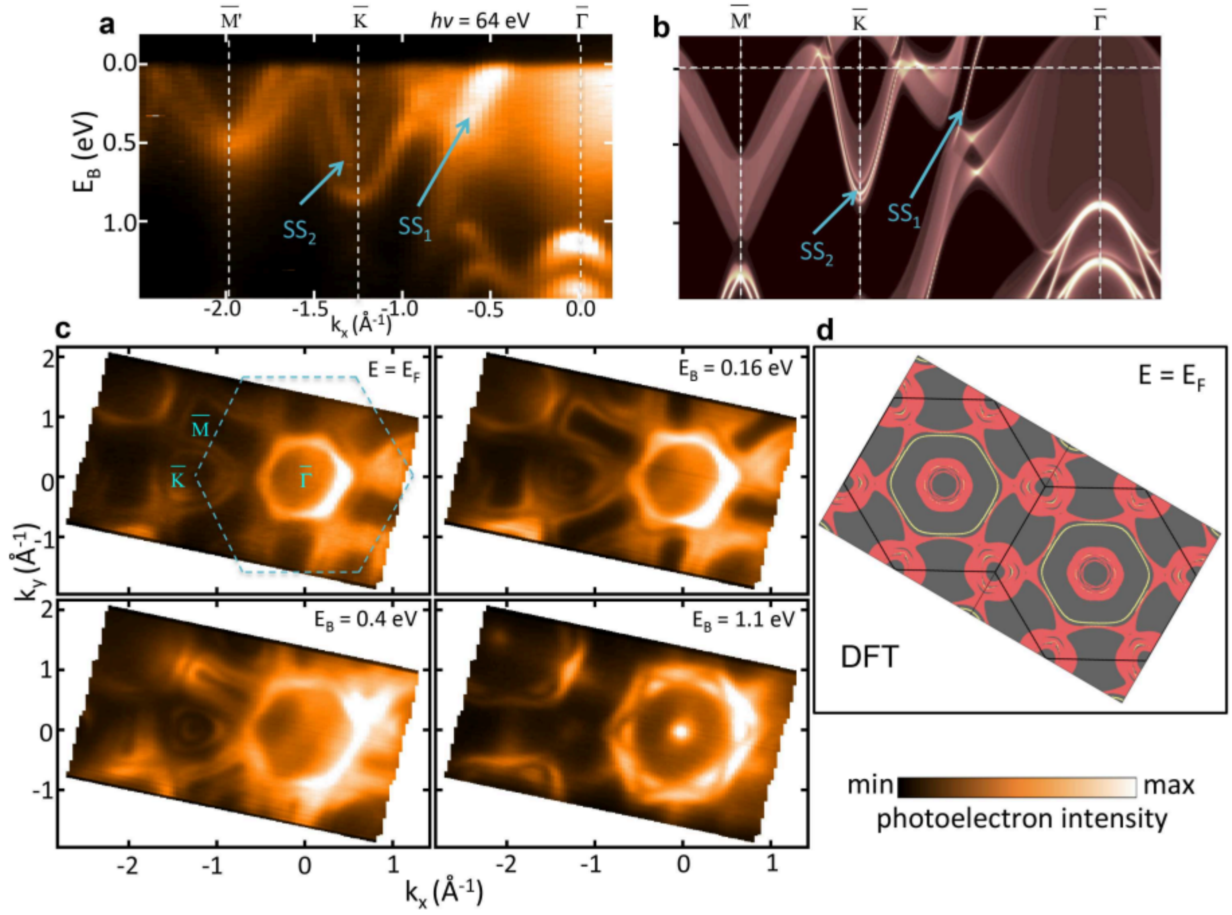

Figure 1.12 ARPES mapping and band calculation of $PbTaSe_2$. (a) ARPES spectra taken along M–K–Γ at photon energy of 64 eV. (b) DFT projected bulk bands and surface bands (bright white lines) of (001) surface with Pb-termination. (c) ARPES constant-energy contours taken at photon energy of 64 eV. (d) DFT Fermi surface contour of $PbTaSe_2$ (001) surface). The yellow lines indicate the surface states on Pb-terminated (001) surface. (From Ref. [53]).

ZrSiS [56] have shown evidence of the existence of Dirac-like features and "drumhead" surface states, which point to the potential node line semimetallic states in these materials. Fig. 1.12 shows the ARPES mapping and band calculation for $PbTaSe_2$. Band structures from ARPES measurements and corresponding numerical calculations of $PbTaSe_2$ are shown in Figs. 1.12(a) and (b), respectively. The projected bulk bands and surface bands for the Pb-termination (001) surface were shown with the surface states highlighted by the white lines and marked by the blue arrows. The (001) Fermi surface of $PbTaSe_2$ from ARPES measurements with 64 eV photons and theoretical simulations are shown in Figs. 1.12(c) and (d). At the Fermi level, the Fermi surface consists of three parts: a hexagon-shaped pocket centered at Γ with smeared intensity inside, a dog-bone-shaped contour centered at the M point, and several circles surrounding the K point. The "drumhead" shape surface states at the K points are noted as evidence supporting the existence of the topological node line semimetallic states in this material [53]. However, further research is still needed to understand fully the significance and relation of the "drumhead" surface states to Dirac node lines.

As we have discussed at the beginning of this section, the Dirac node lines in the materials are typically closed loops or extended across the entire Brillouin zone. However, we have observed a completely different Dirac node line structure–Dirac node arc–in $PtSn_4$, a compound showing extremely large magnetoresistance at low temperatures and high magnetic fields. Unlike the closed loop Dirac node line, the Dirac node arc is formed by Dirac dispersion extended along one dimension in the momentum space and terminated by energy gaps at both ends. Detailed electronic structure of $PtSn_4$ will be presented in Chapter 6.

CHAPTER 2. ANGLE-RESOLVED PHOTOEMISSION SPECTROSCOPY (ARPES)

In this chapter, we will cover the basic principles of angle-resolved photoemission spectroscopy (ARPES), the components of the ARPES system, and techniques for preparation of sample surface. In Section 2.1, we will present the basic principles of ARPES measurements and explain how the conservation of energy and momentum is used to infer the energy and momentum of the electrons. There are two theoretical approaches to describe the photoemission process: comprehensive one step model and much simpler three step model. We will mainly focus on the three-step model in this thesis, because it is easy to understand and sufficiently captures the essence of the photoemission process. We will introduce single particle spectral function that is used to describe the interaction of electrons in solids. Finally, matrix elements play an important role in determining the intensity of the ARPES spectral, a brief discussion will be given in this section.

After the discussion of the basic principles, we will then present the description of the components in the ARPES system in Section 2.2. Photon source is one of the most crucial components in the APRES system. With the basic Helium-discharge lamp, it is easy to setup an in-house system. However, only the He Iα spectral line with photon energy of 21.2 eV has sufficient intensity for acquiring high quality data. Synchrotron radiation photon sources are also commonly used, with its great advantage of wide range of tunable photon energies from tens of to hundreds of eV. With the emergence of advanced laser photon sources, ultrahigh momentum and energy resolutions can be now achieved. The advantages and disadvantages of these photon sources will be discussed in this section along with examples. After the electrons have been excited and escaped from the sample surface, angle (momentum) resolved electron analyser will be used to determine the energy and momentum information of the photoelectrons.

In order to obtain the information about the initial state of the electrons in a photoemission experiment, their path from the sample to the detector has to be maintained at ultrahigh vacuum. Even slightly elevated pressure will cause condensation at sample surface and scattering of the photoelectrons. The importance of keeping an ultrahigh vacuum in the ARPES system will be discussed briefly. In order to control the sample temperatures precisely, cold head and cold finger are also important, especially for studying superconductivity, magnetic phase transitions, and structural phase transitions. Thus, a brief introduction to cold head will also be included in this section.

In Section 2.3, we will present a couple of methods to prepare the sample before we can measure the electronic properties of the crystal. Cleaving the sample in ultrahigh vacuum is the most widely used method to obtain a clean and flat surface, which works pretty well for layer crystals. For samples that cannot be cleaved properly, a sequence of polishing, sputtering, and annealing techniques can be used. For measuring thin film samples, Molecular Beam Epitaxy (MBE) technique has become very popular. However, we do not have the capability of doing MBE growth in our system yet. Thus, we will mainly focus on the first two techniques.

2.1 Principles of ARPES

2.1.1 Photoemission Process

The observation of photoelectric effect by Heinrich Hertz [57] in 1887 has inspired great interest in investigating the properties of light and its interaction with matter. In 1902, Lenard observed that the energy of the emitted electrons increased with higher incident frequency of the light [58]. Three years later, Albert Einstein introduced the idea of discrete quanta to describe the photoelectric effect [59] and built the foundation of the dual nature of light, as both a electromagnetic wave and a single particle photon. The discovery of the quantization of light led to the quantum revolution in physics and earned Einstein the Nobel Prize in Physics in 1921. Since then, photoelectric effect has been widely used in the photoemission spectroscopy to study the electronic properties of materials.

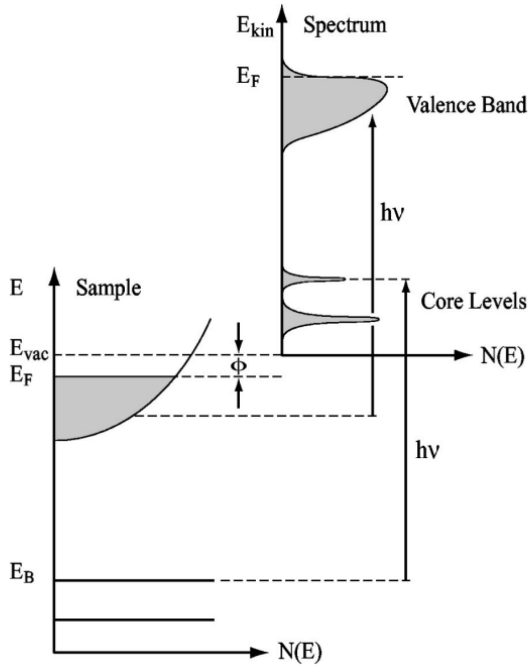

Figure 2.1 Energetics of the photoemission process. The electron energy distribution produced by incoming photons and measured as a function of the kinetic energy E_{kin} of the photoelectrons (right) is more conveniently expressed in terms of the binding energy E_B (left) when one refers to the density of states inside the solid ($E_B = 0$ at E_F). (From Ref. [60]).

Fig. 2.1 shows a schematic of the photoemission process. An electron inside the material absorbs a photon with the energy $h\nu$, overcomes the binding energy E_B and the work function ϕ, then escapes into the vacuum with energy E_{kin}. This process can be expressed by the following equation

$$h\nu = E_B + \phi + E_{kin} \tag{2.1}$$

where the work function (ϕ) is typically around 4–5 eV for metals, and represents the potential barrier that prevents the electrons from escaping from a solid [60]. To avoid measuring the work function for each sample, the samples measured in the ARPES system are in electrical contact with the analyzer and a reference gold sample that is used to determine the Fermi energy of the system.

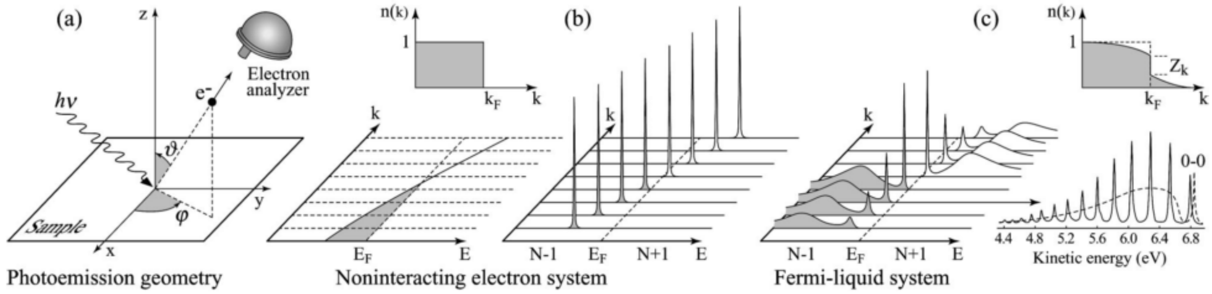

Figure 2.2 Schematic of the angle-resolved photoemission spectroscopy. (a) Schematic of an ARPES experiment. The emission direction of the photoelectron is specified by the polar (θ) and azimuthal (ψ) angles. (b) Momentum-resolved one-electron removal and addition spectra for a noninteracting electron system with a single energy band dispersing across E_F. (c) The same spectra for an interacting Fermi liquid system. (From Ref. [60]).

By taking advantage of the energy conservation law as shown above, we could get the binding energy of the electrons by doing simple algebra to solve Eq. 2.1.

$$E_B = h\nu - \phi - E_{kin} \tag{2.2}$$

One of the most commonly used techniques based on this process is the X-ray photoelectron spectroscopy (XPS), which was developed by Kai Siegbahn and *et al* in 1957 [61]. XPS is also known as Electron Spectroscopy for Chemical Analysis (ESCA), which emphasizes the chemical information that the technique provides. By probing the energy core levels of the elements in the material, elemental composition can be detected [62].

In order to determine the momentum of the electrons in the materials, angle-resolved photoemission spectroscopy was developed. Fig. 2.2(a) shows the schematic of an ARPES experiment. A beam of photons with known photon energy $h\nu$ is incident on the sample, which has an atomically flat surface and has to be a single crystal for momentum-resolved measurements. The electrons inside the sample will be excited and escape into vacuum with various emission directions, which are specified by θ and ψ. After travelling through ultrahigh vacuum, the electrons are then collected by the electron analyzer, where energy and momentum of the electrons are acquired on a charge coupled device (CCD) camera.

By measuring the kinetic energy E_{kin} and the departure angle of the electrons, the electron momentum can be determined based on the following formula

$$p_{\|} = \hbar k_{\|} = \sqrt{2mE_{kin}} \cdot sin\theta \tag{2.3}$$

$$p_{\perp} = \hbar k_{\perp} = \sqrt{2m(E_{kin} \cdot cos^2\theta + V_0)} \tag{2.4}$$

where $p_{\|}$ ($p_{\perp}$) is the momentum component parallel (perpendicular) to the surface of the sample. Parallel component of the electron momentum is conserved in the photoemission process, because we can neglect the photon momentum at low photon energies used in the ARPES measurements (less than a few hundred eV) and the sample surface is atomically flat. However, the momentum perpendicular to the sample surface is not conserved, therefore we need to consider the inner potential V_0 in the formula, which is hard to determine precisely. Several methods can be used to determine the value of V_0, such as matching the theoretical and experimental band mapping for the occupied electronic state, using the theoretical zero of the muffin tin potential used in band structure calculations, or inferring from the experimentally observed periodicity of the out of plane direction dispersion $E(k_{\perp})$ [63]. The last method can be easily achieved in the ARPES experiment by varying the incident photon energies. Therefore the $k_{\perp}$ (and its periodicity) of the emitting electrons can be determined after utilizing Eqs. 2.2 and 2.4.

As for the momentum parallel to the surface of the sample $p_{\|}$, we can determine the x and y component of the momentum (assuming we are looking at $x - y$ plane of the sample) by measuring the electron outgoing angles θ and ψ.

$$p_x = p_{\|} \cdot cos\psi = \sqrt{2mE_{kin}} \cdot sin\theta \cdot cos\psi \tag{2.5}$$

$$p_y = p_{\|} \cdot sin\psi = \sqrt{2mE_{kin}} \cdot sin\theta \cdot sin\psi \tag{2.6}$$

As shown in Fig. 2.2(b), by measuring the angles of the outgoing electrons, a single band dispersion under the assumption of noninteracting electron system can be mapped out dispersing through the Fermi energy. Both the direct and inverse photoemission spectra are shown, and the former one is usually observed in a conventional ARPES system. When considering the interacting Fermi liquid system, the single electron spectral would have a finite band width [as shown in Fig. 2.2(c)], which contains information about the lifetime (interaction and scattering) of the electrons in the material [60]. To describe the photoemission process, three-step model is often discussed.

2.1.2 Three-step Model

The photoemission process discussed above can be described by two models: three-step and one-step model as shown in Fig. 2.3. In the one-step model, the photon absorption, electron removal, and electron detection are treated as a single coherent process. Thus, the bulk, surface, and vacuum have to be included in the Hamiltonian of interaction, which makes the one-step model really complicated. Due to the complexity of the one-step model, three-step model is usually used to describe the photoemission process. Although this model uses several assumptions and simplifications, it has been proved to be rather successful. Within this approach, three independent and sequential steps are included in the photoemission process: (1) The electron is excited by the incident photon, (2) The excited electron travels from the bulk to the surface, (3) The excited electron on the sample surface escapes into vacuum. The total photoemission intensity is just the product of these three independent terms representing the probability of each process. The first step represents the probability of the optical transition, which provides information about the intrinsic electronic structure of the material and gives rise to the matrix element effect that we will discuss in this section. The second step is proportional to the probability that the excited electron travels from the bulk to the surface without any scattering, thus the energy and momentum of the excited electron are considered to be conserved in order to reflect the intrinsic electronic structure in the sample. This probability is tightly connected to the effective mean free path of the excited electrons, which will be discussed along with the photon sources used in the ARPES experiment (Section 2.2.1). The third step is the transmission probability of the excited electrons through the surface, which depends on the energy of the electrons and the material's work function [60].

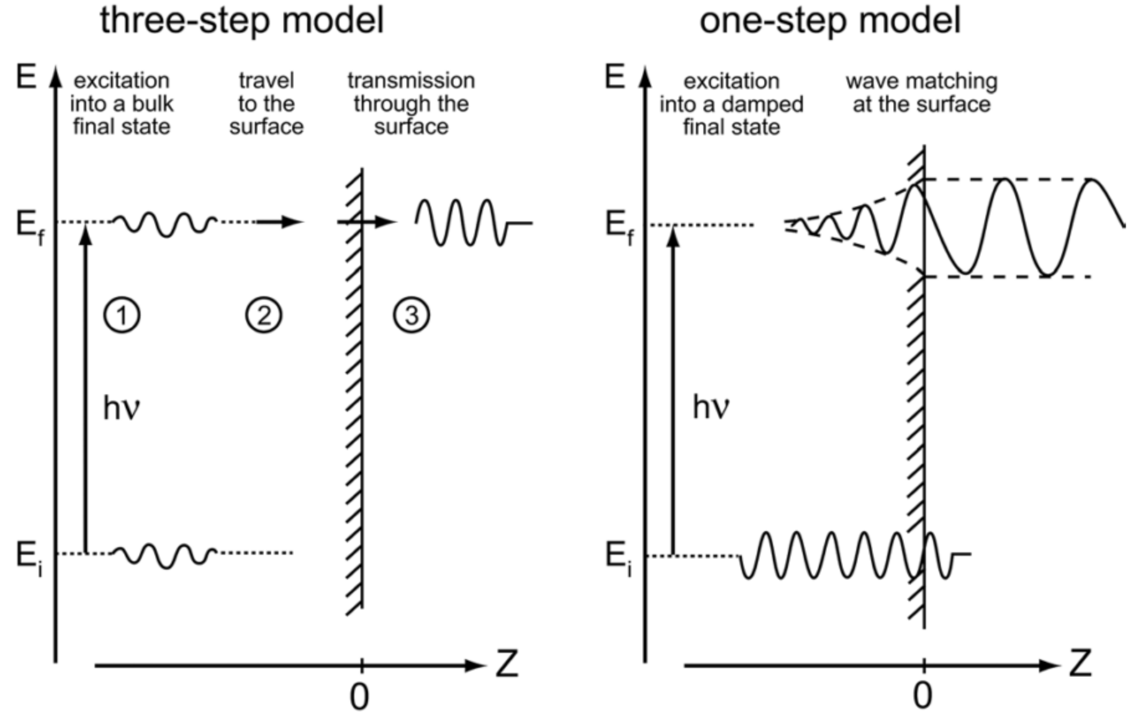

Figure 2.3 Pictorial representation of three-step and one-step model descriptions of the photoemission process (From Ref. [63]).

The transition probability w_{fi} in the first step of the photoemission process can be approximated by Fermi's golden rule:

$$w_{fi} = \frac{2\pi}{\hbar} |\langle \Psi_f^N | H_{int} | \Psi_i^N \rangle|^2 \delta(E_f^N - E_i^N - h\nu) \tag{2.7}$$

where Ψ_i^N stands for the N-electron initial state, Ψ_f^N is one of the possible final states, $E_i^N = E_i^{N-1} - E_B^k$ and $E_f^N = E_f^{N-1} + E_{kin}$ are the initial and final state energies of the N-particle system (E_B^k is the binding energy of the photoelectron with kinetic energy E_{kin} and momentum k). The Hamiltonian for interaction with the photon can be written as

$$H_{int} = \frac{e}{2mc}(\mathbf{A} \cdot p + p \cdot \mathbf{A}) = \frac{e}{mc}\mathbf{A} \cdot p \tag{2.8}$$

where p is the electronic momentum operator and $\mathbf{A}$ is the electromagnetic vector potential. In this approximation, gauge $\Phi = 0$ was chosen for the scalar potential, and the quadratic term in

A was not considered since it is typically negligible when compared to the linear terms in the linear optical regime. This interaction Hamiltonian plays an important role when considering matrix element effect or circular dichroism effect in the ARPES measurements [63]. This will be further demonstrated in the section of photon sources.

In order to calculate the photoemission intensity in terms of the transition probability w_{fi} in the first step of the photoemission process, we need to introduce the *sudden approximation* assumption. Under this assumption, the photoemission process is assumed to be *sudden*, i.e., an electron is instantaneously removed and the effective potential of the system changes discontinuously at that instant. Thus, we can factorize the initial and final state wave functions in Eq. 2.7 into photoelectron and (N-1)-electron terms,

$$\Psi_i^N = \mathcal{A}\phi_i^k \Psi_i^{N-1} \tag{2.9}$$

$$\Psi_f^N = \mathcal{A}\phi_f^k \Psi_f^{N-1} \tag{2.10}$$

where $\mathcal{A}$ is an antisymmetric operator that ensures that the N-electron wave function satisfies the Pauli principle, ϕ_i^k (ϕ_f^k) is the initial (final) one-electron orbital with momentum k, and Ψ_i^{N-1} (Ψ_f^{N-1}) is the initial (final) state wave function of the $(N-1)$-electron system. Thus, the matrix element in Eq. 2.7 can be expressed as

$$\langle \Psi_f^N | H_{int} | \Psi_i^{N-1} \rangle = \langle \phi_f^k | H_{int} | \phi_i^k \rangle \langle \Psi_m^{N-1} | \Psi_i^{N-1} \rangle \tag{2.11}$$

where $\langle \phi_f^k | H_{int} | \phi_i^k \rangle \equiv M_{f,i}^k$ is the one-electron dipole matrix element, $\langle \Psi_m^{N-1} | \Psi_i^{N-1} \rangle$ is the $(N-1)$-electron overlap integral, Ψ_m^{N-1} is the eigenfunction with energy E_m^{N-1} of the $(N-1)$-electron system after one-electron removal. The total transition probability is given by the sum over all possible excited states m.

$$I(k, E_{kin}) = \sum_{f,i} w_{f,i} \propto \sum_{f,i} |M_{f,i}^k|^2 \sum_m |c_{m,i}|^2 \delta(E_{kin} + E_m^{N-1} - E_i^N - h\nu) \tag{2.12}$$

where $|c_{m,i}|^2 = |\langle \Psi_m^{N-1} | \Psi_i^{N-1} \rangle|$ is the probability of the case that the removal of an electron from state i will leave the $(N-1)$-electron system in the excited state m. Since the eigenfunctions of the $(N-1)$-electron system are orthogonal to each other, the probability $|c_{m,i}|^2$ will be zero unless $\Psi_m^{N-1} = \Psi_i^{N-1}$, leading to unity probability. In this case, if $M_{f,i}^k \neq 0$, the ARPES spectra will be given by a delta function at the Hartree-Fock orbital energy E_B^k as shown in Fig. 2.2(b). However, this is assuming that we are in the noninteracting particle regime. When considering strongly correlated systems, many of the $|c_{m,i}|^2$ will be different from zero because the removal of the photoelectron results in a significant change of the system effective potential. Thus, the overlap integral between Ψ_i^{N-1} and many final eigenstates Ψ_m^{N-1} will be non-zero. As a result, the final ARPES spectra are not delta functions but will show a main line and several satellites corresponding to the non-zero excited states m created in the photoemission process as shown in Fig. 2.2 [60].

2.1.3 One-particle Spectral Function

When considering the correlated systems, the ARPES spectra are no longer δ-functions and several other states will have finite probability $|c_{m,i}|^2$ in Eq. 2.12. Green's function formalism is the most powerful and commonly used approach to solve this problem. In this approach, the one-electron addition and removal Green's function $G^+(k,\omega)$ and $G^-(k,\omega)$ are introduced at $T = 0$

$$G^{\pm}(k,\omega) = \sum_m \frac{|\langle \Psi_m^{N\pm 1}|c_k^{\pm}|\Psi_i^N\rangle|^2}{\omega - E_m^{N\pm 1} + E_i^N \pm i\eta} \tag{2.13}$$

where the operator $c_k^+ = c_{k\sigma}^+$ $(c_k^- = c_{k\sigma})$ creates (annihilates) an electron with energy ω, momentum k, and spin σ in the N-particle initial state Ψ_i^N. The summation adds up all possible $(N\pm1)$-particle eigenstates $\Psi_m^{N\pm 1}$ with eigenvalues $E_m^{N\pm 1}$, and η is a positive infinitesimal. Thus, we will have the *one-particle spectral function*

$$A(k,\omega) = A^+(k,\omega) + A^-(k,\omega) = -\frac{1}{\pi}\mathrm{Im}G(k,\omega) \tag{2.14}$$

$$A^{\pm}(k,\omega) = \sum_m |\langle \Psi_m^{N\pm 1}|c_k^{\pm}|\Psi_i^N\rangle|^2 \delta(\omega - E_m^{N\pm 1} + E_i^N) \tag{2.15}$$

where $G(k,\omega) = G^{+}(k,\omega) + [G^{-}(k,\omega)]^{*}$ is the *retarded Green's funciton.* $A^{+}(k,\omega)$ and $A^{-}(k,\omega)$ are the one-electron removal and addition spectra, which can be obtained with direct and inverse photoemission, respectively.

By comparing $A^{-}(k,\omega)$ and Eq. 2.12 (note that c_k is the annihilation operator for one electron with momentum k, thus $\Psi_i^{N-1} = c_k \Psi_i^N$), and taking into account the finite-temperature effect, the intensity measured in an ARPES experiment on a two-dimensional single-band system can be written as

$$I(k,\omega) = I_0(k,\nu,A) f(\omega) A(k,w) \tag{2.16}$$

where k is the electron momentum, ω is the electron energy with respect to the Fermi level, and $I_0(k,\nu,A)$ is proportional to the squared one-electron matrix element $|M_{f,i}^{k}|^2$. Therefore the ARPES intensity depends on the electron momentum, as well as the energy and polarization of the incoming photon (more details will be discussed in Section 2.1.4). Fermi function $f(\omega) = (e^{\hbar\omega/k_B T} + 1)^{-1}$ accounts for the fact that direct photoemission only probes the occupied electronic states.

The energy renormalization and lifetime of the electron in the many-body system can be inferred from the real and imaginary parts of the self-energy term $[\Sigma(k,\omega) = \Sigma^{'}(k,\omega) + i\Sigma^{''}(k,\omega)]$, respectively. Using the self-energy terms, the Green's and spectral functions can be expressed as the following

$$G(k,\omega) = \frac{1}{\omega - \epsilon_k - \Sigma(k,\omega)} \tag{2.17}$$

$$A(k,\omega) = -\frac{1}{\pi} \frac{\Sigma^{''}(k,\omega)}{[\omega - \epsilon_k - \Sigma^{'}(k,\omega)]^2 + [\Sigma^{''}(k,\omega)]^2} \tag{2.18}$$

The spectral function $A(k,\omega)$ has the form of a Lorentzian function if Σ is a linear function of ω. Thus, fitting the ARPES spectral with a Lorentzian function is often used to extract information about scattering rates and energy renormalization. In general, it is extremely difficult to extract the exact values of $\Sigma(k,\omega)$ from the ARPES spectra, since high quality measurements are typically obtained with the direct photoemission process [63].

2.1.4 Matrix Elements

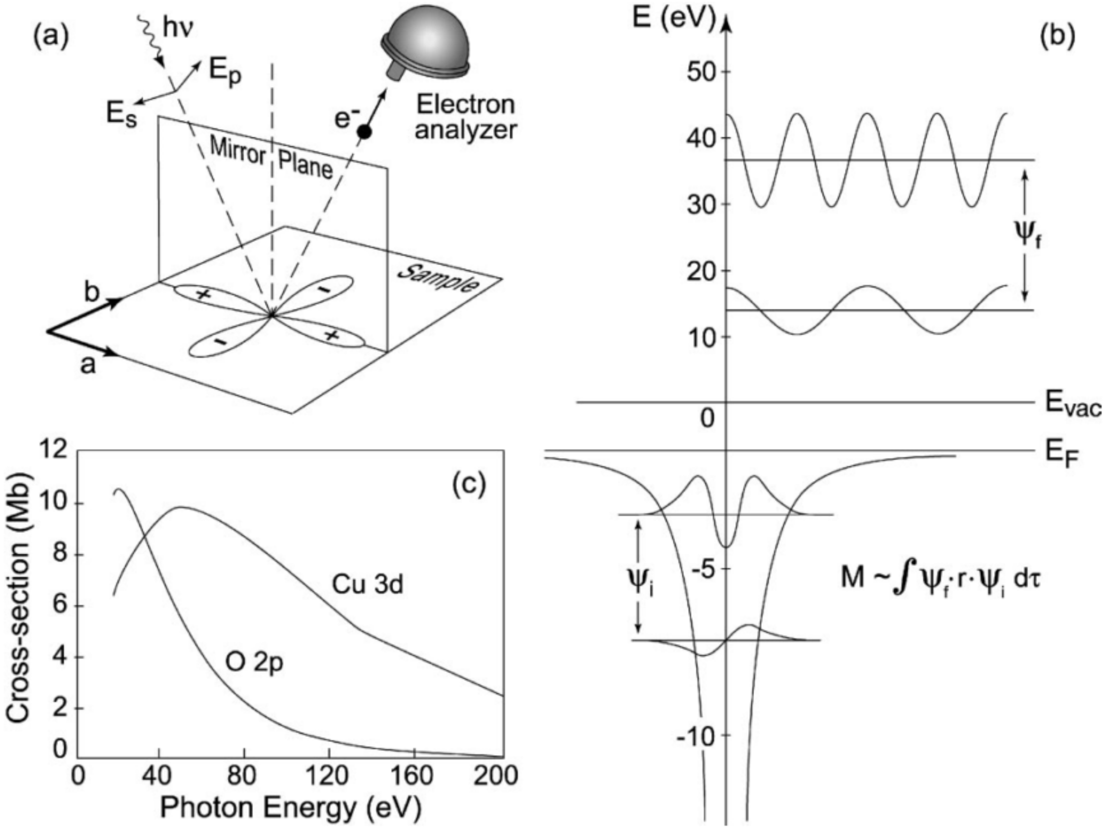

Figure 2.4 Schematic representation of the polarization and photon energy effects in the photoemission process. (a) Mirror plane emission from a $d_{x^2-y^2}$ orbital. (b) Sketch of the optical transition between atomic orbitals with different angular momenta (the wave function of the harmonic oscillator are used here for simplicity) and free-electron wave functions with different kinetic energies. (c) Calculated photoionization cross sections for Cu 3*d* and O 2*p* atomic levels. (From Ref. [63]).

As we have pointed out in Section 2.1.3, the probability of the optical transition in the first step of the photoemission process depends on the matrix element term $|M^k_{f,i}|^2$. Therefore, the initial and final states of the electron, as well as the energy and polarization of the incoming photons will have a significant effect on the ARPES intensity. Not only does the matrix elements depend on the properties of the electron and photons (such as the energy and momentum), but also the experimental geometry, which may even result in complete suppression of the ARPES intensity. By substituting the interaction Hamiltonian from Eq. 2.8, the matrix element term

$|M_{f,i}^k|^2$ can be written as $|M_{f,i}^k|^2 \propto |\langle\phi_f^k|\mathbf{A}\cdot p|\phi_i^k\rangle|^2$, where the vector potential $\mathbf{A}$ will specify the polarization direction of the incoming photons. Fig. 2.4 shows an example of considering the experimental geometry in the ARPES measurements. In Fig. 2.4(a), the electron analyzer is pointed in the mirror plane of the photoemission from a $d_{x^2-y^2}$ orbital. In order to have nonvanishing photoemission intensity, the whole function in the overlap integral must be even under reflection with respect to the mirror plane. Furthermore, the final state wave function ϕ_f^k must have even-parity in the mirror plane; otherwise, there would be zero intensity everywhere including the detector. Therefore, the term $(\mathbf{A}\cdot p)|\phi_i^k\rangle$ must be even. Considering both even and odd symmetry of the initial state, the polarization conditions of the incoming photons can be summarized as the following

$$\langle\phi_f^k|\mathbf{A}\cdot p|\phi_i^k\rangle = \begin{cases} \phi_i^k \quad \mathit{even} \qquad \langle +|+|+\rangle \Rightarrow \mathbf{A} \quad \mathit{even} \\ \phi_i^k \quad \mathit{odd} \qquad \langle +|-|-\rangle \Rightarrow \mathbf{A} \quad \mathit{odd} \end{cases} \tag{2.19}$$

In the example shown in Fig. 2.4(a), the initial state $|\phi_i^k\rangle$ is even. Thus, the potential vector $\mathbf{A}$ must be even or pointing in the mirror plane in order to observe finite ARPES intensity from this orbital. The transition probability also depends on the incoming photon energy, which determines the energy and momentum of the outgoing electron as demonstrated in Figs. 2.4(b) and (c). By considering a plane wave $e^{i\mathbf{kr}}$ for the photoelectron at the detector, the matrix element can be written as $|M_{f,i}^k|^2 \propto |(\mathbf{A}\cdot p)\langle\phi_i^k|e^{i\mathbf{kr}}\rangle|^2$. The overlap integral strongly depends on the details of the initial state wave function, and on the wavelength of the outgoing plane wave [as shown in Fig. 2.4(b)]. In Fig. 2.4(c), we can clearly see that for Cu 3d and O 2p the photoionization cross section strongly depends on the photon energy used in the measurements.

2.2 Components of an ARPES System

With the knowledge of the basic principles of an ARPES measurement, we now proceed to look into the details of each component in the ARPES system. As we have discussed in Section 2.1.1, the photoemission process of the ARPES experiment can be described by the three-step model with the first step as the excitation of the photoelectrons by the incident light. Indeed, photon sources play an essential role in the ARPES system. Various photon sources, such as He-discharge lamps, synchrotron radiations, and laser photon sources have been used throughout the study and will be discussed separately with detailed examples from the unpublished results. After escaping the sample surface, the photoelectrons will be collected by a hemispherical electron analyzer for energy and momentum analysis. Basic concept and principle of operation of an electron analyzer will be discussed to explain how the energy and momentum information can be obtained at the same time. Ultrahigh vacuum is very important in preserving the information of the photoelectrons, since they need to travel a fairly long distance (∼ 2 m) from the sample surface to the electron analyzer. Due to the limited probing depth of the ARPES system, preserving the freshness of the cleaved sample surface also requires the ultrahigh vacuum. Finally we will discuss basic knowledge of a cold head for controlling the sample temperature from room temperature (300 K) to low temperature (∼ 15 K), which is essential for studying magnetic phase transitions as shown in Section 2.2.4 and structural phase transitions shown in Fig. 2.21.

2.2.1 Photon Source

ARPES measurements are typically performed with photon energies less than a few hundred eV. However, recently keV photon sources gained some popularity due to enhancement of the escape depth of the photoelectrons, which enables measurements of bulk electronic structure. One important aspect of choosing the low photon energy is the ability to achieve high momentum resolution. By taking the derivatives of Eq. 2.3, the resolution of the parallel component of the momentum can be expressed as the following

$$\Delta p_{\parallel} = \hbar \Delta k_{\parallel} = \sqrt{2mE_{kin}} \cdot cos\theta \cdot \Delta\theta \tag{2.20}$$

where $\Delta\theta$ corresponds to the finite acceptance angle of the electron analyzer. Therefore, lower photo energy would result in lower E_{kin} and typically yield higher momentum resolution assuming that the same electron analyzer is used in the ARPES experiment. Fig. 2.5 shows the Fermi surface and band dispersion measured at two different photon energies. Panels (a) and (b) show the ARPES intensity measured at the photon energy of 21.2 eV in the He-lamp

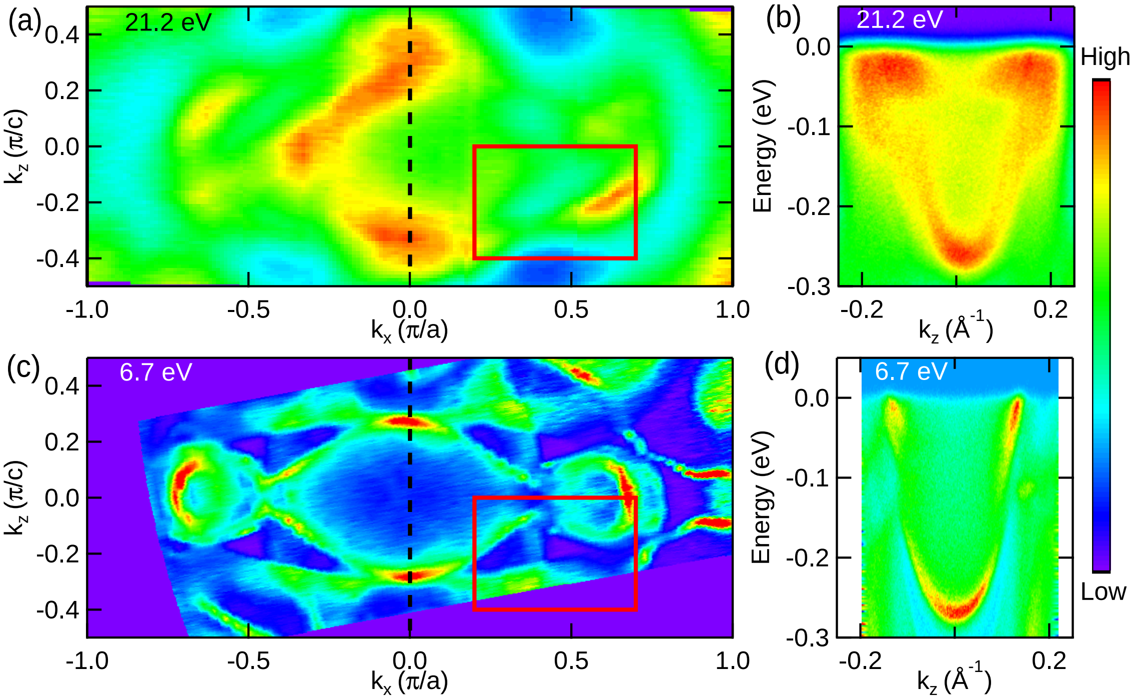

Figure 2.5 Fermi surface plots and band dispersion of $PtSn_4$ measured at photon energies of 21.2 and 6.7 eV. (a) Fermi surface plot of ARPES intensity integrated within 10 meV about the chemical potential measured at photon energy of 21.2 eV. (b) Band dispersion along the black dashed line in panel (a). (c) Fermi surface plot of ARPES intensity integrated within 10 meV about the chemical potential measured at photon energy of 6.7 eV. (d) Band dispersion along the black dashed line in panel (c).

ARPES system. Panels (c) and (d) show the ARPES intensity measured at the photon energy of 6.7 eV in the tunable laser-based ARPES system. By comparing panel (a) with (c), we can clearly see that the features on the Fermi surface can be better resolved in the low photon energy measurements. The band dispersion in panel (d) is much sharper and has much higher momentum resolution than the one in panel (b). However, we should also be cautious that the electron analyzer in the laser ARPES system is more advanced (Scienta R8000) compared to the one in the He-lamp ARPES system (Scienta SES2002), which will also affect the momentum and energy resolution of the ARPES intensity. Although lowering the incident photon energy could be one possible way to improve the momentum resolution in the ARPES experiment, sufficiently high photon energies are needed in order to excite the electrons with enough energy to overcome the potential barrier on the sample surface, i.e., the work function (typically 4–5 eV in the metal). In addition, there is a drawback in using low photon energy to measure the Fermi surface of the sample. As we can see in Figs. 2.5(a) and (c), the Fermi surface plot from higher photon energy (21.2 eV) covers more area (larger momentum space based on Eq. 2.3) in the Brillouin zone than the one from lower photon energy (6.7 eV). Thus, we sacrifice the range of momentum space available for study when using low photon energies for ARPES measurements, which could be a nightmare if the area of interest lies outside of the probing range.

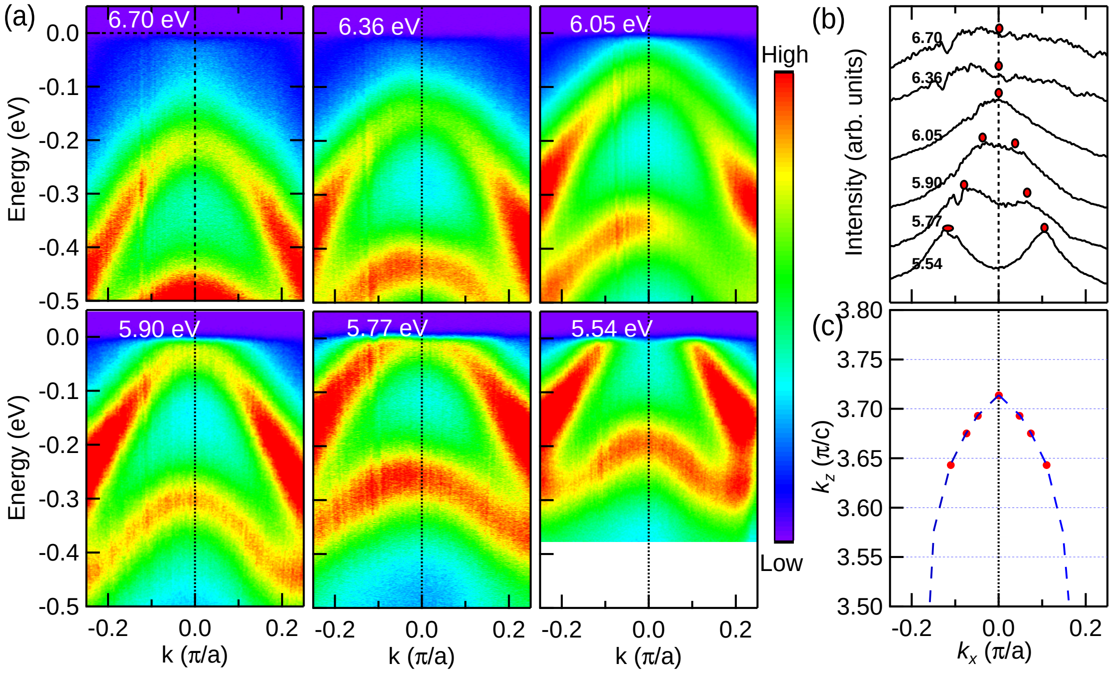

Figure 2.6 Band dispersion of YSb measured at various photon energies. (a) Band dispersion of YSb measured at photon energies of 6.70, 6.36, 6.05, 5.90, 5.77, and 5.54 eV, respectively. (b) Momentum dispersion curves at the Fermi energy extracted from panel (a). (c) k_z dispersion of YSb.

Besides the momentum resolution difference demonstrated in Fig. 2.5, another important feature should be noted: the Fermi surface plots in Figs. 2.5(a) and (c) are not exactly the same (one example is the same area enclosed by the red solid boxes), even though the band dispersions along the center cuts look similar to each other at different photon energies. This difference in Fermi surface plots is due to the fact that with one single incident photon energy, we are probing the Fermi surface along a spherical cut in a three-dimensional momentum space. By varying incident photon energies, we can probe the Fermi surface at various values of the k_z momentum (i.e. roughly equal to radius of the sphere). For sample with strong three dimensional character of the electronic structure, we can tune the incident photon energies to determine the k_z dispersion of the sample. Fig. 2.6 shows the band dispersion of YSb measured at photon energies of 6.70, 6.36, 6.05, 5.90, 5.77, and 5.54 eV, respectively. Two hole bands can be clearly seen in the band dispersion measured at the photon energy of 6.70 eV. As the incident photon energy decreases, the top hole band continuously moves up and touches the Fermi level at the photon energy of 6.05 eV. By further decreasing the incident photon energy, we can see that the top hole band crosses the Fermi level and forms a hole pocket. The size of the hole pocket increases continuously as the probing photon energy decreases. Fig. 2.6(b) presents the momentum dispersion curves (MDCs) at the Fermi energy extracted from the plots in panel (a). The peak positions of the MDCs are extracted by fitting a double-Lorentzian function to the curve, which denote the Fermi surface sheet along the out of plane direction. Panel (c) summarizes the k_z dispersion of YSb with an ellipse shape based on panel (b). The above data demonstrate the ability of probing the k_z dispersion of the sample by tuning the incident photon energies. We should also note that with the limited tunability of the photon source, only partial k_z dispersion can be measured as shown in Fig. 2.6(c).

Another important aspect of the photon sources is that the kinetic energy of the photoelectrons will depend on the photon energy used. This leads to different mean free paths in the sample as shown in Fig. 2.7. The mean free path is an indicator of how far a photoelectron on average will travel through a solid without scattering (loss of momentum/energy information). This is essential for the second step of the photoemission process, where we assume that no energy loss and change of momentum occurs. As we can see from the “Universal Curve”, the most commonly used photon energies in an ARPES experiment fall into the range of about 20–100 eV, which is sitting at the bottom of the curve. This leads to the fact that the common ARPES experiment is basically probing the top few layers of the crystal ($\sim$ 10 Å), i.e., it has high surface sensitivity. On the other hand, with low photon energy of around 6 eV (laser photon source) and high photon energy of around 1000 eV (synchrotron radiation photon source),

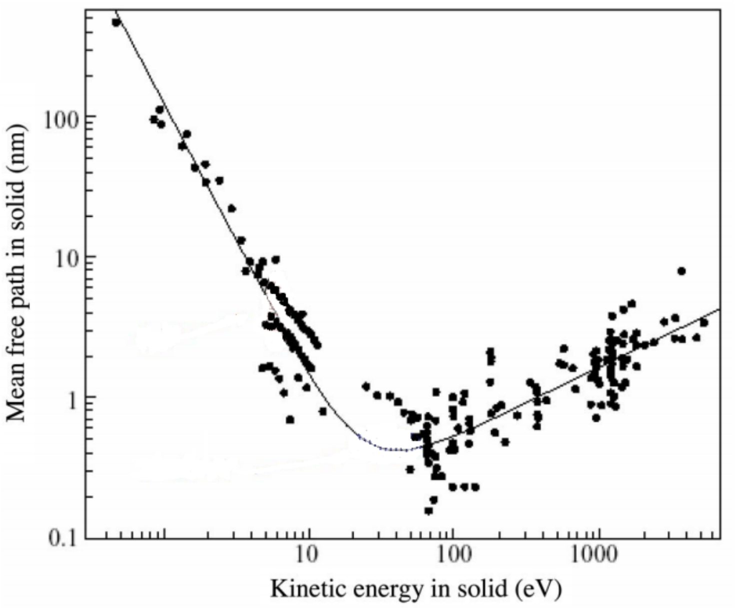

Figure 2.7 Universal curve of the electron mean free path in solids. (From Ref. [64])

the electron mean free path is almost an order of magnitude larger. Thus, the ARPES measurements would have higher bulk sensitivity by using low energy laser or high energy synchrotron radiation. Therefore, the range of the incident photon energies should be used depending on which property, surface or bulk, we are most interested in.

In the following sections, we will cover three most commonly used photon sources, namely He-lamp, synchrotron radiation, and laser in ARPES experiments.

2.2.1.1 He-discharge lamp

He-discharge lamp (we commonly refer to as He-lamp for short) belongs to a family of artificial light sources called gas-discharge lamps. Gas-discharge lamps generate light by sending an electrical discharge through an ionized gas, a plasma. Collisions between the electrons and the atoms in the plasma will excite the atoms to a higher energy state. When the excited atoms de-excite to a lower energy state (or ground state), a photon with the characteristic energy equal to the energy difference between these two states will be emitted. In a typical DC-powered gas-discharge lamp system, a noble gas such as neon inside the lamp tube is ionized, and

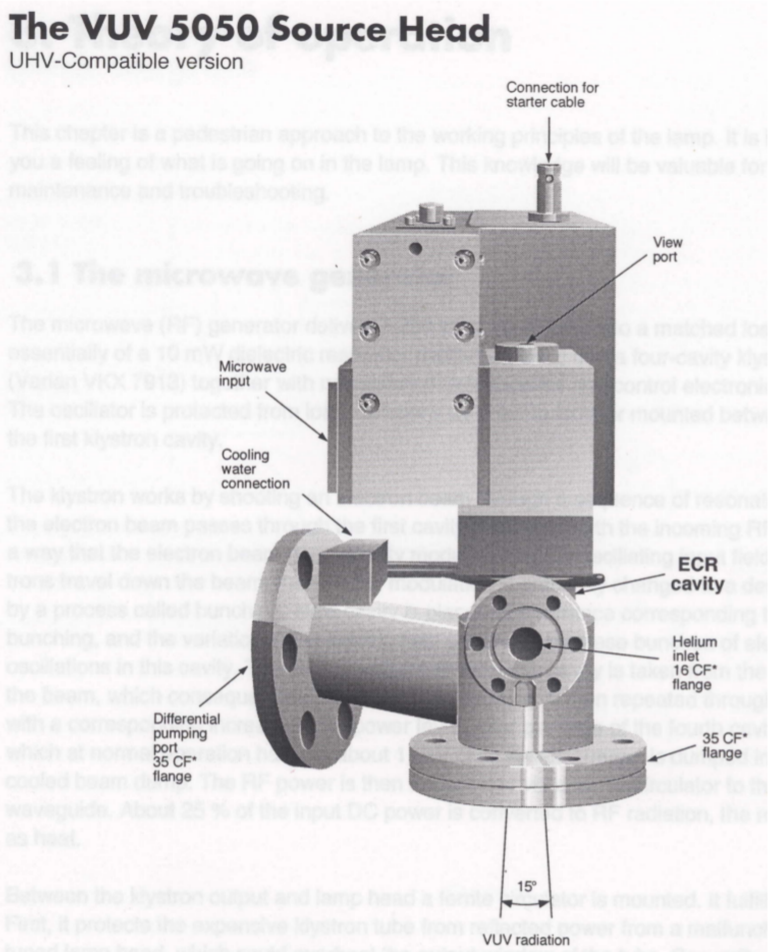

Figure 2.8 VUV 5050 source head. (From Ref. [65])

electrical discharge is produced by applying a high DC voltage between two electrodes. The electrons need to travel a finite distance to gain enough energy to excite the atoms in the plasma. Thus, relatively high gas pressure, sufficiently high voltage, and finite dimensions are required to have a sufficiently intense photon source.

Another type of gas-discharge lamps has taken advantage of the electron cyclotron resonance (ECR). An electron with charge e, mass m, and velocity v travelling perpendicular to a magnetic field B will form a circular orbit with angular frequency $\omega = eB/m$. Thus, a typical electron has a free travel distance considerably longer than the cavity dimensions and leads to increased ionization probability at a relatively low gas density. On the other hand, since the frequency of revolution is independent of the velocity, a radio frequency (RF) oscillating electric field

Table 2.1 Spectral lines of helium plasma (From [65])

Spectral Line	Energy (eV)	Intensity (%)
HeI α	21.2182	≈ 88
HeI β	23.087	≈ 5
HeI γ	23.743	≈ 1
HeI δ	24.045	< 0.2
HeII α	40.814	≈ 5
HeII β	48.372	≈ 0.5
HeII γ	51.017	≈ 0.1

with its field vector perpendicular to the B-field can be applied to couple with the plasma in the device to constantly accelerating the electrons. When compared to the DC-powered gas-discharge lamp, the ECR discharge lamp can operate at a much lower gas pressure and much smaller volume. Furthermore, the positive ions in the ECR discharge are not coupled to the RF due to its much larger mass. Thus, the kinetic energy of the ions reaching the cavity walls is fairly low ($\sim$ 10 eV) comparing to the ones in the DC-powered discharge ($\sim$ 500 eV). This results in much slower sputter wear rate of the cavity wall in the ECR discharge system than that of the anode in the DC-powered discharge system.

Fig. 2.8 shows a VUV 5050 source head in the Scienta VUV 5000 photon source system. The light source is based on a helium plasma, generated with the ECR technique. The microwave generator (10 GHz) is coupled to a small discharge cavity in a magnetic field tuned to the microwave frequency to meet the ECR condition. Cooling water must be supplied during operation to avoid the melting of the waveguide soldered joints, which may lead to injury from the escaping microwave radiation. The view port can be used for alignment and visual inspection of the discharge.

Table 2.1 shows the energies and relative intensities for the most intense spectral lines in a He-discharge lamp. Since the HeI α line is emitted with roughly 90 % of the total intensity, there is almost no need for a monochromator in the VUV 5000 photon source. For ARPES experiments, we typically use HeI α and HeII α lines. HeI α line has a photon energy of 21.2 eV and is mainly used for band dispersion measurements and Fermi surface mapping. Due to

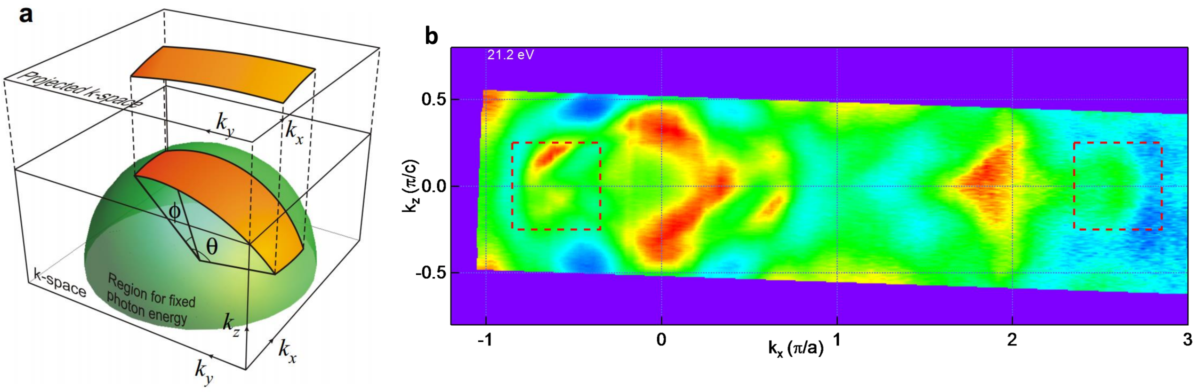

Figure 2.9 (a) Schematics of the Fermi mapping. (From Ref. [66]) (b) Fermi surface of $PtSn_4$ measured with HeI α spectral line (21.2 eV photons).

the relatively high energy photons in the HeI αline, it can probe the second Brillouin zone of most materials. This can be demonstrated in the ARPES measurements of $PtSn_4$.

The photoelectrons at the Fermi surface emitted by fixed-energy photons span a spherical surface at the three dimensional k-space as shown in Fig. 2.9(a). Therefore, for Fermi surface measured at large θ (second Brillouin zone in the following case), the k_z value could be different from the Fermi surface in the first Brillouin zone. This difference would be evident if the material has strong three-dimensionality of the electronic structure. Fig. 2.9(b) shows the Fermi surface measured by HeI α spectral line, where the Fermi surface sheets in the first and second Brillouin zones are observed close to the zone centers ($k_x = 0$ and 2, respectively). The difference between these two Fermi surface sheets can be clearly seen in the red dashed boxes, which should be symmetric if they are at the same location along the out of plane direction. These results (Fig. 2.5 and Fig. 2.9) have demonstrated the strong three-dimensionality of the electronic structure in $PtSn_4$, which is consistent with the band structure calculations in Ref. [67].

For HeII α line with photon energy of 40.8 eV, it can either be used to measure the band dispersion and Fermi surface, or to determine the chemical composition on the surface of the sample like an XPS. Fig. 2.10 shows an example of using HeII α to detect the Pb deposition on the surface of a Si (111) plate. In panel (a), we can clearly see one dispersion sitting at the binding energy of $\sim$ 3 to 4 eV, and two dispersionless peaks sitting at the binding energies of

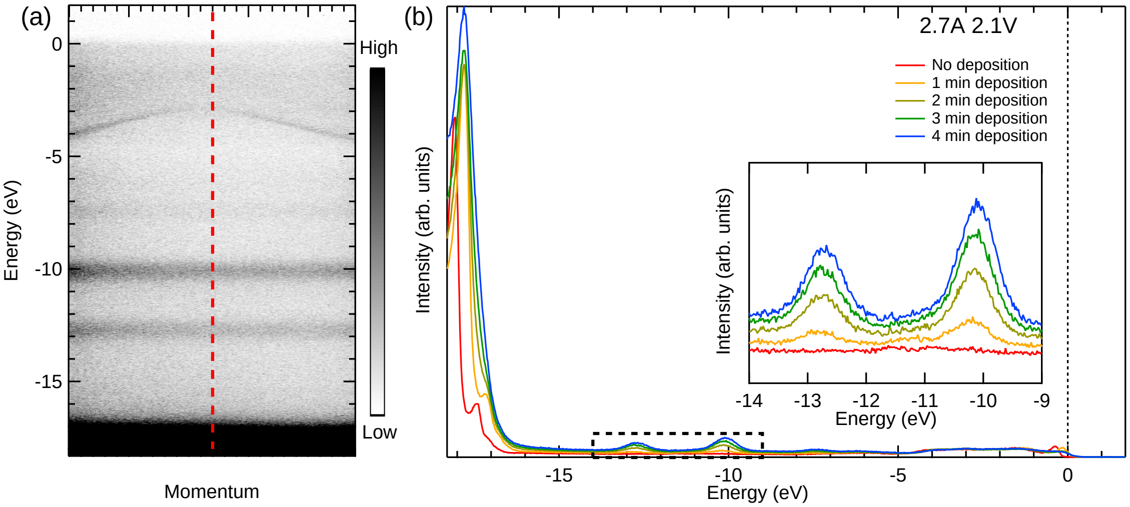

Figure 2.10 HeII α measurements of Pb deposition on Si (111) surface. (a) ARPES intensity measured after 4-min Pb deposition (2.7 A and 2.1 V applied on Pb source). (b) Energy dispersion curve [red dashed line in panel (a)] integrated over the whole momentum range. Inset shows the zoom-in image of the black dashed box.

$\sim$ 10 and 13 eV after 4-min Pb deposition. The band with dispersion comes from the Si(111) substrate and the dispersionless peaks come from core levels of Pb deposited on the surface of the substrate. Panel (b) shows the energy dispersion curve [along the red dashed line in (a)] integrated over the whole momentum range prior to deposition, and 1- to 4-min Pb deposition. The inset shows the zoom-in image of the black dashed box, where two peaks at the binding energies of $\sim$ 12.8 and 10.1 eV continuously grow in intensity with longer Pb deposition time. This figure demonstrates the ability of using HeII α line to probe the band dispersion of the material and the chemical composition on the sample surface at the same time.

2.2.1.2 Synchrotron Radiation

Although He-lamp photon source can provide us with relatively high intensity photon beam, the usable photon energies are limited to 21.2 (HeI α) and 40.8 eV (HeII α). As we have discussed at the beginning of this section, the ability to tune the incident photon energies continuously is very important for probing the momentum dispersion along the out of plane direction. Therefore, synchrotron radiation with large range of tunable photon energies is an important tool in photoemission studies. Synchrotron radiation photon beams are produced

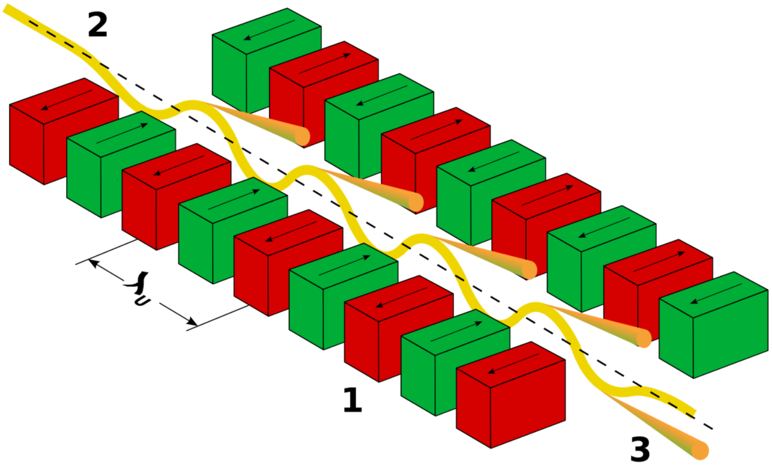

Figure 2.11 Undulator used in the synchrotron radiation center. (from Ref. [68])

by radially accelerating charged particles, using bending magnets, undulators and/or wigglers. In most ARPES experiments, undulators are commonly used.

Fig. 2.11 shows a schematic of the undulator. It consists of a periodic structure of dipole magnets, which produces a static magnetic field alternating along the length of the undulator with a periodicity of λ_u. Electrons travelling in this periodic magnetic field are forced to undergo oscillations and thus to radiate energy. The radiation produced in an undulator has high intensity and is collimated on the orbit plane of the electrons. After exiting the undulator, the radiation is monochromatized at the desired photon energy by a grating monochromator, and is focused on the sample. The advantage of using a synchrotron radiation is that it offers a wide range of spectral, from the visible to the x-ray region, with an intense and highly polarized continuous spectrum [60]. Thus, ARPES experiment with this type of photon source can probe several Brillouin zones of the sample along the in-plane and out-of-plane directions, which is often used to determine the $k_\perp$ dispersion and inner potential V_0 of the material as we have discussed in the previous sections.

Fig. 2.12 shows the ARPES intensity and k_z dispersion of YSb measured at Synchrotron Radiation Center (University of Wisconsin - Madison) at photon energies from 30 to 76 eV with 2 eV step. Panel (a) shows the band dispersions from several photon energies as marked at the top left corner of each plot. We can clearly see that the hole pocket size changes with the

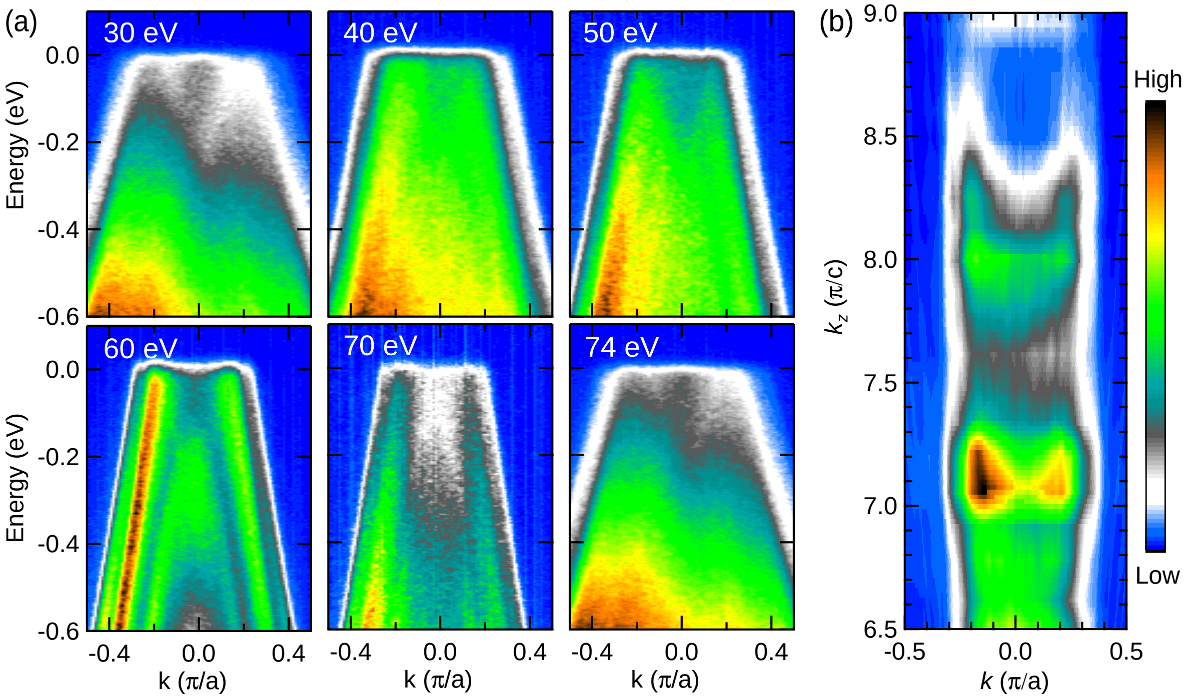

Figure 2.12 Synchrotron radiation based ARPES measurements of YSb. (a) Band dispersion measured at photon energies of 30, 40, 50, 60, 70, and 74 eV. (b) k_z dispersion of YSb measured at photon energies from 30 to 76 eV with 2 eV step.

incident photon energy. By stacking the band dispersions from various photon energies together and extracting the ARPES intensity at the Fermi level, k_z dispersion can be constructed as shown in panel (b). Comparing to Fig. 2.6, it is obvious that ARPES measurements using synchrotron radiation source cover much wider momentum space in the out-of-plane direction. There is only a half ellipse shape in Fig. 2.6, whereas several ellipses can be seen in Fig. 2.12. These results demonstrate the advantage of the synchrotron radiation source for studies requiring wide k_z scans.

2.2.1.3 Laser ARPES

Although synchrotron radiation can provide us wide range of photon energies, the experiment time (beamtime) in synchrotron radiation centers is limited. Researchers working on synchrotron radiation ARPES experiments will have to work 24 hours a day continuously for several days in order to take full advantage of the precious time. A tabletop photon source

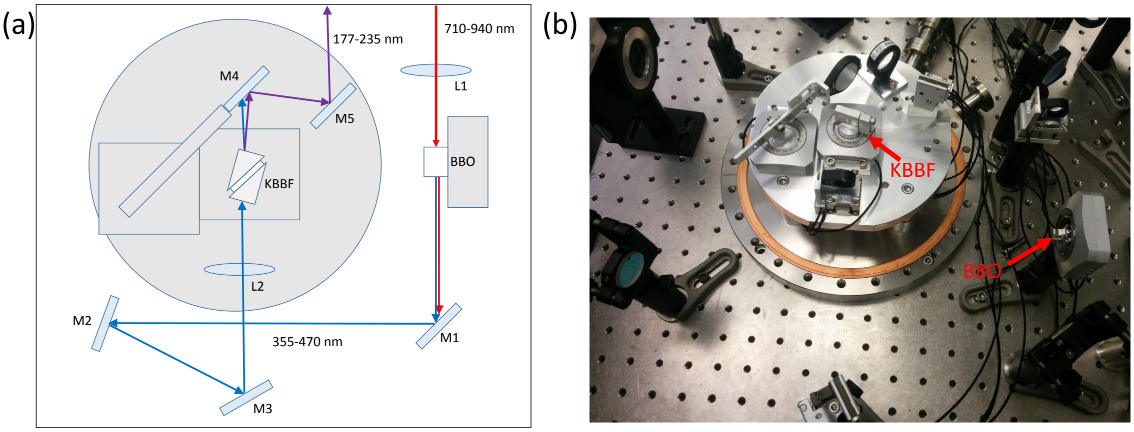

Figure 2.13 (a) Schematic layout of the fourth-harmonic generation. Red, blue, and purple arrows indicate the optical path for fundamental, second-harmonic generation, and fourth-harmonic generation photon beam, respectively. (b) Picture of the optical components layout. Red arrows point to the KBBF and BBO crystals, respectively.

with energy tunability is therefore very desirable. Tunable laser becomes the natural choice.

Fig. 2.13(a) shows the schematic layout of the fourth-harmonic generation (FHG) in our laser ARPES system. An infrared (IR) beam with wavelength of 710-940 nm (red arrows) is produced by Ti:sapphire laser. After being focused by lens L1, the IR beam passes through BBO crystal with doubled frequency, i.e., with wavelength of 355-470 nm (blue arrows). After being reflected by several mirrors, the second-harmonic laser beam goes through the KBBF crystal and its frequency doubles again, resulting in the fourth-harmonic laser beam. The outgoing fourth-harmonic laser beam has wavelength between 177 and 235 nm (corresponding to photon energies of 7 and 5.3 eV, respectively). Since the typical work function in the metal is roughly 4 to 5 eV, the fourth-harmonic laser beam has sufficiently high photon energy for the ARPES experiment. Fig. 2.13(b) shows a picture of the optical components in the laser ARPES system, where the red arrows point to the KBBF and BBO crystals. Since UV photons with wavelength of below 200 nm are readily absorbed by oxygen, it is important to enclose the fourth-harmonic generation part in a rough vacuum ($\sim$ 10 mTorr). This layout design is modified based on the original design in Ref. [69] to have a more compact stage for fourth-harmonic generation; thus, it is easier to enclose in a vacuum chamber.

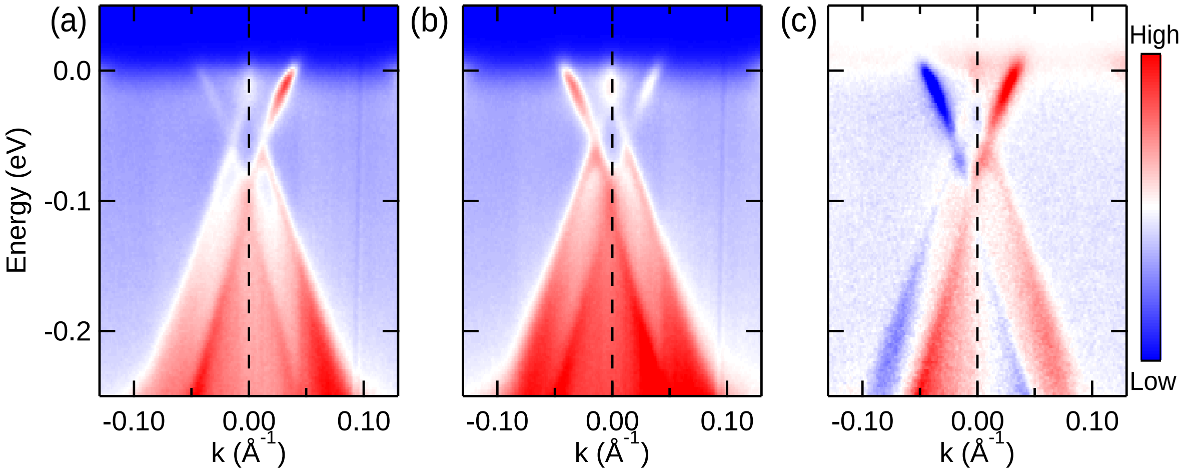

Figure 2.14 Circular dichroism of $PtSn_4$. (a) ARPES intensity at X point of $PtSn_4$ measured with right-handed circularly polarized light. (b) ARPES intensity at X point of $PtSn_4$ measured with left-handed circularly polarized light. (c) ARPES intensity of (a) subtracting (b).

Due to its relatively low photon energies, laser photon source results in higher momentum resolution in the ARPES measurements as shown in Fig. 2.5. Another advantage of the laser photon source is that its polarization can be easily changed from linearly polarized light to circularly polarized by inserting a quarter-wave plate in the beam path. Furthermore, left- and right-handed circularly polarized light can also be achieved by using a half-wave plate. Taking advantage of the left- and right-handed light, circular dichroism can be utilized to study the spin texture in topological insulators [19, 70].

Fig. 2.14 shows the circular dichroism of $PtSn_4$. Panels (a) and (b) show the ARPES intensity at X point of $PtSn_4$ measured with right- and left-handed circularly polarized light, respectively. We can clearly see the intensity difference in these two plots. The ARPES intensity measured with right-handed circularly polarized light has higher intensity on the right side of the Dirac dispersion, while the other one shows the opposite. By subtracting ARPES intensity of (b) from (a), we can see the difference of these two measurements more clearly [shown in panel (c)]. The Dirac dispersion on the left hand side has the opposite polarization dependence of the intensity compared to the one on the right hand side. These plots demonstrate the ability of measuring circular dichroism in the laser ARPES system. However, we should note that

Table 2.2 Comparison of photon sources (Adopted from [71])

	Helium-lamp	Synchrotron radiation	Laser
Photon energy (eV)	21.2, 40.8	20–1000	5.3–7
Intensity (photons/s)	10^{13}	10^{12}	10^{15}
Energy resolution (meV)	~ 8	1-50	< 1
Momentum resolution (Å^{-1})	10^{-2}	10^{-1}	10^{-3}
Time resolved	none	$\sim$ 10 ns	100 fs – ps
Polarization	unpolarized	changeable	easy to change
Bulk sensitivity (ML)	~ 5	~ 50	10–100
Spot size	1 mm	50 μm	1– 30 μm
Momentum range	2 BZ	several BZ	partial BZ

detailed analysis of the matrix elements, selection rules, and experimental geometry for the circularly polarized light used in these measurements is needed. Further theory is required to better understand the Dirac state in $PtSn_4$.

The properties of these photon sources used for ARPES experiment are summarized in Table 2.2. We can clearly see that the advantages of the laser photon source are high intensity, high energy and momentum resolution, easy to change polarization, bulk sensitivity, and small spot size. However, due to its low photon energy and fairly small tunability, laser-based ARPES system can only probe partial Brillouin zone (BZ) of the sample [see Fig. 2.5(c)]. Thus, He-lamp and Synchrotron radiation ARPES experiment are essential to determine the whole BZ information.

2.2.2 Electron Analyzer

Apart from the photon source, electron analyzer is another essential part of an ARPES system. Fig. 2.15 shows a schematic of the Scienta hemispherical analyzer. A conventional hemispherical electron analyzer consists of multielement electrostatic lens, a hemispherical energy analyzer with entrance slits, and an electron detector. The electrostatic lens collects the electrons from the sample and transfers them to the entrance slit of the energy analyzer. The lens serves mainly three purposes: (1) physically separates the sample region from the electron analyzer for better accessibility of the sample, (2) acts as focusing lens to produce a photoelec-

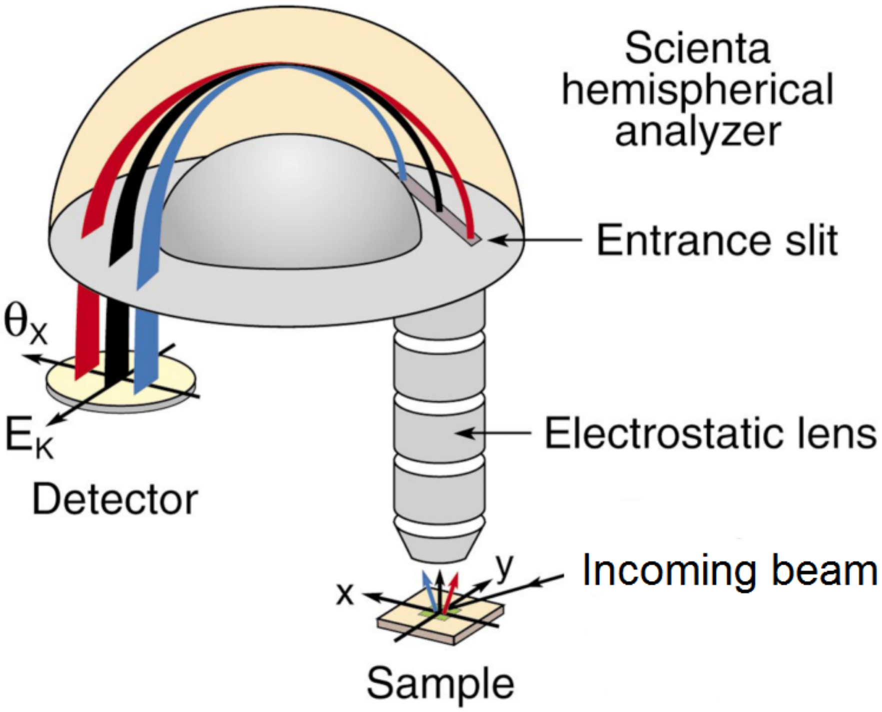

Figure 2.15 Schematic of the Scienta hemispherical electron analyzer. The red, black, and blue beams represent photoelectrons with different emission directions. Within the same beam, photoelectrons with different energies are present. (Adopted from Ref. [60])

tron image of the sample on the entrance plane of the analyzer, (3) matches the initial kinetic energy of the electrons to the pass energy of the analyzer. The electron energy analyzer is the part of the instrument that measures the actual energy dispersion and consists of two concentric hemispheres of radius R_1 and R_2. These two hemispheres are kept at a potential difference ΔV, so that only those electrons reaching the entrance slit with kinetic energy within a narrow range centered at the pass energy E_{pass} can pass through this hemispherical capacitor. The pass energy E_{pass} has the following form,

$$E_{pass} = \frac{e\Delta V}{(R_1/R_2 - R_2/R_1)} \tag{2.21}$$

In this way it is possible to measure the kinetic energy of the photoelectrons with an energy resolution given by

$$\delta E_a = E_{pass}(\frac{w}{R_0} + \frac{\alpha^2}{4}) \tag{2.22}$$

where $R_0 = (R_1 + R_2)/2$, w is the width of the entrance slit, and α is the acceptance angle ($\sim 14^\circ$ in the He-lamp ARPES system with a SES2002 electron analyzer and $\sim 30^\circ$ in the laser ARPES system with a R8000 electron analyzer). Due to the spherical symmetry, electrons pass through a straight slit with width < 1 mm will be imaged onto a curved line at the detector with a radius half of the analyzer (the effect can be neglected for relatively wide slits). Thus, the narrower slits are curved with the appropriate radius to produce straight lines at the detector, which yields higher energy resolution but lower sensitivity. Typically a slit carousel is used with various widths and shapes (straight or curved) to facilitate the choice of a suitable compromise between resolution and sensitivity. The electron detector consists of two micro-channel plates (MCP), a phosphor screen, and a CCD camera, which is responsible for detecting electrons and measuring their energy and momentum. The MCP pair multiplies each incoming electron $\approx 10^6$ times and this electron pulse is accelerated to the phosphor screen to produce a light flash, which can be captured by the CCD camera. As shown in Fig. 2.15, after the electrons inside the sample get excited by the incoming photon beam, the electrons escape the sample surface in various directions (denoted by the red, black and blue arrows). After being focused by the electrostatic lens onto the entrance slit, electrons with the same outgoing direction (momentum) but different energies will be deflected by the electron energy analyzer and finally get collected by the detector with both energy and momentum resolved [60, 72]. Figs. 2.14(a) and (b) show typical ARPES intensities measured at the detector with red and blue color scale.

2.2.3 Ultrahigh Vacuum

In the ARPES experiment, ultrahigh vacuum is required mainly for two reasons: (1) the photoelectrons need to travel relatively long distance (~ 2 m) to the electron detector without collision with gas molecules in the system, (2) fresh sample surface needs to be maintained since most of the ARPES measurements are probing the top few layers of the sample. In order to satisfy the first condition, a vacuum of 10^{-4} Torr is enough by doing rough estimation using the kinetic theory. In kinetic theory, the mean free path of a particle is $l = (n\sigma)^{-1}$, where n is the density of the particles, and σ is the effective cross-sectional area for collision. Using ideal gas law, we have $n = N/V = p/(k_B T)$, where k_B is the Boltzmann constant ($\sim 1.38 \times 10^{-23} J \cdot K^{-1}$), and room temperature $T = 300K$. The effective cross-section area can be estimated using the radius of the gas particle in the system, $\sigma = \pi \cdot r^2$, where r is the radius of the gas particle ($\sim$ 1 Å). Thus, we would have

$$p \sim \frac{k_B T}{\pi r^2 \cdot l} \sim \frac{1.38 \times 10^{-23} J/K \times 300K}{3.14 \times (10^{-10} m)^2 \times 2m} \sim 0.066 \text{ Pa} \sim 5 \times 10^{-4} \text{ Torr} \tag{2.23}$$

However, the second condition cannot be easily satisfied. From the surface science lectures, we know that the gas flux can be written as

$$Z_w = \frac{dN_f}{dt} = \frac{P}{\sqrt{2\pi m k_B T_g}} \tag{2.24}$$

where N_f is the total number of particles striking the surface per unit area, m is the particle mass, k_B is the Boltzmann constant, and T_g is the gas temperature (300 K). Thus, we can calculate the number of particles striking on the surface based on the above equation. An another easy way to estimate this value is to take advantage of the Langmuir's Rule

$$\#L = P \times t \times 10^6 \tag{2.25}$$

where L stands for 1 monolayer of gas particles on the surface, P is the gas pressure with unit of $Torr$, and t is the time with unit of s. Thus, in order to measure the samples with less than one monolayer of gas particles covered on top for one day, the minimum pressure would be 1×10^{-11} Torr assuming that each and every gas particle hitting on the sample surface sticks on the surface. Normally, pressure below 1×10^{-10} Torr in the ARPES system is sufficient for basic measurements for a few days or even weeks. In order to achieve ultrahigh vacuum in the ARPES system, "baking" the system is necessary to desorb gases from the chamber walls. Typical temperature for baking is around 120 °C to 150 °C based on the maximum allowed temperature of each component in the ARPES system. After two or three weeks of baking,

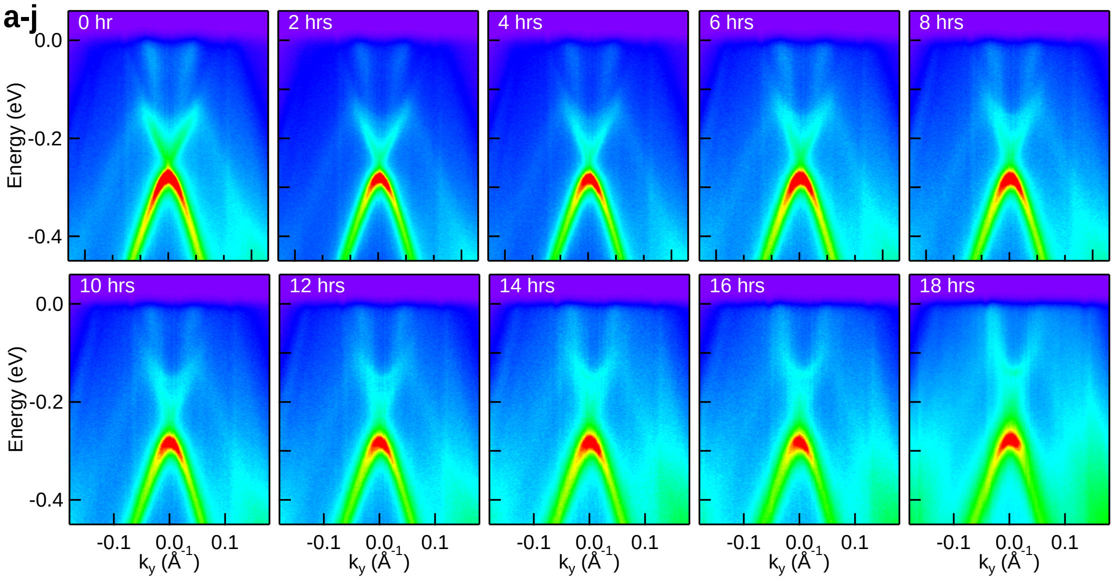

Figure 2.16 Time dependence of the band dispersion in LaBi. (a)–(j) Band dispersion of LaBi measured at photon energy of 6.7 eV, temperature of 40 K, and time of 0 to 18 hours after cleaving *in situ*.

most of the residue gases inside the ARPES main chamber would be H_2, N_2, and CO_2 and a ultrahigh vacuum of 5×10^{-11} Torr can be achieved. However, for samples such as LaBi, even though ultrahigh vacuum is maintained in the system, the measured spectrum changes with time due to deposition of contaminants on the surface.

LaBi is an air sensitive material that may react to O_2, water, N_2, or CO_2. Even though the sample is measured under a vacuum better than 8×10^{-11} Torr, its band structure evolves slowly but significantly with time. Fig. 2.16 shows the time dependence of the band structure in LaBi measured at the photon energy of 6.7 eV and temperature of 40 K. We can clearly see the top cone of the Dirac dispersion at the binding energy of $\sim$ 200 meV after fresh cleaving [Fig. 2.16(a)]. However, as time goes by to 10 hours after cleaving, the intensity of the top cone is smeared out [Fig. 2.16(f)]. After 16 hours, the top cone of the Dirac dispersion cannot be clearly resolved as shown in Fig. 2.16(i). These results show strong variation of the measured band structure in LaBi with time. Therefore, all the measurements need to be completed on a freshly cleaved sample within a relatively short time (a couple of hours) to ensure that the intrinsic band structure of LaBi is obtained.

2.2.4 Cold Head

The ability to control the sample temperature is very important for studying interesting temperature dependent physical properties, such as superconductivity, ferromagnetic and antiferromagnetic (AFM) phase transitions, temperature-induced Lifshitz transitions and etc.

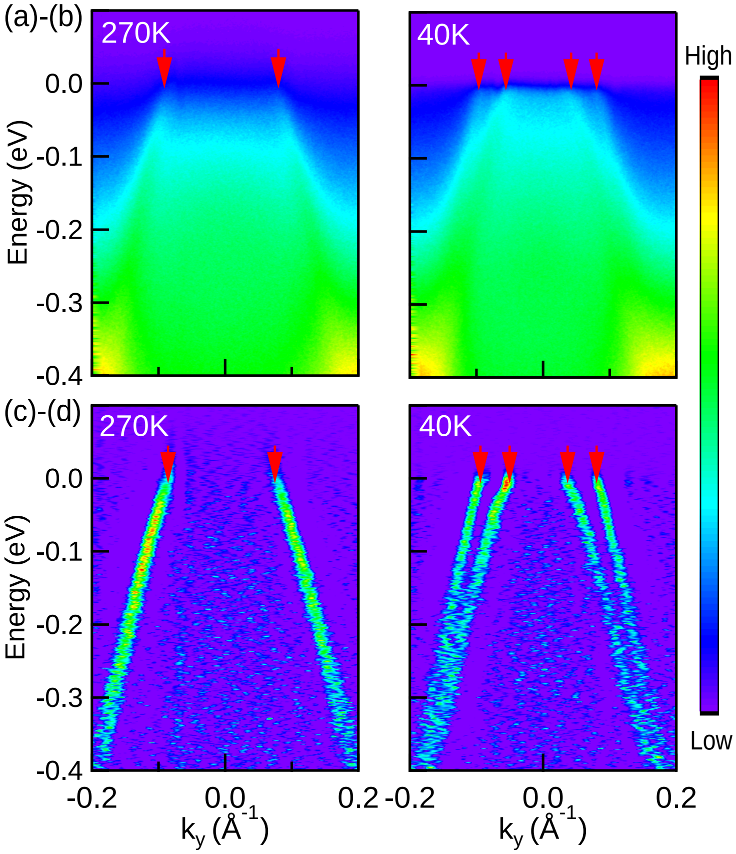

Figure 2.17 Band dispersion of $CrAuTe_4$ measured at photon energies of 6.70 eV. (a)-(b) ARPES intensity measured at $T = 270$ and 40 K, respectively. (c)-(d) The intensity plots of the second derivatives of data in (a) and (b). The red arrows mark the Fermi crossings. (From Ref. [73])

Fig. 2.17 shows the band dispersion of $CrAuTe_4$ measured at the photon energy of 6.70 eV and temperatures of 270 and 40 K. $CrAuTe_4$ has an AFM transition at 255 K as shown in the magnetization data and temperature dependent resistivity measurements [73]. As we can see in Fig. 2.17, the band dispersion measured at 270 K (above the AFM transition temperature of 255 K) shows only a single hole pocket (marked by the red arrows). When the sample

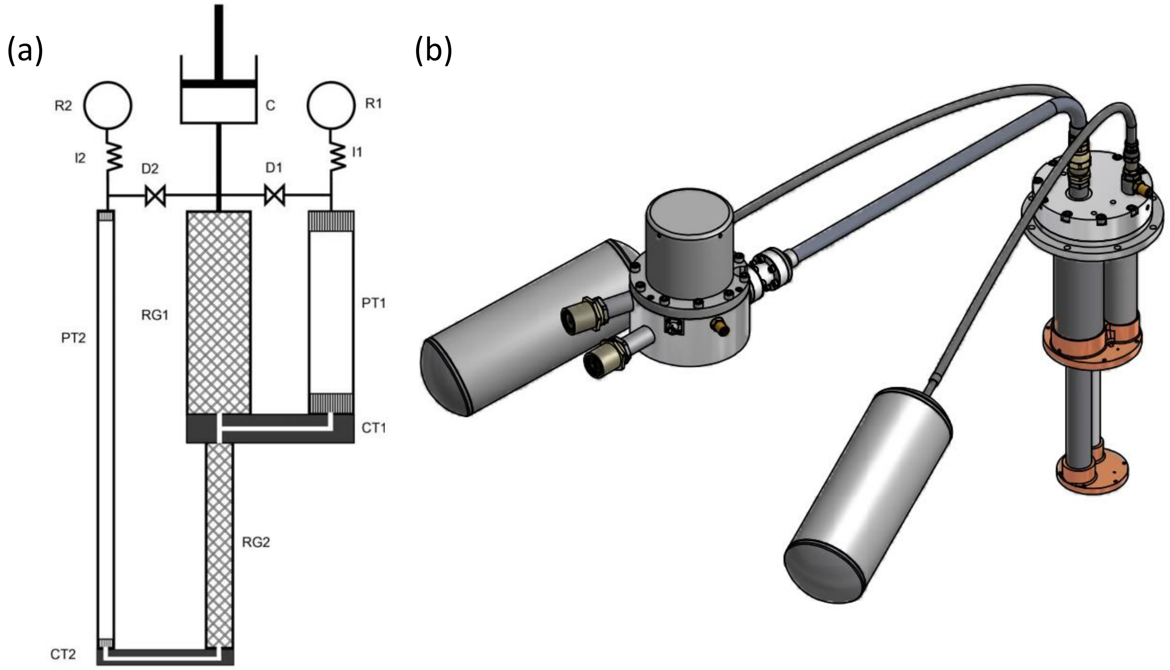

Figure 2.18 (a) Schematic of the two-stage pulse tube crycooler with gas-coupled stages. C: compressor; R1, R2: reservoirs; PT1, PT2: pulse tubes of first and second stage; RG1, RG2: first stage and second stage regenerator; CT1, CT2: cold tips; I1, I2: inertance lines; D1, D2: second-inlet valves. (b) Schematic outline drawing of PT415 cryorefrigerator with remote motor option from Cryomech, Inc. (From Ref. [74, 75])

temperature is cooled down to 40 K, another hole pocket emerges in the center [panel (b)]. To better illustrate the band dispersion, we calculate and plot the second derivative of the ARPES intensity in Figs. 2.17(c)-(d), where one hole pocket to two hole pockets transition can be clearly seen. This demonstrates the importance of precise sample temperature control in the ARPES measurements.

The most direct, yet not the most cost efficient way to cool down a sample is to use liquid Helium ($T = 4.2$ K) based on the lowest temperature that is required. Liquid He is very expensive and its use for ARPES measurements in laboratory environment is cost prohibitive. In our laboratory we use closed cycle refrigerator, which uses electrical energy and thermodynamics to cool down the samples.

Fig. 2.18 shows a schematic drawing of the two-stage pulse tube crycooler with gas-coupled stages. Both stages have a U-shaped configuration with the warm ends of the pulse tubes located at ambient temperature that is cooled by air flow during operation. The regenerator of the first stage serves for precooling of the Helium gas for both stages. At the cold end of the first regenerator the gas is split into one fraction that flows through the first stage pulse tube and another fraction that enters the second stage. The regenerator consists of a matrix of a solid porous material, through which the gas flows back and forth, and heat is stored and released periodically. This periodic gas flow is driven by the compressor and motor on top of the cold head which would cause vibration on the whole stage. In order to minimize the vibration in the system, we use PT415 cryorefrigerator with remote motor option to isolate the motor from the cold head [Fig. 2.18(b)]. The PT415-RM pulse tube refrigerator can achieve cooling power of 1.35 W at 4.2 K and 36 W at 45 K. This is more than sufficient to cool down samples below liquid He temperatures [75].

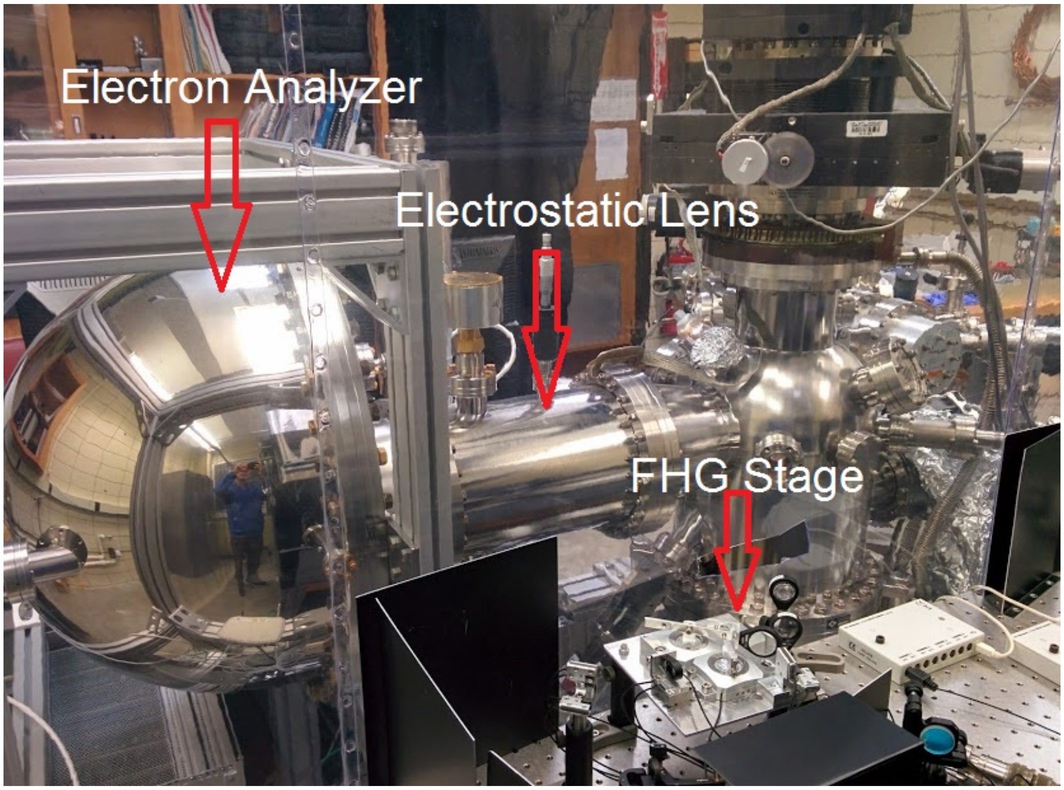

Figure 2.19 Laser ARPES system. The red arrows point to the electron analyzer, electrostatic lens, and FHG stage, respectively.

In summary, Fig. 2.19 shows a picture of the Laser ARPES system in our lab, which is the first operational tunable laser ARPES system in the world. Most of the data that will be shown in the following chapters are collected using this system. The red arrows point to the main components of the system, i.e., electron analyzer, electrostatic lens, and FHG stage. The cold head with 4-axis motion is not completely shown in this picture and will be replaced soon by PT415-RM cold head with lower temperature capability and minimum vibration. Except for the FHG stage (for now), all other components are under ultrahigh vacuum. Furthermore, in order to eliminate the earth magnetic field effect on the trajectory of the photoelectrons, magnetic shielding (μ-metal) and demagnetization of the inner components are essential in order to obtain reliable results from ARPES measurements.

2.3 Sample Preparation

After all the components in the ARPES system have been properly set up, the next step is to prepare "good" surfaces of the samples for measurements. As we have discussed in Section 2.1.1, in order to ensure that the parallel component of the photoelectron's momentum is conserved, the sample surface needs to be atomically flat. Furthermore, we cannot measure sample surfaces directly prepared in the open air, because they are covered by multiple layers of molecules as we have pointed out in Section 2.2.3. Thus, the sample surfaces need to be freshly prepared in the ultrahigh vacuum. There are three main methods of sample preparation: (1) cleaving (breaking) the sample in ultrahigh vacuum, (2) polishing the sample in open air, then sputter and anneal the sample surface in vacuum, (3) *in-situ* growth of thin films using molecular beam epitaxy (MBE) method. In our ARPES system, we do not have a MBE system yet, although we can do simple deposition like Pb, Au, Gd, K, and etc for magnetic/non-magnetic or electron/hole doping measurements. In the following sections, the first two methods will be discussed.

2.3.1 Cleaving

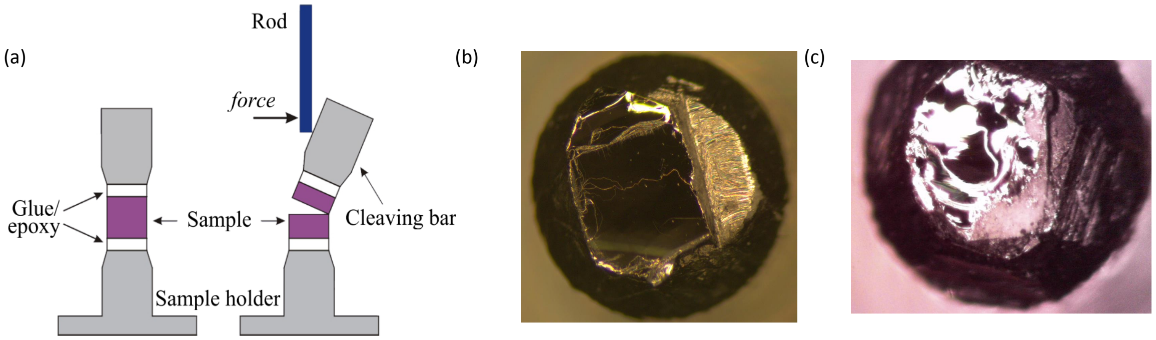

Figure 2.20 (a) Process of sample cleaving. A cleaving bar is attached to the sample before it is loaded; then it is removed mechanically inside the vacuum chamber. (Adopted from Ref. [66]) (b) Picture of a cleaved sample $PtSn_4$. (c) Picture of a cleaved sample $Ce_3Bi_4Pt_3$.

Fig. 2.20(a) shows the process of sample cleaving. First the sample is glued to the sample holder, which is usually made out of aluminium. Two types of glues can be used. One is silver epoxy, which is conductive itself. The other is Torr Seal high vacuum epoxy, which is not conductive and usually extra graphite paint is needed to ensure the sample is properly electrically connected to the system. After the sample is glued to the sample holder, a cleaving bar is glued on top of the sample. After the sample transferred into the ultrahigh vacuum system has been cooled down to the desired temperature for measurements, we use a rod (transfer arm) to push on the side of the cleaving bar and split the sample into two pieces as shown in Fig. 2.20(a). For samples with layered structure, such as $PtSn_4$, cleaving can produce beautiful atomically flat surface as shown in Fig. 2.20(b). With this nice cleaved surface, high resolution ARPES intensity can be obtained as shown in Fig. 2.5(c). However, for samples that do not have a layered structure, such as $Ce_3Bi_4Pt_3$, shiny surface may be obtained after cleaving [Fig. 2.20(c)]. This shiny but uneven cleaving surface usually produce high intensity of photoelectrons but poorly resolved momentum and energy information.

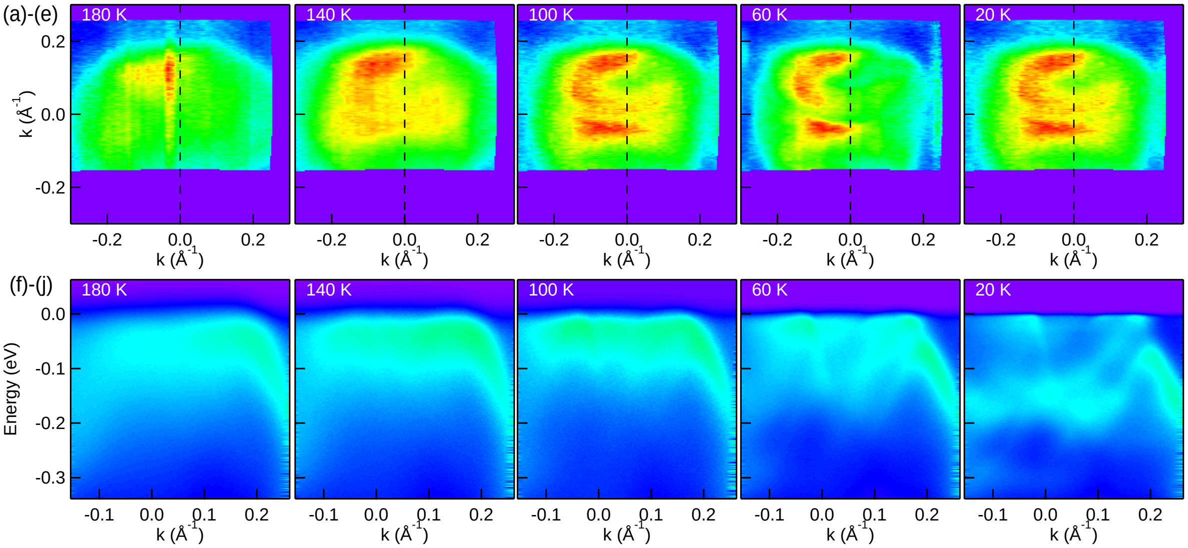

Figure 2.21 Fermi surface and band dispersion of $Bi_2Rh_3S_2$. (a)–(e) Fermi surface of $Bi_2Rh_3S_2$ measured at photon energy of 6.7 eV and temperature of 180, 140, 100, 60, and 20 K, respectively. (f)–(j) Band dispersion along the black dashed lines in (a)–(e), respectively.

An example of imperfect energy and momentum resolved ARPES measurements is $Bi_2Rh_3S_2$ (shown in Fig. 2.21). $Bi_2Rh_3S_2$ has a structural first-order transition at around 165 K [76]. As shown in Figs. 2.21(a)–(e), the Fermi surface evolves from mainly one big hole pocket at the temperature above the transition temperature of 165 K into two smaller pockets at temperatures below the transition temperature. Figs. 2.21(f)–(j) show the band dispersion along the black dashed lines in (a)–(e), respectively. New bands emerge starting at the temperature of 140 K and become significantly visible at 20 K. Even though we can see dramatic changes in the Fermi surface and band dispersion, all these features are very broad and not very well resolved. One reason may due to the imperfect cleaving of the sample of this material, and the other reason may due to the strong three-dimensionality of its electronic structure. Further band structure calculations are needed to verify the origin of the electronic structure transition.

2.3.2 Polishing, Sputtering, and Annealing

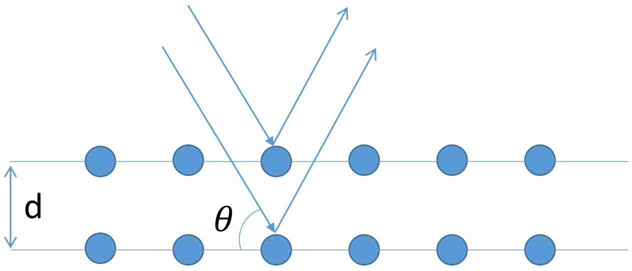

Figure 2.22 Bragg's Law. d is the distance between two diffraction planes, θ is the incident angle of the X-ray with respect to the diffraction plane.

For samples that cannot be cleaved properly, polishing is the other option to obtain a flat surface. Another benefit of using polishing is that we can almost choose any crystal orientation as needed. To determine the crystal orientation, back-reflection Laue system is used in our lab. In the back-reflection Laue system, the film for recording the backward diffraction beams is placed between the X-ray source and the crystal. The diffraction beams form arrays of spots, which satisfy the Bragg's law

$$2 \cdot d \cdot sin\theta = n\lambda \tag{2.26}$$

where d stands for the distance between the two diffraction planes, θ stands for the incident angle of the beam respect to the diffraction plane, and λ stands for the wavelength of the incident X-ray. Since we are using white X-rays (a full spectrum of many wavelengths), these X-rays will have the opportunity to be diffracted by different planes given that the value of λ satisfies the Bragg's law. Therefore, in Laue measurements, an array of spots corresponding to different orientations will be obtained.

Au_2Pb crystallizes in cubic Laves phase at room temperature, and is a topological superconductor candidate with a Dirac metal to topological metal transition along with a structural phase change [77]. Fig. 2.23 shows the pictures of Au_2Pb single crystals with different orientations and their corresponding Laue patterns. Fig. 2.23(a) shows the natural growth facet of a Au_2Pb single crystal, and panel (d) shows its corresponding Laue pattern with three-fold

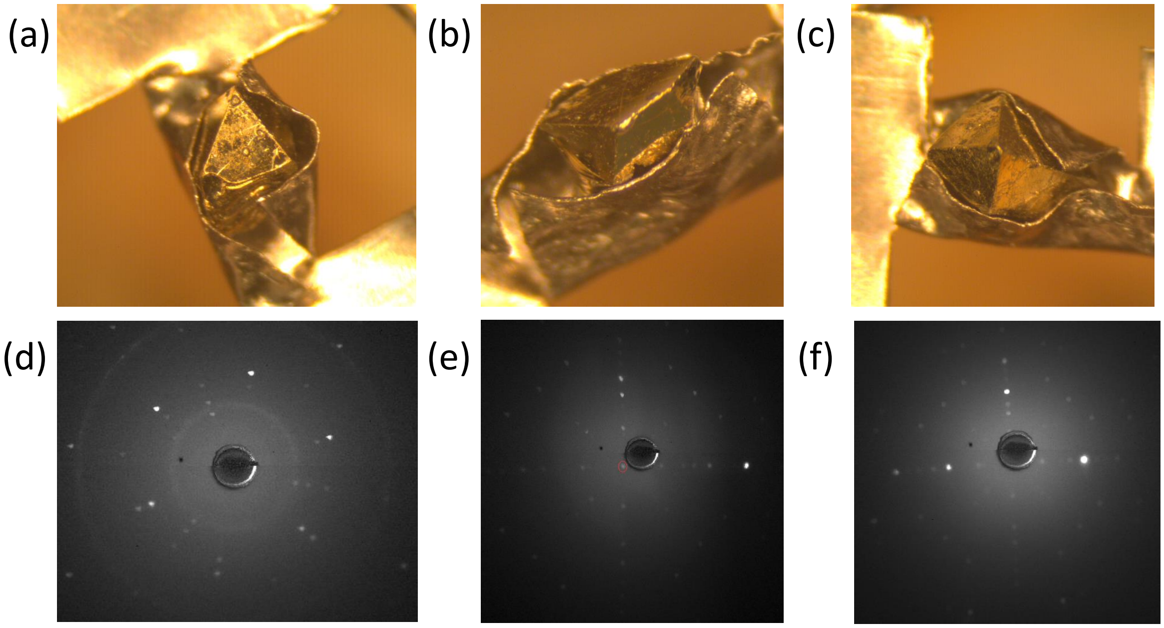

Figure 2.23 Laue pattern from Au_2Pb. (a)-(c) Au_2Pb natural growth facet, edge, and corner, respectively. (d)-(f) Laue pattern from (a)-(c) crystal orientations, respectively.

(more precisely six-fold) symmetry. Thus, the natural growth facet would be in (111) direction. Fig. 2.23(b) shows the natural growth edge, and panel (e) shows its Laue pattern with clear four-fold symmetry, indicating the (001) direction. Fig. 2.23 shows the natural growth corner, which shows a four-fold crystal symmetry at the tip. Obviously the Laue pattern shown in panel (f) has a clear four-fold symmetry, consistent with the crystal image. The orientations of the single crystals' edge and corner may vary from one to the other, but most of the facets that we have measured show clear six-fold symmetry, i.e., along (111) direction. With the ability to determine the single crystal orientation by Laue system, we successfully obtained crystals with (111) and (001) surfaces by cutting, filing, and polishing various pieces of the sample.

Taking the corner at the (001) orientation of the crystal as an example, we first use a diamond file to file the tip of the crystal off as shown in Fig. 2.24(a), then various grades of sandpapers are used to rough polish the top surface [Fig. 2.24(b)], finally we use grinder/polisher to fine polish the crystal surface as shown in Fig. 2.24(c). Fig. 2.24 shows this three-step process, with each step improving the flatness of the crystal surface. In panel (c), a flat and shiny surface is obtained after proper polishing, which almost resembles the surface of a layer-structured crystal surface after cleaving [Fig. 2.20(b)]. However, we should note that the sample surface is still not as perfectly flat as the surfaces in cleaved samples. Besides, even with careful handling of the crystal surface, there are still small scratches on the surface that cannot be eliminated completely. With all the polishing powders/solutions and glueing wax, it is very important to clean the crystal thoroughly before loading the crystal into ultrahigh vacuum in order not to contaminate the whole system.

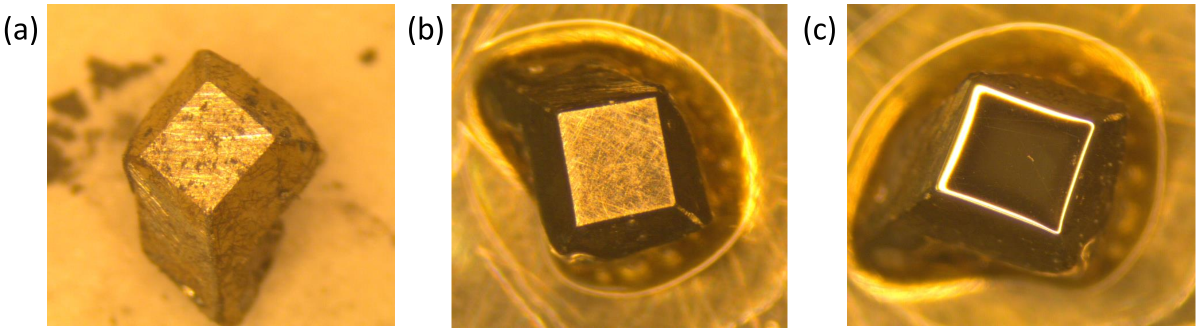

Figure 2.24 Process of polishing Au_2Pb. (a) After filing the tip of Au_2Pb crystal off. (b) After polishing with various grades of sandpapers. (c) After polishing with grinder/polisher.

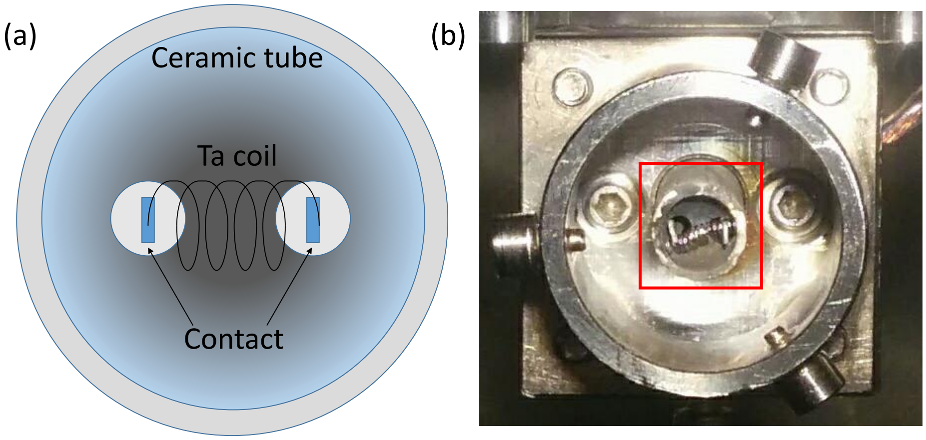

Figure 2.25 Stage for electron heating. (a) Schematic of the electron heating stage. (b) Picture of the sample stage. The red box marks the electron heating stage.

Sputtering is used to clean the top surface of the polished sample. During sputtering process, Argon gas with a base pressure of 1 × 10^{-5} Torr is maintained in the preparation chamber. At the beginning, sputtering voltage of 1 kV and current of 15 mA are used to clean the surface. However, this high sputtering voltage and current could potentially lead to significant damage to the crystal structure at the surface. Thus, annealing is required to obtain a smooth surface and reduce the number of defects. Fig. 2.25 shows the custom made electron beam heating stage, where high-energy (1 keV) electron beam emitted from Ta coil bombards the back of the sample holder and thus transfer kinetic energy to thermal energy for sample heating. Fig. 2.25(a) shows the schematic view of the electron heating stage, and panel (b) shows a picture of the whole sample stage with the red box marking the electron heating component. Typically temperatures below 500 °C can be easily achieved and samples are kept at temperatures below its melting point for several minutes or longer. This sputtering and annealing process will be repeated multiple times in order to obtain a nice smooth surface. During the cycling procedure, sputtering voltage can be lowered down to 200 V, which is enough to clean the sample surface without introducing major damage in the Au_2Pb case.

Fig. 2.26 shows the Fermi surface measurements of Au_2Pb measured at photon energy of 21.2 eV. As we have shown in Fig. 2.23, the natural growth facet of this crystal is in the (111) direction and the edge and corner cases are most often along the (001) direction. Thus, in order to obtain the Fermi surface of Au_2Pb along the (001) direction, we have to polish, sputter, and anneal the samples as described above. Fig. 2.26(a) shows the ARPES intensity integrated within 10 meV about the chemical potential measured along (001) direction. We can see several pockets in the first Brillouin zone, which seem to be consistent with four-fold symmetry. However, due to the fact that polishing, sputtering, and annealing cannot produce a perfect atomically flat surface, the band structures cannot be resolved clearly. Thus, we cannot determine whether this is exactly four-fold symmetry or it is two-fold symmetry as proposed in the literature that the Au_2Pb crystal undergoes a low temperature structural phase transition from cubic Laves phase into orthorhombic phase structure (slightly distorted version of the cubic Laves phase structure) [77]. On the other hand, the (111) direction of this crystal has the natural growth facet. After sputtering and annealing (polishing is not necessary) for several

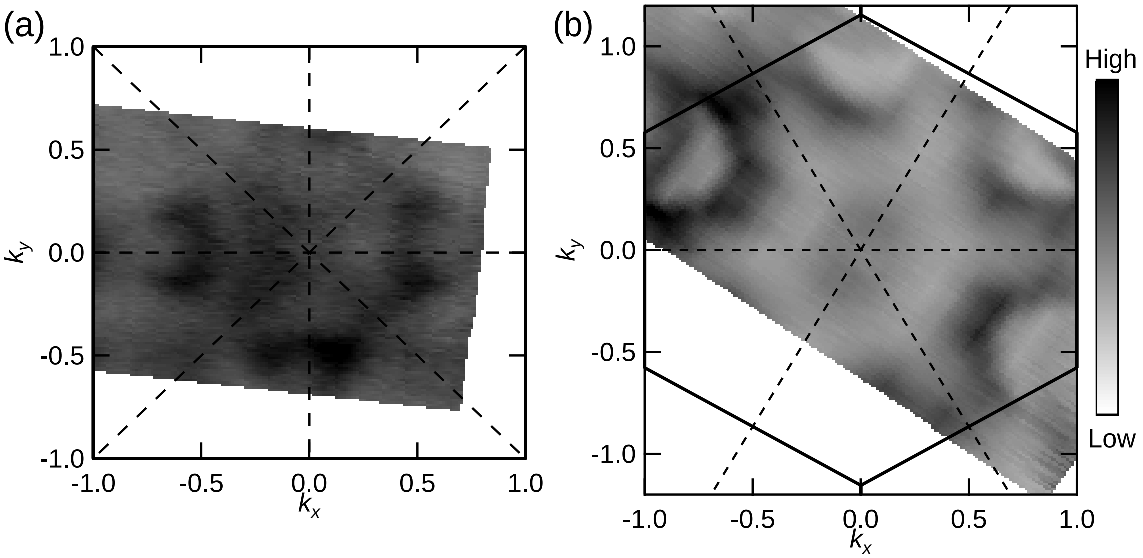

Figure 2.26 Fermi surface measurements of Au_2Pb. (a) Fermi surface plot of ARPES intensity integrated within 10 meV about the chemical potential measured along (001) direction and $T = 35$ K. (b) Fermi surface plot of ARPES intensity integrated within 10 meV about the chemical potential measured along (111) direction and $T = 18$ K.

cycles, we have obtained nice Fermi surface as shown in Fig. 2.26(b). From the ARPES intensity plot, we can see roughly six-fold symmetry in the Fermi surface, which is consistent with a cubic crystal structure. Thus, by measuring the electronic structure of Au_2Pb, we have demonstrate the advantages of using polishing, sputtering, and annealing technique in the ARPES experiments. It is an excellent technique to study the crystals that do not have a layered structure, i.e., those that cannot be cleaved properly. Furthermore, it has given us the power to study any orientations of the single crystal instead of being limited to its natural cleaving planes.

In summary, in this chapter, we have covered the basic knowledge of ARPES experiment. The basic principles of ARPES were discussed, such as the photoemission process including the momentum and energy conservation during the process, the one- and three-step model for calculating the ARPES intensity, one-particle spectral function for extracting the electron interaction/scattering information, and matrix elements that play an important role when we use left- and right-handed circularly polarized light. Then we have discussed the experimental components in a typical ARPES system, including different photon sources and their advantages and disadvantages, the electron analyzer and how it measures the energy and momentum of the photoelectrons at the same time, the ultrahigh vacuum and why it is important in ARPES measurements, and the cold head for precise temperature control of the samples. Finally we described two basic sample preparation techniques, i.e., cleaving and polishing/sputtering/annealing.

In the following chapters, we will utilized the ARPES system to study the electronic properties of some novel topological quantum materials, such as a topological insulator (semimetal) candidate LaBi with asymmetric mass acquisition, a three-dimensional Dirac semimetal Cd_3As_2 with detailed k_z dispersion, a type-II Weyl semimetal candidate WTe_2 harboring temperature-induced Lifshitz transition, and a Dirac node arc metal $PtSn_4$ with unusual Dirac node structure.

CHAPTER 3. TOPOLOGICAL SEMIMETAL CANDIDATE LaBi

3.1 Asymmetric mass acquisition in LaBi

The following context is an extended version of the published work in
Phys. Rev. B **94**, 081108(R)

3.1.1 Introduction

The discovery of quantum Hall effect [2] introduced the concept of quantum states that cannot be classified by spontaneous symmetry breaking, but instead are classified by their topology. Another topological state, quantum spin Hall state, has been theoretically predicted and experimentally observed in HgTe quantum wells [10, 12]. This new topological state exists in a system that is insulating in its bulk but topologically conducting on the edges (i.e., one-dimensional equivalent of a two-dimensional surface). A $Bi_{0.9}Sb_{0.1}$ binary was the first bulk material verified to be a topological insulator by use of angle-resolved photoemission spectroscopy (ARPES) to directly probe the electronic structure [11, 13]. However, its complicated surface states, fairly small bulk band gap, and alloying disorder made it hard to be a model system for studying topological quantum phenomena and technological applications. Bi_2Se_3, Bi_2Te_3, and Sb_2Te_3 were theoretically predicted [14] and experimentally proved to be the second generation topological insulators (or, at lease, near insulators) with a single Dirac cone residing at the Γ point [78, 16]. The surface Dirac cone states are protected by time-reversal symmetry (TRS). Therefore, TRS breaking sources, such as magnetic field or magnetic dopant can modify the massless electrons into finite mass electrons [22].

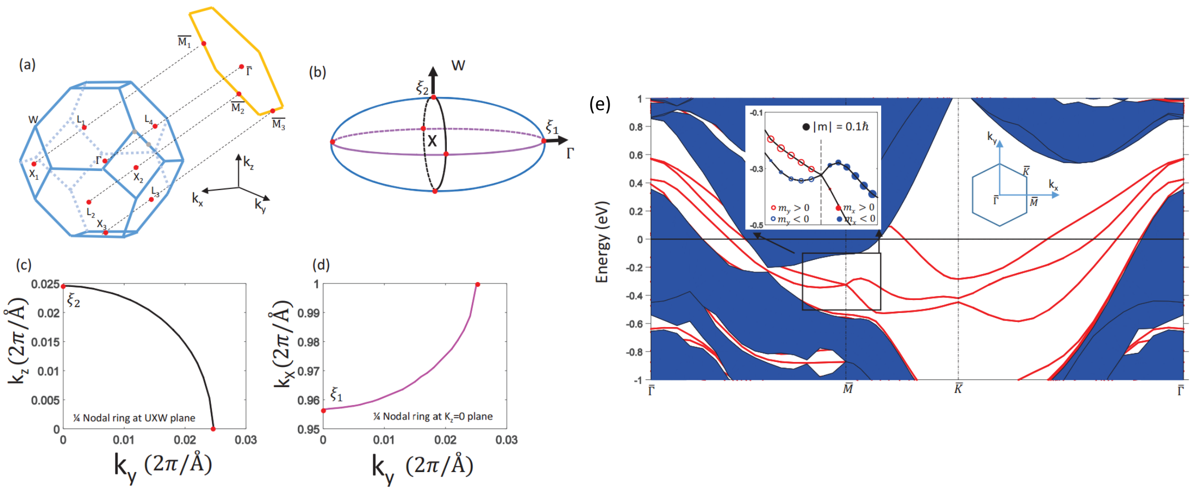

Figure 3.1 Brillouin zone and band structure calculations of LaBi. (a) The three-dimensional Brillouin zone of the face-centered cubic lattice and its projection to the surface Brillouin zone of the LaBi (111)-surface. (b) A schematic of the three nodal rings around one X-point in LaN. (c, d) The calculated configuration of the nodal rings on the yz-plane and the xy-plane, respectively. Only one quarter of each ring is shown due to symmetry. (e) The band structure on the (111)-surface of a 20-layer slab of LaBi. The inset shows the spin texture near M. (Adopted from Ref. [55])

The discovery of such topologically protected quantum states generated a lot of interest and sparked the search for other novel, exotic topological states, such as three-dimensional Dirac semimetals [27, 28, 26, 29, 30, 79], type-I and type-II Weyl semimetals [42, 43, 37, 41, 80, 44, 45, 46, 48, 47, 81, 82, 83, 84, 85, 86], and line node semimetals [53, 87]. However, no new family of binary topological insulators was reported to date. Recently, simple rocksalt rare-earth monopnictides LaX (X =N, P, As, Sb, Bi) were predicted to host novel topological states, such as "linked nodal ring" in LaN when spin-orbital coupling is neglected [55]. When considering the spin-orbital coupling, LaN turns into a three-dimensional Dirac semimetal and the rest of the family turn into topological insulators [55].

In Fig. 3.1 we present the drawing of the Brillouin zone and band structure calculations of LaBi. The three-dimensional (3D) Brillouin zone and its surface projection on the (111)-surface is shown in Fig. 3.1(a). When the spin-orbit coupling in LaBi is neglected, three nodal rings formed by band crossing points are predicted based on the first-principles calculations. These intersecting nodal rings look like the equator and two perpendicular longitudes of a football

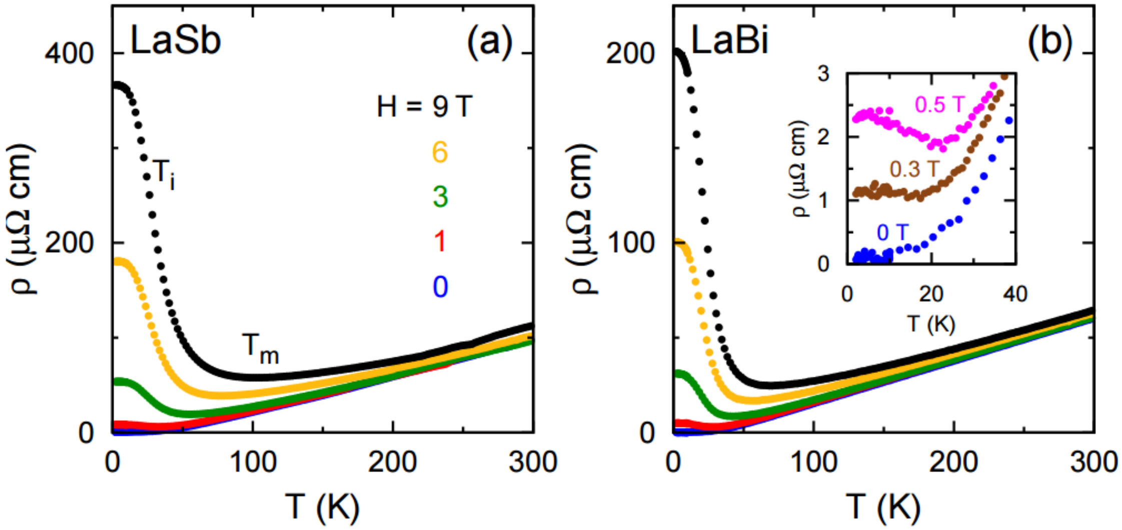

Figure 3.2 Extremely large magnetoresistance in LaSb and LaBi. (a) $\rho(T)$ of LaSb at several magnetic fields as indicated on the figure. Temperature of resistivity minimum T_m and inflection T_i are marked on the black curve. (b) $\rho(T)$ of LaBi at the same fields as in LaSb. Inset shows $\rho(T)$ at low T and low H to capture the onset of resistivity activation at 0.4 ± 0.1 T. (From Ref. [88])

centered at each X point as shown in Fig. 3.1(b). One quarter of each nodal ring is shown in Fig. 3.1(c) and (d) to provide more details. When spin-orbit coupling in LaBi is turned on (in calculation), the nodal rings break up and the band crossing along Γ-X becomes an anti-crossing with a gap of $\sim$ 35 meV, leading to a 3D topological insulator phase. Based on the analysis, the single Dirac cone projected onto the (001) surface would be buried inside the bulk projection continuum and hence cannot be observed. On the other hand, the projection on the (111)-surface will result in three Dirac cones at the M point as shown in Fig. 3.1(e). Since there are bands crossing the Fermi energy everywhere in the Brillouin zone, the LaBi is called a topological semimetal candidate in the published work instead of the topological insulator candidate as proposed in Ref. [55].

Interestingly, extremely large magnetoresistance was observed in this material [89, 90, 88]. As shown in Figs. 3.2(a) and (b), LaBi and its sister compound LaSb both show significant increase in the resistivity at low temperatures and high magnetic fields. The magnetoresistance, defined as $\mathrm{MR} = 100 \times [R(H) - R(0)]/R(0)$, can reach as high as $5 \times 10^5\%$ at the temperature of 2 K and magnetic field of 9 T [88]. The origin of the extremely large magnetoresistance in LaBi has been attributed to either its topological nature [88] or the electron-hole carrier compensation [90, 89, 91]. In order to elucidate this question, detailed band structure and Fermi surface measurements are needed.

Here, we present the results from our laboratory-based ARPES measurements and density functional theory (DFT) calculations detailing the electronic structure of LaBi. We observe the coexistence of the bulk and surface states at the Γ point from our He lamp and ultrahigh resolution laser-based ARPES measurements. The dispersion of the surface state is highly unusual. It resembles a Dirac cone, but upon closer inspection we can clearly detect an energy gap. The bottom band follows roughly a parabolic dispersion. The top band has an unusual linear "V"-shape dispersion with the tip approaching very closely to the extrapolated location of Dirac point. This is evidence of abnormal, asymmetric mass acquisition by Dirac fermions. Our data suggests that this compound hosts an unusual, yet to be understood topological state.

3.1.2 Methods

3.1.2.1 Sample growth.

Single crystals of LaBi were grown using a high-temperature solution growth technique [92]. Starting elements (La from Ames Laboratory and Bi from Alfa Aesar, 99.99% purity) were packed in a frit-disc alumina crucible set (otherwise known as a Canfield crucible set or CCS) [93] with a molar ratio of La : Bi = 30: 70. The crucible with the starting materials were sealed in a silica ampoule under a partial argon atmosphere. The whole ampoule was then heated up to 1200°C, held at 1200°C for 3 h and slowly cooled to 1000°C over 50–100 h, at which temperature the solution and the single crystals were quickly separated in a centrifuge. Single crystals of LaBi are cubic in shape with a typical edge length of 0.5 mm.

3.1.2.2 ARPES measurements.

ARPES measurements were carried out using a helium discharge lamp (angular and energy resolutions set at ∼0.3° and 15 meV, respectively) and tunable, laser-based [69] (∼0.05° and 1 meV) ARPES spectrometers. Data from the laser-based ARPES were collected with a tunable photon energy from 5.64 to 6.70 eV and the size of the photon beam on the sample was ~ 30 μm. Samples were cleaved *in situ* at a base pressure lower than 1×10^{-10} Torr. Samples were cleaved at 37 K in the He-lamp system and 40 K in the laser-based system and were kept at the cleaving temperature throughout the measurements. The cleaved surface is perpendicular to the (100) direction.

3.1.2.3 Calculation method.

DFT calculations [94, 95] have been done in VASP [96, 97] using the Perdew-Burke-Ernzerhof [98] exchange-correlation functional, plane-wave basis set with projected augmented waves [99] and spin-orbital coupling effect included. For bulk band structure of LaBi, we use the conventional tetragonal cell of four atoms along (001) direction with a $(10\times10\times8)$ k-point mesh. For (001) surface band structure, we sue slabs up to 48 atomic layers or 96 atoms with a $(10\times10\times1)$ k-point mesh and at least a 12 Å vacuum. The kinetic energy cutoff is 165 eV. The convergence with respect to k-point mesh was carefully checked, with total energy converged below 1meV/atom. We use experimental lattice parameters of $a = 6.5799$ Å with atoms fixed in their bulk positions.

3.1.3 Results and Discussion

The crystal structure, calculated 3D Fermi surface (FS) and band dispersion along key directions in the Brillouin zone (BZ) for LaBi are shown in Figs. 3.3(a) - 3.3(c). Panel (d) shows the ARPES intensity measured at the chemical potential using the He-I line (21.2 eV) at $T = 37$ K. The data was integrated within 10 meV to improve statistics. High intensity areas mark the contours of the FS sheets. The FS consists of one electron and two hole pockets at the Γ point and two elliptical electron pockets at the M point (black dashed lines are guide to

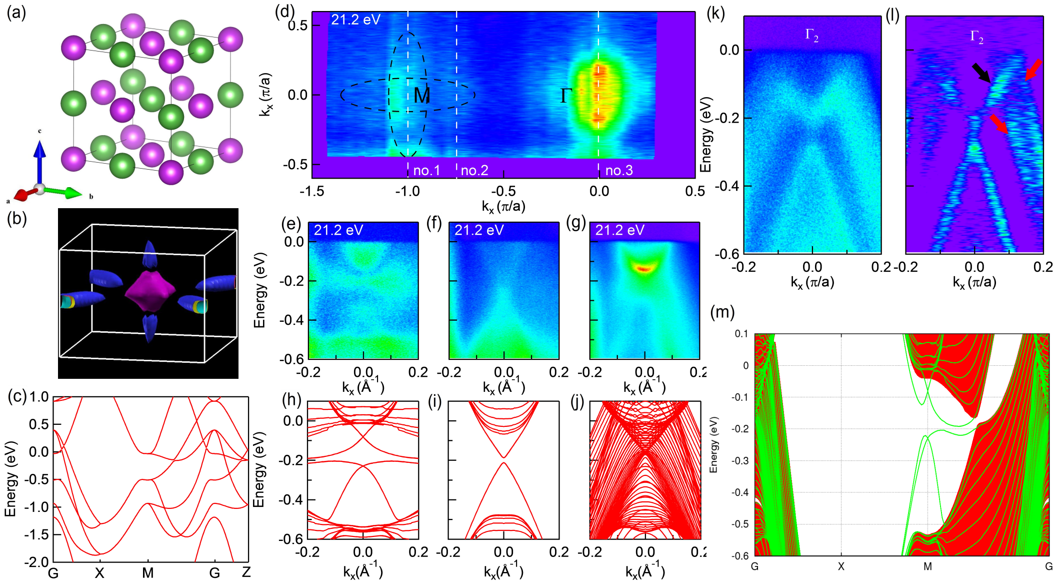

Figure 3.3 Calculated and experimental Fermi surface (FS) and band dispersion of LaBi measured at $T = 37$ K and photon energy of 21.2 eV. (a) Crystal structure (La: purple spheres; Bi: green spheres) of LaBi. (b) Brillouin zone (BZ) and DFT-calculated 3D bulk FS of LaBi. (c) Calculated bulk dispersion along main symmetry directions. (d) FS plot of ARPES intensity integrated within 10 meV of the chemical potential along $\Gamma - M$. (e)-(g) ARPES intensity along cuts 1–3 marked by white dashed lines in (b). (h)-(j) Surface-band dispersion calculated for a 48-layer slab along cuts 1–3 in (b). (k) Measured dispersion along the Γ cut in the second BZ. (l) Second derivative of data in (k). Black and red arrows point to electron and hole bands, respectively. (m) Projection of 3D bulk dispersion in red with overlapped green surface bands calculated for a 48-layer slab.

the eye). The FS resembles the calculated bulk-band FS from DFT as shown in Fig. 3.3(b). Panels (e)–(g) show the band dispersion measured using ARPES along cuts 1–3 [marked in (b) as white dashed lines] in Fig. 3.3(d). Panels (h)–(j) show the corresponding surface band calculations with a 48-layer slab along those same cuts shown in panels (e)–(g). In Panel (e), we can see two electron pockets at the M point with the smaller one being enclosed by the bigger one, which agrees with the calculations shown in panel (c). Panel (f) shows the band dispersion along the cut 2 at the crossing point of the $d - p$ orbital mixing. This feature may look like a Dirac cone, except that the calculation shows a possible gap separating the top and bottom bands. Our DFT calculation results are similar to the results in Ref. [55] in which

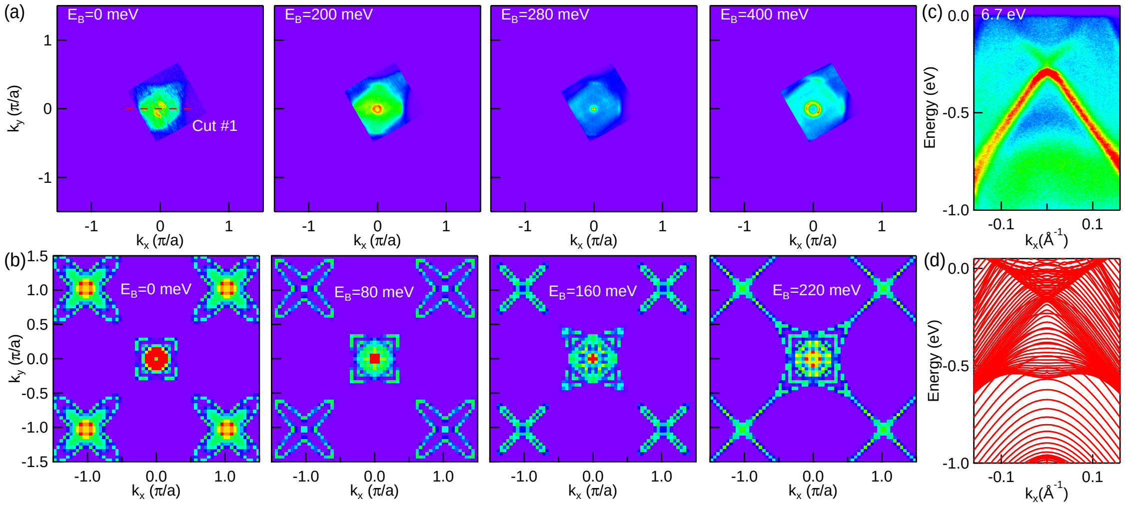

Figure 3.4 Fermi surface and band dispersion in the proximity of the Γ point measured at $T = 40$ K and photon energy of 6.70 eV. (a) Constant energy contour plots of ARPES intensity integrated within 10 meV at the binding energies of 0, 200, 280, and 400 meV. (b) Constant energy contour plots of DFT surface-band calculation at the binding energies of 0, 80, 160, and 220 meV with a 16-layer slab. (c) Band dispersion along cut 1 marked in panel (a). (d) Calculated surface-band dispersion along $\Gamma - X$ in panel (a) with a 48-layer slab.

topological surface state was predicted to reside in the $d - p$ band inversion regime. However, due to limited resolution and limited tunability of the photon energy in the He-lamp ARPES system, we cannot verify its surface origin by probing its out-of-plane momentum dispersion in proximity at the M point. At the Γ point [panel (g)], an electron pocket is clearly seen. However, no details can be resolved at higher binding energies. Panel (j) shows the calculated surface-band dispersion along the same cut as in panel (g), which very roughly resembles main features measured by ARPES results. The electron pocket and two hole pockets are clearly observed in the second BZ, as shown in Fig. 3.3(k) and its second derivative in panel (l). The band dispersion of the surface state at Γ is more complicated, because there is no gap in the projected 3D bulk dispersion, as shown in Fig. 3.3(m). This means that signals from both bulk and surface states will contribute to photoelectron intensity.

To reveal the details of these states at Γ we used a vacuum ultraviolet laser ARPES spectrometer. The low photon energy combined with small beam spot and ultrahigh resolution allows us to gain more information about these features. Figure 3.4 shows the constant energy contours and data along the high symmetry cut along with the results of the DFT surface-band calculations using a slab method. Panel (a) shows the constant energy contours measured at 40 K and photon energy of 6.7 eV. The constant energy contour at the Fermi level shows rather blurred features dominated mostly by bulk bands. At the binding energy of 200 meV, a circular energy contour can be clearly observed, surrounded by square shape bulk-band intensities. Further moving down to 280 meV below the Fermi level, the circle shrinks to a dot of intensity. At binding energy of 400 meV, the dot expands to an almost perfect circle. Panel (b) shows the constant energy contours from DFT calculations with a 16-layer slab, which also shows the evolution of the Dirac-cone like feature from a circular contour to a single Dirac point and further to a circular contour, which is not very easily resolved due to contribution of the bulk-band projection, but has an overall shape consistent with the data. The surface Dirac-cone like band dispersion can be better visualized in band dispersion data [panel (c)] along cut 1 in Fig. 3.4(a). The bulk conduction band crosses the Fermi level and the top of the bulk valence band is visible in panel (c). The conduction and valence bands appear to be connected by a surface state that forms a Dirac-like cone. Panel (d) shows the calculated surface state with a 48-layer slab, which demonstrates that the surface state is buried in the bulk state projection. This is consistent with the data shown in panel (a) and it is also consistent with previously reported results [55].

We utilize photon energy dependent ARPES data to distinguish between bulk and surface states as shown in Fig. 3.5. A single Dirac-like dispersion is present at higher photon energies [top row of data in panel (a)] with no obvious change in shape. However, the size of the conduction electron pocket and the intensity of the bulk hole band change drastically especially for lower photon energies and overshadow the surface state due to different matrix elements [bottom row of panel (a)]. In order to qualitatively determine the change in the size of the conduction electron pocket as a function of k_z momentum, we have plotted the momentum dispersion curves (MDCs) at the Fermi level in panel (b), which clearly shows an increase of the electron pocket size with decreasing incident photon energies. For the four highest photon energies we plot the MDCs at binding energies of 200 meV (top part of the Dirac-cone-like feature) and 320 meV (bottom part of the Dirac-cone-like feature). Constant separation

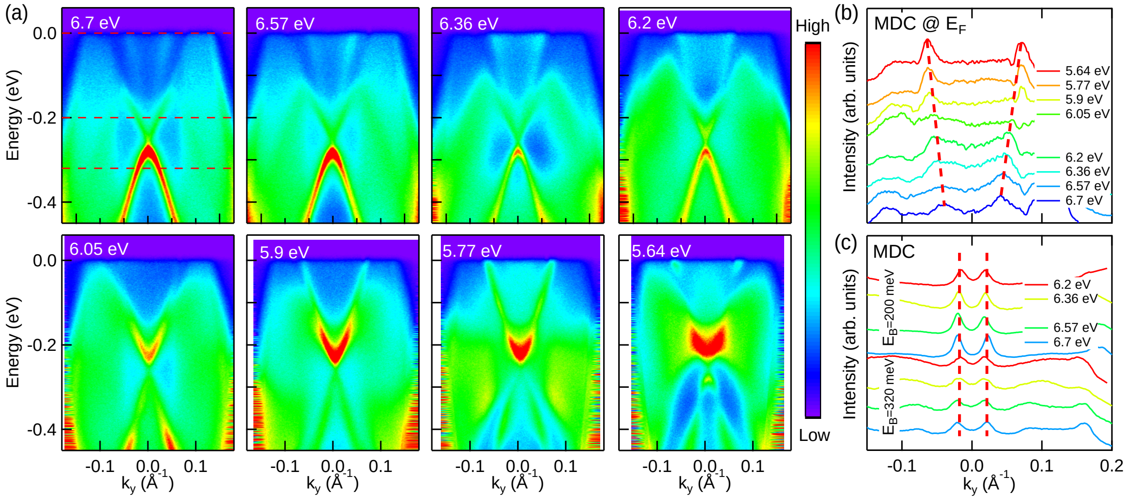

Figure 3.5 Band dispersion measured at $T = 30$ K using several photon energies. (a) Band dispersion along cut 1 in Fig. 3.4(a) using photon energies of 6.70, 6.57, 6.36, 6.20, 6.05, 5.90, and 5.64 eV. (b) Momentum dispersion curves at the chemical potential for data in panel (a). (c) Momentum dispersion curves at the binding energies of 200 and 320 meV for data in panel (a).

between the MDC peaks demonstrates surface origin or quasi-two-dimensionality of this feature. These results are consistent with the band structure calculations.

The key question raised by these data is whether or not this actually is a relativistic, Dirac dispersion with no energy gap and apparent degeneracy of electronic states at the Dirac point. To examine this we use energy distribution curves (EDCs) and look for the presence of an energy gap. The band dispersion along the Γ cut measured with 6.7 eV photons is shown in Fig. 3.6(a). In Fig. 3.6(b), we show the band dispersion extracted from MDC peaks (green lines) and EDC peaks (red lines). The lower band has a parabolic dispersion that can only occur if and energy gap is present. To verify this, we have plotted a set of EDCs equally spaced in the momentum in Fig. 3.6(c). The EDC at the suspected location of the Dirac point shows a peak that originates from the bottom part of the dispersion and a distinct shoulder at lower binding energy that originates from the upper band. The two peaks fitted to EDC at the Γ point are shown in Fig. 3.6(d). We also verified that at other photon energies, where the matrix elements weaken the intensity of the bottom band, a clear dip is observed in EDCs at the energy that would correspond to the Dirac point–evidence that a gap is present instead

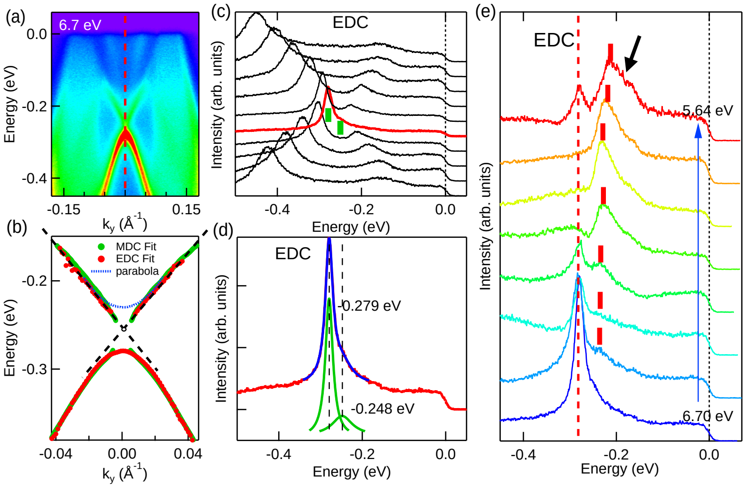

Figure 3.6 Band dispersion and EDCs measured at $T = 40$ K and photon energy of 6.7 eV. (a) Band dispersion measured along symmetry direction at Γ. (b) Band dispersion extracted by MDC (green) and ECD (red) fits. The black dashed lines are extensions of the top Dirac-like bands. The blue dotted line marks the dispersion of the bottom band reflected about the energy of the Dirac point–i.e., show the expected dispersion of the upper band for the case of symmetrical mass acquisition. (c) Set of equally spaced EDCs corresponding to the data in (a). The red curve is measured at Γ and it reveals the presence of an energy gap separating the upper and lower branches marked by bars. (d) Single EDC corresponding to the data in (c). The green curves are two Lorentzian curves fitted to the EDC and the blue curve is the composite of the two green curves. The blacked lines mark the location of the peak positions. (e) EDC curves at Γ for measured photon energies. The red bar marks the locations of the surface state peak. The black arrow marks the intensity due to bulk band that increases at lower photon energies.

[Fig. 3.6(e)]. Note that at very low photon energies the bulk intensity overlaps and moves the apparent location of the upper peak to even lower binding energies. This additional intensity is indicated by the black arrow in the top curve of panel (e). These data confirm the presence of an energy gap separating the two bands and it demonstrates that Dirac fermions acquire mass and energy gap.

This is not a case of a trivial band gap. While the electron part of the band is parabolic, the top part is remarkably linear with a pronounced cusp pointing towards the bottom band. Usually, when Dirac fermions acquire mass, the upper and lower bands should develop similar parabolic features with degree of symmetry about the energy of the Dirac point. The experimental data is very different, as the upper band remains linear and cuspy almost to the Dirac point energy. To better illustrate this we marked the expected dispersion of the upper band for the case of symmetric mass acquisition by blue dots in Fig. 3.6(b). Such asymmetric acquisition of mass was not predicted by theory, to the best of our knowledge, and further theoretical efforts are needed to explain this highly unusual behavior.

In summary, we studied the electronic properties of newly proposed topological semimetal LaBi. The dispersion of the surface state resembles a Dirac cone, but upon closer inspection we can detect an energy gap. The bottom band follows roughly a parabolic dispersion. The top band has an unusually linear, V-shape dispersion with the tip approaching very closely to the bottom band. Such abnormal, asymmetric mass acquisition by Dirac fermions suggests that this compound likely hosts an unusual, yet to be understood topological state.

3.1.4 Acknowledgements

We acknowledge very useful discussions with Yuan-Ming Lu. This work was supported by the U.S. Department of Energy, Office of Science, Basic Energy Sciences, Materials Science and Engineering Division. Ames Laboratory is operated for the U.S. Department of Energy by Iowa State University under Contract No. DE-AC02-07CH11358. L.H. was supported by CEM, and NSF MRSEC, under contract No. DMR-1420451.

CHAPTER 4. THREE-DIMENSIONAL DIRAC SEMIMETAL Cd_3As_2

4.1 Three-dimensional Dirac state in Cd_3As_2

4.1.1 Introduction

As we have already discussed in Section 1.3, three-dimensional Dirac semimetals can potentially be parent compounds for Weyl semimetals and topological insulators when time-reversal or space-inversion symmetry is broken [24]. Cd_3As_2 is a three-dimensional semimetal with valence and conduction bands touching at discrete points along the Γ-Z axis, where the Dirac points are protected by the $\mathcal{C}_4$ rotation symmetry. ARPES measurements have provided strong evidence for the existence of Dirac dispersion in two-dimensional momentum space [28, 29, 30, 31] as shown in Fig. 1.7. However, due to the limited photon energy tunability at the synchrotron radiation centers, only coarse k_z measurements with photon energy steps of 4 eV [29], 1 eV [30], and 2 eV [31] were presented.

Measurements utilizing a broad range of photon energies with energy steps of 1 eV (see Fig. 4.1) reveal the bottom and top dispersion of the Dirac cones along all three momentum directions with and without potassium doping. In these measurements, only bottom Dirac cones can be observed in the as-grown crystals. These dispersions can be fitted with only one set of velocity parameters: $V_x = 8.47$ eV Å, $V_y = 8.56$ eV Å, and $V_z = 2.16$ eV Å as shown in Figs. 4.1(a)–(c). In order to observe the top Dirac cone, potassium doping was deposited. The top Dirac cone dispersions along all three directions are shown in Figs. 4.1(g)–(i). Even though the Dirac dispersions along the k_x and k_y can be resolved clearly, the dispersion along the k_z direction is still not very sharp [30]. Relatively large photon energy steps and limited momentum and energy resolutions significantly limit the ability to measure the Dirac dispersion along the k_z direction still remain uncovered. Here, we report the evolution

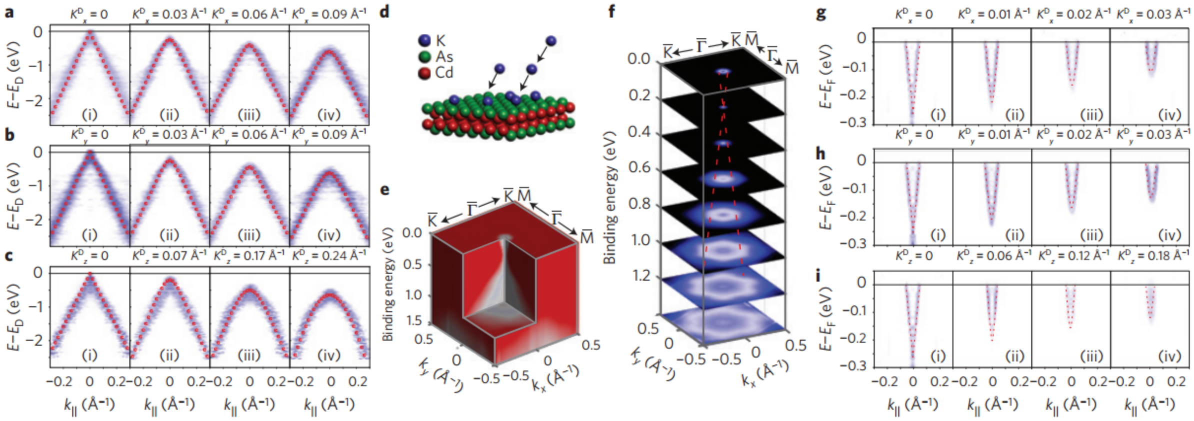

Figure 4.1 Dispersion of the three-dimensional Dirac fermions along all three momentum directions in Cd_3As_2. (a)–(c) Band dispersions measured at a series of k_x, k_y, and k_z values. Red dotted curves are fitted dispersions by using only one set of velocity parameters. (d) Illustration of the *in situ* electron doping using an alkaline metal dispenser. (e) Three-dimensional intensity plot of the photoemission spectra at the Dirac point after K surface doping, showing the upper Dirac cone. (f) Stacking plots of constant-energy contours after K doping. (g)–(i) Band dispersions of the upper Dirac cone measured after K doping with fitted dispersions. (From Ref. [30]).

of the Dirac dispersion along k_z direction by using tunable laser based ARPES with photon energy steps of ~ 0.15 eV. With the high precision control of the incident photon energy, and ultrahigh momentum and energy resolution, we can obtain high quality data showing the Dirac dispersion along all three momentum directions. Our ultrahigh resolution data helps us better determine the Fermi velocities of the electrons in this material.

4.1.2 Methods

4.1.2.1 Sample growth.

Crystals of Cd_3As_2 were grown by solution growth from a Cd-rich melt [79].

4.1.2.2 ARPES measurements.

Samples were cleaved *in situ* at 40 K under ultrahigh vacuum (better than 1.5×10^{-10} Torr), and kept at their cleaving temperature throughout the measurements. The data were acquired using a tunable VUV laser-based ARPES system, consisting of a Scienta R8000 electron analyzer. Photon energy dependent data were collected with a tunable photon energy from 5.77 eV to 6.7 eV with energy step of $\sim$ 0.15 eV. Momentum and energy resolutions were set at $\sim$ 0.005 Å^{-1} and 2 meV.

4.1.3 Results and Discussion

Fig. 4.2 shows the constant energy contours of Cd_3As_2 measured at various photon energies. Figs. 4.2(a)–(d) show the ARPES intensity of Cd_3As_2 integrated within 10 meV at the binding energy of 0, 100, 200, and 300 meV, respectively. We can clearly that the energy contour in

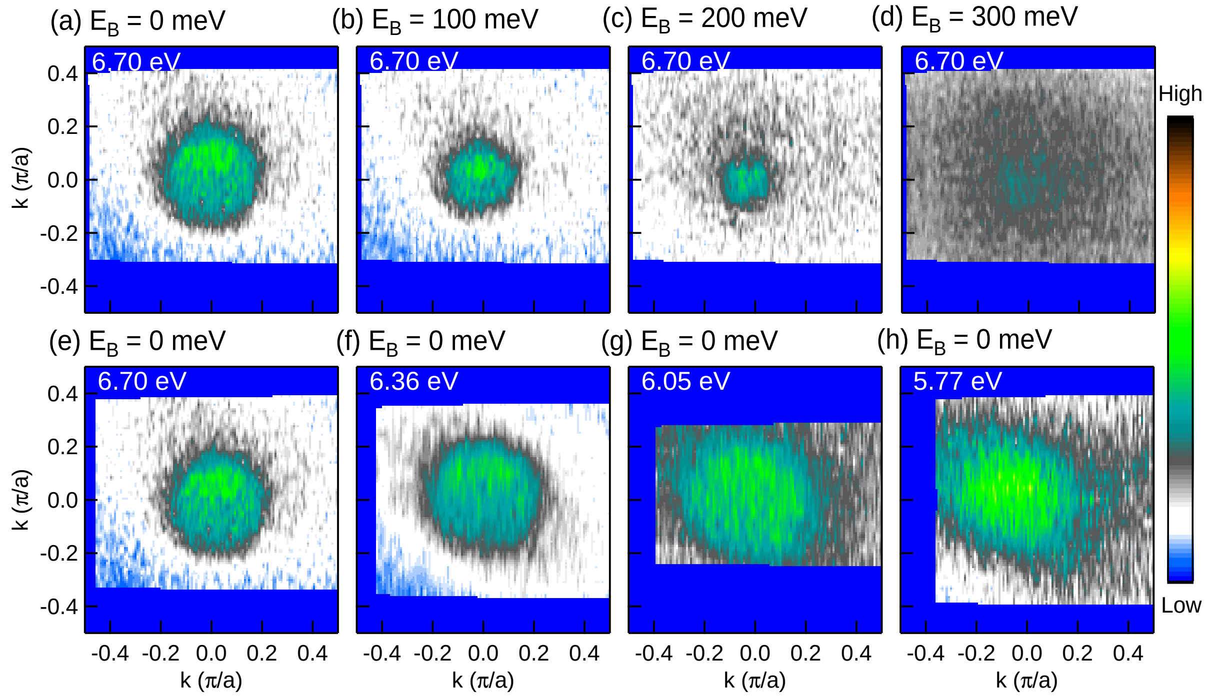

Figure 4.2 Constant energy contours of Cd_3As_2. (a)–(d) Constant energy contours of Cd_3As_2 measured at photon energy of 6.7 eV and binding energy of 0, 100, 200, and 300 meV, respectively. (e)–(h) Fermi surface plots (constant energy contours at E_F) of Cd_3As_2 measured using photon energy of 6.70, 6.36, 6.05, and 5.77 eV, respectively.

the k_x and k_y plane shrinks continuously with higher binding energy. These plots demonstrate that the top Dirac cone observed in the measurements. Figs. 4.2(e)–(h) show the Fermi surface of Cd_3As_2 measured at the photon energies of 6.70, 6.36, 6.05, and 5.77 eV, respectively. No clear trend can be concluded from the photon energy dependent Fermi surface measurements except for some variations in ARPES intensity and shape. On the other hand, the band dispersions at various photon energies provide essential information of the three-dimensional Dirac state in this material. In the following, we will show detailed photon energy dependence measurements of Cd_3As_2.

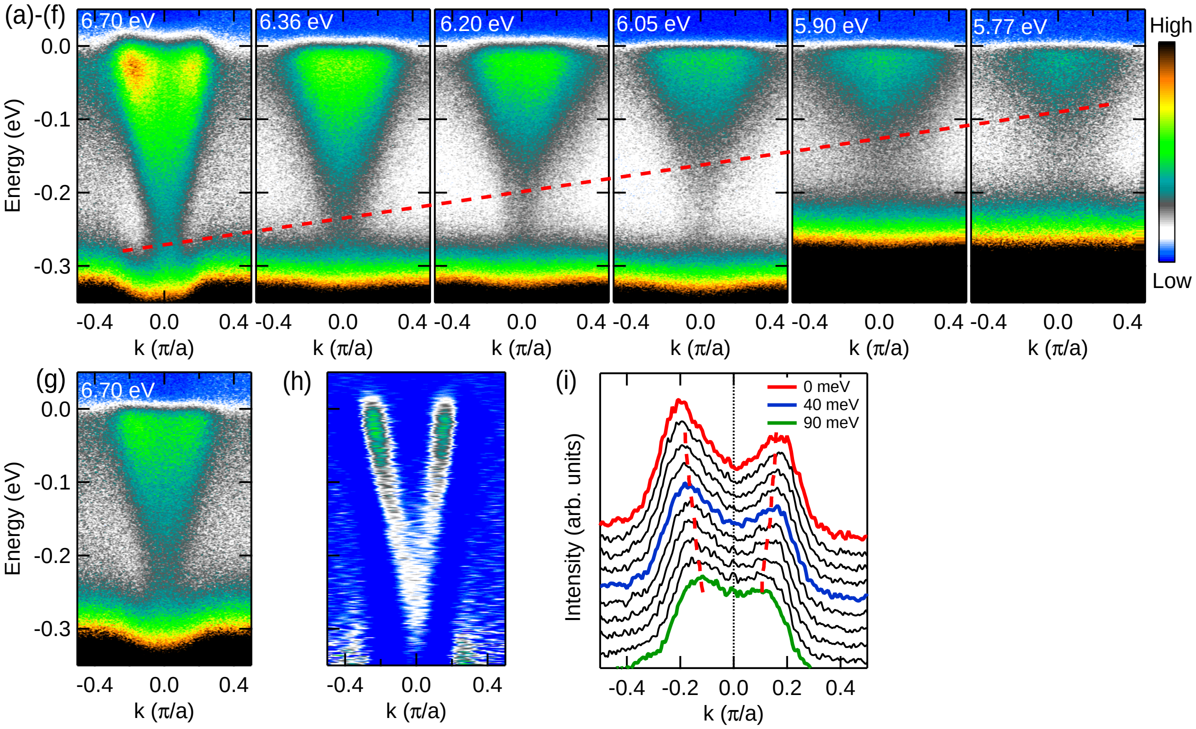

Figure 4.3 Band dispersions of Cd_3As_2 measured using various photon energies. (a)–(f) Band dispersions of Cd_3As_2 measured using photon energy of 6.70, 6.46, 6.20, 6.05, 5.90, and 5.77 eV, respectively. The red dashed line marks the bottom tip of the dispersions. (g) Band dispersion of Cd_3As_2 measured at photon energy of 6.70 eV. (h) Second derivative of (g). (i) Momentum dispersion curves (MDCs) of (h) with constant separations. The red dashed lines are peak positions of the MDCs fitted with double-Lorentzian function.

Fig. 4.3 demonstrates the three-dimensional Dirac state in Cd_3As_2 measured at the temperature of 40 K. Figs. 4.3(a)–(f) show the ARPES intensity measured at the photon energy of 6.70, 6.36, 6.20, 6.05, 5.90, and 5.77 eV, respectively. A Dirac dispersion is clearly seen with the bottom almost touching the top of the valence band in Fig. 4.3(a). As the incident photon energy decreases from 6.70 to 5.77 eV, the Dirac dispersion evolves from linear to parabolic, as the cut in momentum space moves away from the Dirac point and instead glides along side of the cone. Furthermore, the separation between the bottom of the Dirac dispersion and the top of the valence band also increases. The red dashed line in Figs. 4.3(a)–(f) connects the bottom tip of these dispersions from which velocity $v_z = 1.2$ eVÅ can be estimated, in agreement with the results in Ref. [30]. To estimate the Fermi velocity of the electrons in the k_x and k_y directions, we have plotted the second derivative [Fig. 4.3(h)] of the ARPES intensity measured using the photon energy of 6.70 eV [Fig. 4.3(g)]. In this plot, a nice linear dispersion is clearly visible with $V_x \approx V_y = 4.9$ eV Å. These results are consistent with the results from Ref. [30] of 5 eVÅ and are significantly smaller than the value from Ref. [29] of 10 eVÅ and Ref. [31] of 7.5 eVÅ. However, we should also note that due to the limited range of the photon energies in our laser system, we cannot probe the second Dirac point in the Brillouin zone along the Γ-Z direction as presented in other measurements performed using synchrotron radiation.

In conclusion, we verified the three-dimensional character of the Dirac state in Cd_3As_2 by using tunable laser ARPES with fine photon energy steps of ~ 0.15 eV. Our results show that the Fermi velocities along the k_x and k_y directions are roughly 4.9 eVÅ and along the k_z direction 1.2 eVÅ. Since the Dirac state in Cd_3As_2 is protected by crystal symmetry, it is a promising candidate for a parent compound of Weyl semimetals and topological insulators by inducing breaking of the time-reversal or space-inversion symmetry.

4.1.4 Acknowledgements

Funding agencies are the same as presented in Section 3.1.4.

CHAPTER 5. TYEP-II WEYL SEMIMETAL CANDIDATE WTe_2

WTe_2 has attracted great interest due to its extremely large magnetoresistance at low temperatures and high magnetic fields that do not show any sign of saturation [100]. This material was also proposed to be a type-II Weyl semimetal candidate, which has the Weyl nodes emerging at the contact points of the electron and hole pockets [44]. In this chapter, we will describe results of detailed measurements of the electronic structure of WTe_2: the temperature-induced Lifshitz transition in Section 5.1, the observation of Fermi arcs on the surface in Section 5.2, and its three-dimensional bulk electronic structure in Section 5.3.

5.1 Temperature-Induced Lifshitz Transition in WTe_2

The following context is an extended version of the published work in
Phys. Rev. Lett. **115**, 166602

5.1.1 Introduction

Traditional phase transitions are driven by spontaneous symmetry breaking and the continuous growth of an order parameter below the transition, as in magnets and superconductors. In addition, it is possible to have phase transitions in topological materials that do not break any symmetries but can be described by topological invariants. Here we describe a fundamentally different type of phase transition in fermionic systems, a Lifshitz transition. Such Lifshitz transitions hold the key to new types of topological phase transitions [101, 102]. Lifshitz transitions driven by chemical doping or substitution [103, 104] or pressure [105, 106] are common and have been observed previously.

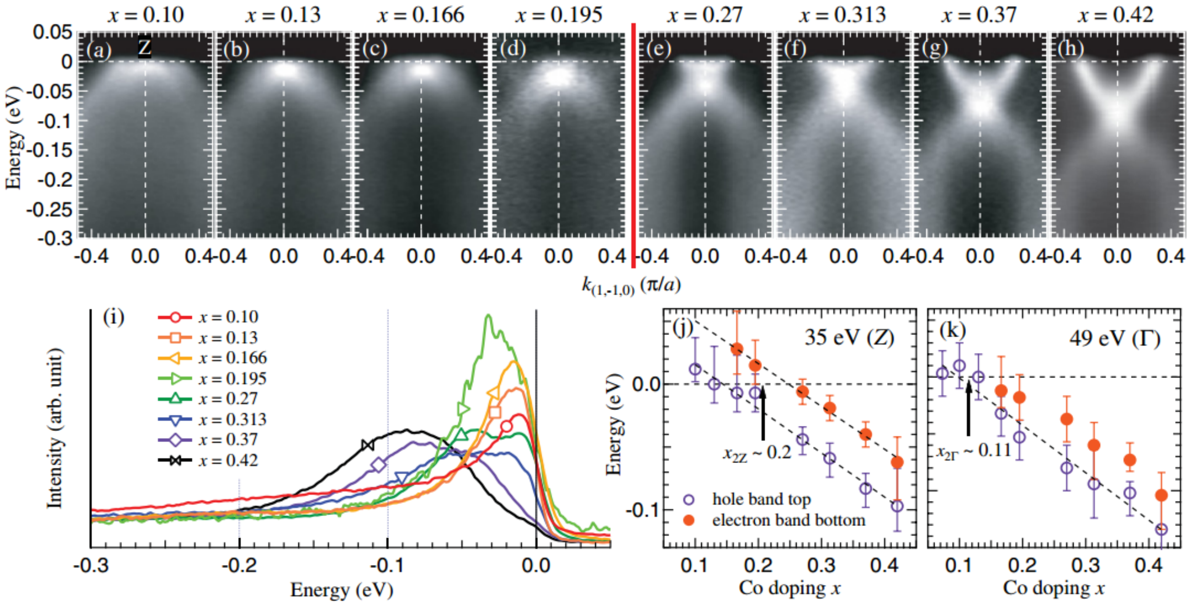

Figure 5.1 Band structure and Lifshitz transitions in $Ba(Fe_{1-x}Co_x)_2As_2$. (a)–(h) Band dispersion for eight different doping levels at T =20 K and photon energy of 35 eV. The red vertical line roughly marks the Lifshitz transition point. (i) Energy distribution curve at Z for each doping level. (j) and (k) Evolution of binding energy for the top of the hole band and the bottom of the electron band at the zone center with respect to cobalt doping. (From Ref. [104])

Fig. 5.1 shows the band dispersion analysis for the Lifshitz transitions in $Ba(Fe_{1-x}Co_x)_2As_2$. Figs. 5.1(a)–(h) show the band dispersion of $Ba(Fe_{1-x}Co_x)_2As_2$ measured at the temperature of 20 K and photon energy of 35 eV with eight different doping levels ranging from $x = 0.10$ to $x = 0.42$. As the cobalt doping level increases, the hole band at the Z point continuously moves down and the top of the hole touches the Fermi level at doping level of $x = 0.195$ as shown in Fig. 5.1(d). An electron band emerges as the doping level reaches $x = 0.27$ and keeps moving down to higher binding energies with increased doping. This dramatic change of Fermi surface topology from a hole pocket to an electron pocket at the critical doping level of $0.195 < x_c < 0.27$ demonstrates the doping-induced Lifshitz transition in $Ba(Fe_{1-x}Co_x)_2As_2$ [104]. In this section, we provide evidence for a new type of such transition in WTe_2 that is driven by temperature.

From the giant magnetoresistance (MR) in Fe/Cr superlattice [107, 108], to colossal MR in manganese oxide materials [109, 110, 111], these phenomena have opened a new era of applications in magnetic field sensors, read heads in high density hard disks, random access memories, and galvanic isolators [112]. Recently, extremely large MR has been obsrved in $PtSn_4$ [67], Cd_3As_2 [113], $NbSb_2$ [114], and WTe_2 [100]. In both $PtSn_4$ and WTe_2, the MR shows no sign of saturation and reaches an order of at least $10^5\%$ at low temperature. The MR in WTe_2 also displays large 3D anisotropy [115, 116] and is linear up to 60 T [115, 117]. Different mechanisms have been proposed to explain MR in these materials [67, 113, 100, 118, 119]. However, the exact origin of MR in these materials remains an open question.

WTe_2 has been known for several decades now [120], and a phenomenological three-carrier semimetal band model [120, 121], density-functional-based augmented spherical wave electronic structure calculations, and early, relatively low resolution ARPES [122] have supported the semimetallic nature of this material. Recent quantum oscillation [123, 124, 125] results have revealed the presence of four small electron and four small hole pockets of roughly similar size consistent with ARPES data [118]. These findings are consistent with carrier compensation mechanisms as the primary source of the MR effect [100, 119]. Furthermore, ARPES studies [118] also reported a change of the size of the Fermi pockets between 20 and 100K. More recently, Jiang *et al.* [126] have proposed that protection from backscattering could play a role in the large nonsaturating MR of WTe_2 in the presence of strong spin-orbital coupling effects. Amazingly, Kang *et al.* demonstrated that a suppression of the magnetoresistence with pressure in this material leads to emergence of superconductivity with respectable T_c of $\sim$6.5K [106]. This occurs in the absence of structural transition, and is caused by pressure-induced Lifshitz transition (suppression of hole pockets), as is evident from Hall data [106].

The strength of our Letter is the combination of temperature-dependent ultrahigh resolution, tunable vacuum ultraviolet (VUV) laser based ARPES [69], and temperature- and field-dependent resistivity and thermoelectric power (TEP) measurements, that together with electronic structure calculations provide new insights into the mechanisms driving the phenomena we observe. The electronic structure calculations show, and our data are consistent with, the presence of two pairs of hole pockets and two pairs of nearly degenerate electron pockets along the $X - \Gamma - X$ direction. Systematic temperature-dependence measurements reveal for the first time a Lifshitz transition, i.e., a change of the Fermi surface topology, close to 160 K, above which both pairs of hole pockets vanish. We further show that this transition is associated with a change of slope observed in the derivative of the temperature-dependent TEP. We demonstrate that the shift of the chemical potential (μ) with temperature, responsible for the Lifshitz transition, is caused by the close proximity of electron and hole densities of states near the Fermi energy. This result is applicable to other important semimetallic systems, such as pnictides, 3D Dirac semimetals, and Weyl semimetals.

5.1.2 Methods

5.1.2.1 Sample growth and transport measurements.

Whereas most of the previous measurements have been carried out on WTe_2 crystals grown via chemical vapor transport using halogens as transport agents [100, 127], we have grown WTe_2 single crystals from a Te-rich binary melt. High-purity, elemental W and Te were placed in alumina crucibles in W_1Te_{99} and W_2Te_{98} ratios. The crucibles were sealed in amorphous silica tubes and the ampoules were heated up to 1000 °C over 5 h, held at 1000 °C for 10 h, then slowly cooled to 460 °C over 100 h, and finally decanted using a centrifuge [92]. The resulting crystals were blade- or ribbonlike in morphology with typical dimensions of 3 × 0.5 × 0.01 mm with the crystallographic c axis being perpendicular to the larger crystal surface; the crystals are readily cleaved along this crystal surface. Temperature- and field-dependent transport measurements were performed in a Quantum Design Physical Property Measurement System for $1.8 \leq T \leq 350$ K and $|H| \leq 140$ kOe. The TEP measurements were performed by a dc alternating temperature gradient technique [128].

5.1.2.2 ARPES measurements.

Samples were cleaved *in situ* at 40 K in UHV. The data were acquired using a tunable VUV laser ARPES [69]. Momentum and energy resolution were set at $\sim$0.005 Å^{-1} and 2 meV.

5.1.2.3 Calculation method.

For first-principles band structure calculations, we used the Perdew-Burke-Ernzerhof parametrization of the generalized gradient approximation [98] and the full-potential (linearized) augmented plane-wave plus local orbitals [FP-(L)APW+LO] method including the spin-orbit coupling as implemented in the *WIEN2K* code [129]. Experimental crystal structure taken from Ref. [130] was used. The muffin-tin radii for W and Te atoms r_W and r_{Te}, were set to 2.4 and 2.38 a.u., respectively. The maximum modulus for the reciprocal lattice vectors K_{max} was chosen so that $r_{Te}K_{max} = 9.00$. TEP was calculated using a 52 × 29 × 13 k-point mesh with the *BOLTZTRAP* code [131].

5.1.3 Results and Discussion

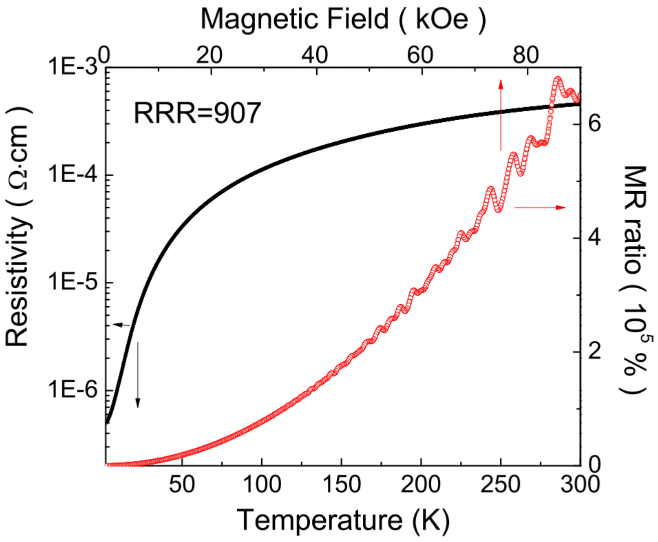

Figure 5.2 Temperature-dependent resistivity and field-dependent magnetoresistance measurements of WTe_2.

Temperature-dependent resistivity and field-dependent magnetoresistance.– Fig. 5.2 shows the resistance of the samples as a function of temperature and magnetic field measured in a standard, linear four probe configuration. The black curve is the resistivity data with residual resistivity ratio of ∼ 907, demonstrating excellent sample quality grown from Te-rich binary melt. The red curve presents the magnetoresistance ratio with respect to the applied magnetic

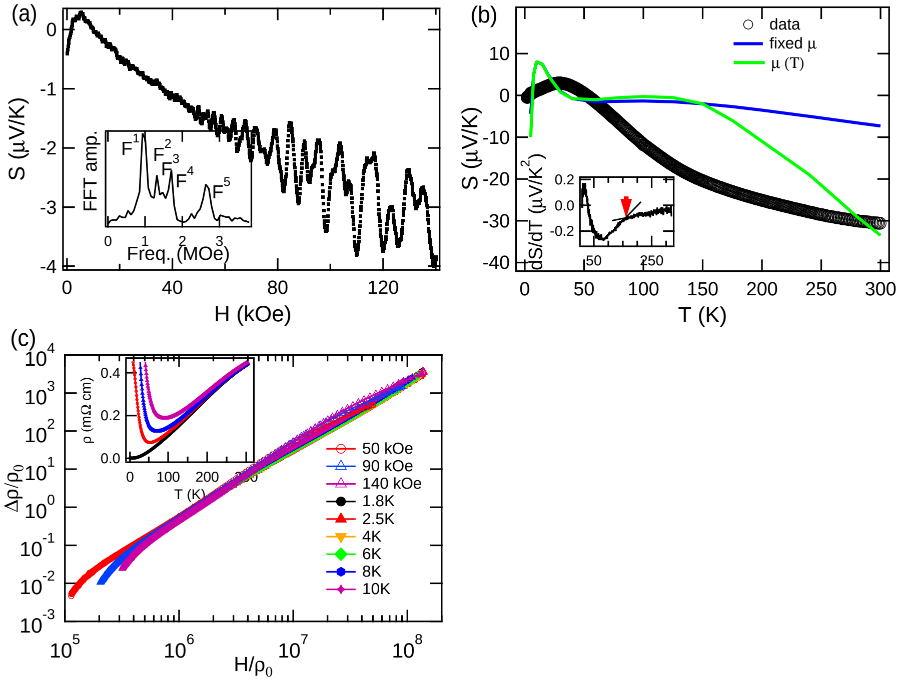

Figure 5.3 Transport property of WTe_2 (a) Magnetic field dependence of thermoelectric power (TEP) measured at T=2.2 K showing very clear quantum oscillations. Inset shows FFT of data after subtraction of a smooth background. (b) Temperature dependence of TEP. Inset shows first derivative with arrow marking the change of slope due to Lifshitz transition. Calculated x component of TEP (i) with fixed chemical potential $\mu(T = 0)$ (blue line) and (ii) with temperature-dependent $\mu(T)$ (green line). In case (ii), $\mu(T)$ calculated from the actual electronic structure is scaled by a factor of 3 for the best experimental fit and shows a variation of 45 meV for temperatures between 0 and 300 K. (c) Generalized Kohler plot. Arrow marks the point below which the Kohler rule is violated ($T < 60$ K). Inset shows temperature dependence of the resistance measured for magnetic field of 0, 50, 90, and 140 kOe.

field. The magnetoresistance reaches up to $6.5\times10^5\%$ at the temperature of 1.8 K and magnetic field of 90 kOe when field is applied along the c axis of the sample ($H \parallel c$). The magnetoresistance measured in our sample is in the same order as reported in the original literature [100].

Thermoelectric power.–The field dependence of the TEP at 2.2 K in WTe_2 shows very clear quantum oscillations [Fig. 5.3(a)], as was the case for $PtSn_4$ [67]. FFT analysis [Fig. 5.3(a) inset] gives $F^1 = 0.93$ MOe, $F^2 = 1.31$ MOe, $F^3 = 1.47$ MOe, and $F^4 = 1.70$ MOe, in excellent agreement with the values found from Shubnikov-de Hass data (Fig. S2 in Supplement Material). Peaks F^1 and F^4 are attributed to hole pockets, while peaks F^2 and F^3 are due to nearly degenerate electron pockets [123]. The peak labelled F^5 is though to be a result of the magnetic breakdown of F^1 and F^4 low field orbits [123].

The temperature dependence of the TEP in Fig. 5.3(b) shows two features that are noteworthy: (a) a monmonotonic dependence of the TEP on temperature with a local maximum at $\sim$30 K and (b) a kink at $T \sim 160$ K marked by an arrow in the inset of Fig. 5.3(b) observed in the rate of change of the TEP dS/dT as a function of temperature. This fact will be important when we investigate the electronic structure using ARPES. The solid greed and blue lines are calculated TEP and are discussed later. We also note that the here-reported feature in TEP occurs at very similar temperature to one where the large magnetoresistance is suppressed [100].

Temperature- and field-dependent magnetoresistance.–The temperature and field dependence of the extraordinarily large MR of WTe_2 are shown in Fig. 5.3(c). The generalized Kohler's plot shows that there is fairly good scaling of the data with an exponent of $\sim$1.98 at lower temperatures. As the temperature is increased, Kohler's scaling breaks down, as was also previously suggested [115], at the field indicated by the vertical arrow in Fig. 5.3(c); at this point temperatures range from 70 to 140 K for scans at different fields. We now proceed to elucidate the electronic origin of the change of the slope of The TEP and violation of Kohler's rule.

In The data discussed below, we provide evidence for two pairs of hole pockets and two pairs of electron pockets in ARPES. We then show the effect of increasing temperature, and how that enhances the electron pockets and finally the disappearance of the hole pockets, i.e., the Lifshitz transition observed at 160 K.

ARPES Fermi surface and band dispersion. –In Fig. 5.4(a) we show the ARPES intensity along high-symmetry directions in the Brillouin zone, integrated within 10 meV about the chemical potential, with the high intensity contours marking the location of the Fermi surface sheets. By comparing with our electronic structure calculations in Fig. 5.5(a), we observe that the ARPES data clearly resolved the two pairs of hole pockets; however, the separation

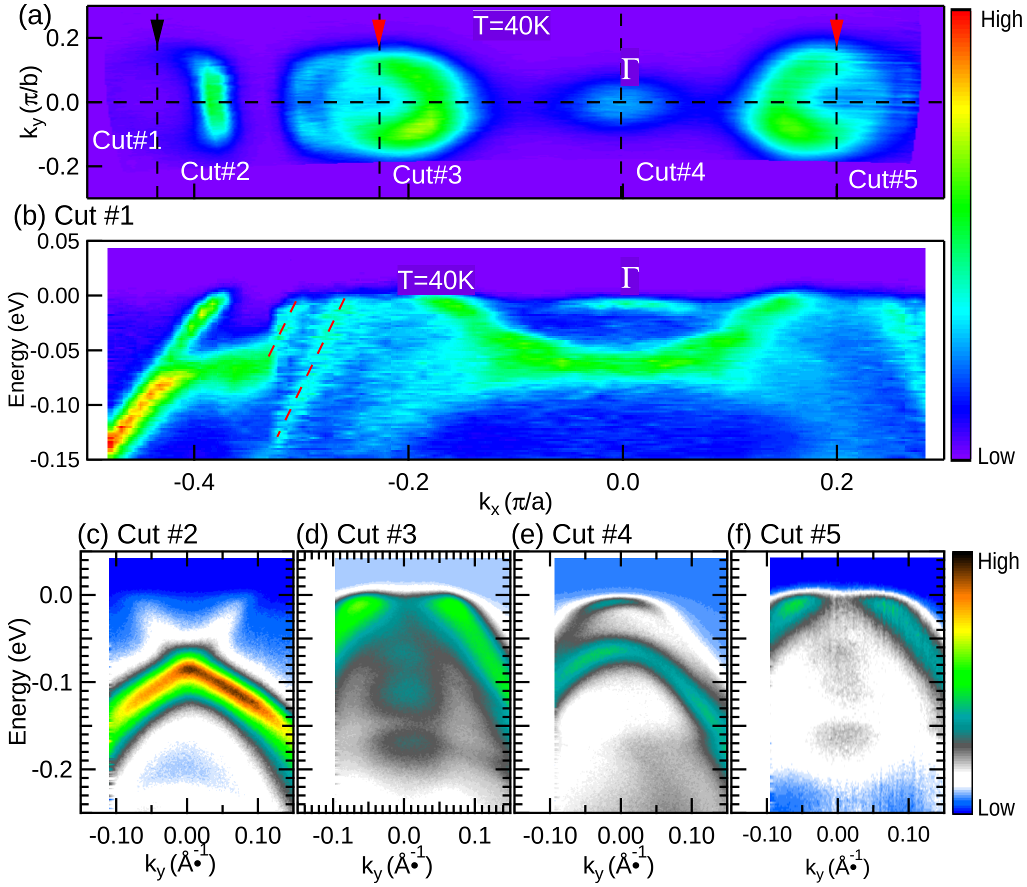

Figure 5.4 Fermi surface plot and band dispersion measured at $T = 40$ K and photon energy of 5.77 eV. (a) Fermi surface plot of ARPES intensity integrated within 10 meV about the chemical potential. Black and red arrows point to electron and hole pockets, respectively. (b)-(f) Band dispersion along cuts 1-5. Dashed lines in (b) mark the two left branches of the two hole bands.

between concentric electron pockets is too small and they appear as a single contour. The top of the band at Γ is located below the chemical potential for all studied photon energies and temperature down to 20 K, as shown in Fig. S6 of the Supplemental Material.

In the band dispersion in Fig. 5.4(b), only the right branch of the electron band is clearly visible due to matrix elements. This is followed by two crossings of the left sides of the hole bands (marked by dashed lines), and the coinciding crossings of the right branch of both of the hole bands. At the center of the BZ, the top of the hole band is located just below the chemical potential; thus, there is no hole pocket at the center of the zone. Detailed band dispersions along vertical cuts are shown in Figs. 5.4(c)-5.4(f). Figure 5.4(c) shows that the bottom of the electron band joins with the top of a lower band and appears just like the structure of a Dirac state [132] approximately 70 meV below the chemical potential. This is different from calculations shown in Fig. 5.5(a), where the bottom of the electron pocket is separated from the band below by a 200 meV gap. Cut 3 and cut 5 reveal that the dispersions of the hole pockets are nearly degenerate at this location.

*T-dependent ARPES and evidence for Lifshitz transition.–*We now proceed to describe one of the more intriguing electronic properties of this material, a restructuring of the Fermi surface with increasing temperature, that also has consequences for the unusual transport properties.

Fig. 5.5(a) shows the calculated band structure along the $\Gamma - X$ direction. The band calculation predicts a pair of hole pockets and a doubly degenerate electron pocket between Γ and X, in agreement with ARPES data presented above and with previous calculations [100]. In Figs. 5.5(b) and 5.5(c) we show the Fermi surface map measured at 40 and 160 K. The hole pockets (marked by red arrows) shrink from two circles to a spot of intensity and electron pockets (marked by black arrow) expand with increasing temperature. We detail this behavior by plotting ARPES intensity divided by the Fermi function along the vertical cut at the center of the hole pocket in Figs. 5.5(d)-5.5(k). A clearly visible hole band moves down in energy and by 160 K its top touches the chemical potential, and at a temperature of 280 K the top of this band has sunk below the chemical potential.

To quantify this effect we have plotted the Energy Distribution Curves (EDC) divided by the Fermi function at the center of the hole pocket for several temperatures in Fig. 5.5(l) and extracted the energy at the top of the hole band from a Gaussian fit in Fig. 5.5(m). Our data show that the top of the hole band moves down in energy upon increasing temperature from 18 meV at 120 K to -7 meV at 280 K. We have also extracted the area of the hole pocket by measuring the separation between Momentum Distribution Curves (MDC) peaks as a function of temperature in Fig. 5.5(m). We see that the top of the hole band moves below the chemical potential and the area of the hole pocket vanishes above ~160 K, signalling the Lifshitz transition.

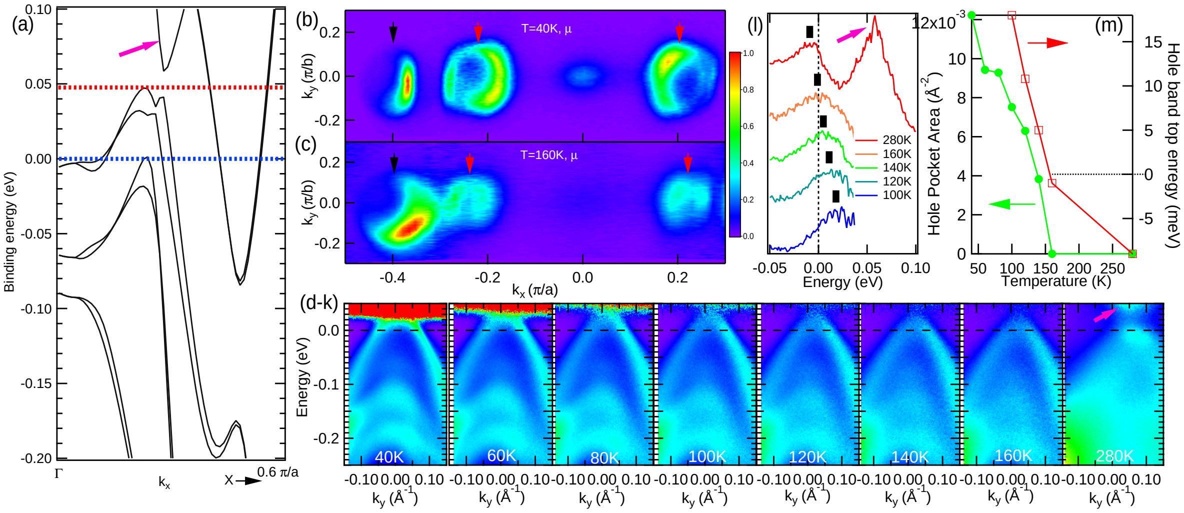

Figure 5.5 (a) Calculated band structure along $\Gamma - X$ symmetry direction. Blue and red dashed lines mark the values of chemical potential determined from ARPES data at low and high temperature, respectively. (b) Fermi surface plot of ARPES intensity integrated within 10 meV about the chemical potential measured at $T = 40$ K and 5.77 eV. Black and red arrows point to electron and hole pockets, respectively. (c) same as (b) but for $T = 160$ K. (d)-(k) Temperature dependence of the band dispersion at the hole pocket [along cut 1 in Fig. 1(a)] divided by the Fermi function. (l) EDCs divided by Fermi function at the center of the hole pocket for several temperatures. Black line marks the energy of the peak. (m) Temperature dependence of the area of the hole pocket and energy of the top of the hole band. Purple arrows in (a), (l), and (k) point to a band located above the hole band.

These data provide an archetypical example of a temperature-induced Lifshitz transition since they demonstrate a change of the Fermi surface topology upon heating. Chemical-substitution-induced Lifshitz transitions are quite common and were previously observed in $Ba(Fe_{1-x}Co_x)_2As_2$ at Co concentrations of 3.8 %, 11 %, and 20 % [103, 104]. On the other hand, a temperature-induced Lifshitz transition in the absence of a structure or magnetic phase transition is extremely rare. The temperature-dependent TEP, in particular the change of slope of $\partial S/\partial T$ at ∼160 K (Fig. 5.3, inset), is consistent with the existence of a temperature-induced Lifshitz transition, as TEP is expected to be very sensitive to the changes in the Fermi surface topology [133]. This conclusion can be further confirmed by the theoretical calculations as shown in the following.

*T dependence of chemical potential $\mu(T)$.–*The dramatic temperature-dependent change in relative size of the electron and hole pockets manifests itself in other measurements over wider temperature ranges, as we discuss below. Going back to Fig. 5.3(b), we compare the TEP measurements with our calculations of the x component of TEP. We notice that for a fixed $\mu(T) = 0$, the agreement is rather poor: the TEP has a large positive peak at low temperatures, and is almost temperature independent above ∼50 K [blue curve in Fig. 5.3(b)], quite unlike the behavior seen in the experimental TEP data.

We next calculate the temperature-dependent $\mu(T)$, by imposing a fixed total number of electrons across all bands at all temperatures. In conventional metals, μ does not change appreciably for $k_BT \ll E_F$. However, in WTe_2 and other semimetals, where the top of the hole band and bottom of the electron band are in close proximity (few tens of meV) to the chemical potential, significant changes of $\mu(T)$ with temperature can occur; e.g., in WTe_2 we calculate that chemical potential should shift by 14 meV between $T = 0$ K and $T = 300$ K. We have repeated the calculation of TEP using a scaled $\mu_F(T = 300\text{ K}) = 45$ meV to account for possible renormalization effects and match the experimentally observed shits. We then use such obtained $\mu_F(T)$ to calculate the x component of TEP. When the temperature-induced shifts of the chemical potential are taken into account, the absolute value of TEP increases monotonically at high temperatures with qualitatively improved agreement with the measurements [green line in Fig. 5.3(b)]. Although the calculation does not take into account the thermal expansion, phonon drag [134], and assumes constant relation time (i.e., ignores T-dependent scattering), it does reproduce the key features of the TEP data: the positive peak at low temperatures and the correct trend at higher temperatures. The breakdown of Kohler's rule in MR shown in Fig. 5.3(c) can also be understood in terms of the changing ratio of electron and hole carriers implied by the data in Fig. 5.5(m) and caused by the temperature-induced shift of $\mu(T)$.

In summary, we discovered the temperature-driven Lifshitz transition in highly magnetoresistive WTe_2. By correlating spectroscopic studies with electronic structure calculations, we find that the chemical potential can be strongly temperature dependent in semimetallic materials such as WTe_2, which in turn can strongly affect their magnetotransport properties [100] by driving a Lifshitz transition. Such shifts in μ with temperature were previously reported in pnictides' high-temperature superconductors [135, 136], where both electron and hole pockets were found in close proximity to the chemical potential. The mechanisms described here, the presence of small electron and hole pockets, strong chemical potential shifts, and Lifshitz transitions, are likely to be relevant for other systems, such as 3D Dirac semimetals, Weyl semimetals, and thermoelectric materials. In the presence of interactions, the restructured Fermi surfaces could change the nesting conditions and drive various magnetic, charge-ordered, and superconducting transitions in these classes of dichalcogenide and related materials.

5.1.4 Acknowledgements

We would like to thank Mohit Randeria for very useful discussions. Research was supported by the U.S. Department of Energy, Office of Basic Energy Sciences, Division of Materials Sciences and Engineering. Ames Laboratory is operated for the U.S. Department of Energy by the Iowa State University under Contract No. DE-AC02-07CH11358. N.H.J. is supported by the Gordon and Betty Moore Foundation EPiQS Initiative (Grant No. GBMF4411). Work at Ohio State University and L.H. were supported by CEM, a NSF MRSEC, under Grant No. DMR-1420451.

5.2 Observation of Fermi arcs in the type-II Weyl semimetal candidate WTe_2

The following context is an extended version of the published work in
Phys. Rev. B **94**, 121113(R)

5.2.1 Introduction

The discovery of graphene [132] opened the possibility to study relativistic quasiparticles that can be realized in solids. The occurrence of Dirac dispersion attracted great interest and triggered searches for novel topological states in three-dimensional (3D) systems [20, 137]. Dirac semimetals with bulk 3D Dirac points protected by crystal symmetry have been proposed to exist in β-cristobalite BiO_2 [24] and A_3Bi (A = Na, K, Rb) [27] and experimentally confirmed in Na_3Bi and Cd_3As_2 [26, 28, 29, 30, 31, 32, 79]. This led to the observation of novel topological quantum states with Fermi arcs [35, 50], which were first observed in Na_3Bi [138]. Subsequently, another type of massless particle–the Weyl fermion [139]–was predicted to exist in a family of noncentrosymmetric transition-metal monophosphides [42, 43]. Angle-resolved photoemission spectroscopy (ARPES) measurements on TaAs [37, 38, 39, 40] and NbAs [41] confirmed the existence of Fermi arcs connecting Weyl points of opposite chirality. Recently, a new type of Weyl semimetal (type-II Weyl semimetal) was proposed to possess Weyl points emerging at the boundary between electron and hole pockets [44]. WTe_2 [44] and $MoTe_2$ [45, 140] were among the first predicted to be type-II Weyl semimetals with different Fermi arc lengths. By doping Mo in WTe_2, the Fermi arc length (or the topological strength) can be continuously tuned [141]. Signatures of topological Fermi arcs have been reported in Mo-doped WTe_2 by using pump laser techniques to access the states above the Fermi level [142]. Spectroscopic evidence for type-II Weyl semimetal states in $MoTe_2$ was reported and novel "track states" were predicted by theoretical modelling and density functional theory calculations [143] and subsequently discovered by ARPES [47]. In addition to $W(Mo)Te_2$ family [142, 47, 144, 145, 146, 147], $YbMnBi_2$ [85] and LaAlGe [86] were also reported to display signatures of type-II Weyl semimetal states.

WTe_2 has attracted great interest due to its extremely large magnetoresistance at low temperatures and high magnetic fields [100], which resemble those of the earlier studied $PtSn_4$ [67, 148]. Superconductivity has been reported to emerge from a suppressed magnetoresistive state by applying high pressure [106, 149]. Interestingly, a temperature induced Lifshitz transition has also been observed in WTe_2 caused by dramatic shifts of the chemical potential with temperature [84]. Type-II Weyl semimetal states have also been proposed to exist in WTe_2 [44].

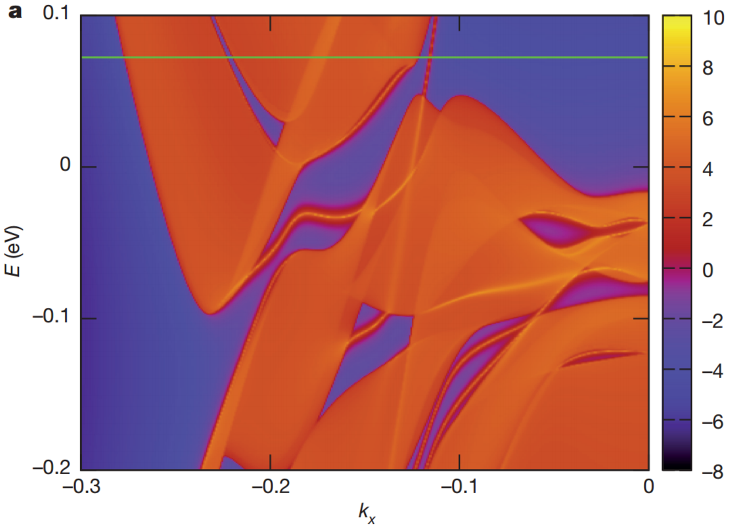

Figure 5.6 Topological surface state in WTe_2. (a) Spectral function of the (001) surface. The Fermi level (green line) is set to be between the Weyl points. (From Ref. [44])

Based on the band structure calculations, one of the four pairs of Weyl points resides at momentum points $k_1 = (0.1212, 0.0454, 0)$ and $k_2 = (0.1218, 0.0382, 0)$, which are very close to each other and hard to resolve by ARPES measurements. Both points are located slightly (0.058 eV and 0.052 eV, respectively) above the Fermi energy, making them difficult to observe by ARPES measurements. Fortunately, distinct topological surface states emerging from the projections of the Weyl points on the surface can be easily resolved by ARPES measurements. Due to the reflection symmetries in this material, Weyl points of opposite chirality are projected on top of each other on the (100) and (010) surfaces, which results in no topological surface states on these two surfaces. On the other hand, all the Weyl points project onto distinct points on (001) surface. Fig. 5.6 illustrates the spectral function of the (001) surface, where the Fermi level (green line) is set to be between the Weyl points. A Fermi arc emerging from the Weyl point at the hole pocket with non-zero Chern number connects to the Weyl point of opposite Chern number on the inside of the electron pocket. Surface states connecting electron and hole bands are clearly visible in Fig. 5.6 [44].

Although the band structures and Fermi surface of WTe_2 have been reported previously [118, 84, 150], no surface states were clearly observed in these studies. Here, we present the study of the electronic structure of WTe_2 by using an ultrahigh resolution, tunable, vacuum ultraviolet (vuv) laser-based ARPES system. We observed two pairs of Fermi arcs that link the electron and hole pockets. These features are consistent with the theoretical prediction that this material is a host of the type-II Weyl semimetallic state. Our results, together with reports of similar states in $MoTe_2$ [142, 47], point to the (W, Mo)Te_2 systems as exciting platforms for tuning the properties of Weyl fermions [141]. WTe_2, in particular, is a model system, where the topological properties can be turned on and off and tuned by the use of strain.

5.2.2 Methods

5.2.2.1 Sample growth.

Sample growth is the same as described in Section 5.1.2.1.

5.2.2.2 ARPES measurements.

Samples for ARPES measurements were cut to roughly a square shape (approximately 300×300 μm) and cleaved *in situ* at 16 and 40 K under ultrahigh vacuum (UHV). The data were acquired using a tunable vuv laser ARPES system, consisting of a Scienta R8000 electron analyzer, picosecond Ti:sapphire oscillator, and fourth harmonic generator [69]. Data were collected with tunable photon energies from 5.3 eV to 6.7 eV. Momentum and energy resolution were set at $\sim$0.005 Å^{-1} and 1 meV, respectively. The size of the photon beam on the sample was set at $\sim$ 30 μm.

5.2.3 Results and Discussion

The schematic drawing of the crystal structure of single unit cell layer of WTe_2 is shown in Fig. 5.7(a). This structure breaks the inversion symmetry due to slight differences in the bond lengths between tungsten and tellurium within the unit cell. This results in the tellurium layer on each side of tungsten being inequivalent. We label those as "A" and "B". We indeed observed two distinct types of electronic structures, but even for a single cleave there were often two different domain types present. This is illustrated in panels (b)–(e) where we show the picture of the sample after cleaving and data along cut #4 (marked in panel h, between the hole and electron pockets) for three spots are plotted in panels (c)–(e). The data from the part of the sample marked by a red circle in (b) shows sharp electron like dispersion near the E_F. The data near the edge of the sample [green and blue circles in (b)] partially (d) or completely (e) lacks this feature. The two domains have different Fermi surfaces and band dispersions as demonstrated in Fig. 5.7. The Fermi surface of type N (normal) domain is shown in panel (f) and band dispersion along the $\Gamma - X$ symmetry direction is plotted in panel (g). These data are very similar to what was previously reported [84]. Figure 5.7(h) shows the Fermi surface plot for the type T (topological) domains in the first Brillouin zone, integrated within 10 meV about the chemical potential, with the high intensity contours marking the location of the Fermi surface crossings. The presence of Fermi arcs that connect the bulk hole and electron pockets is clearly visible. This is further confirmed by examining the band dispersions along cuts #1-#6 as shown in Figs. 5.7(i)–5.7(n). In addition to the two nearly degenerate electron bands and two branches on the left side of the hole pockets (marked by the red dashed lines), a high intensity, sharp band dispersion can be clearly seen, that connects the bottom of the electron pockets and the top of the hole pockets. The data along the y-axis cuts shown in Figs. 5.7(i)–5.7(n), for the type T domains look almost the same as the type N domains [84], except for cuts #3 and #4. Here, an additional electron band s present that results in the formation of the Fermi arcs seen in Fig. 5.7(h). We will examine this feature in more detail below.

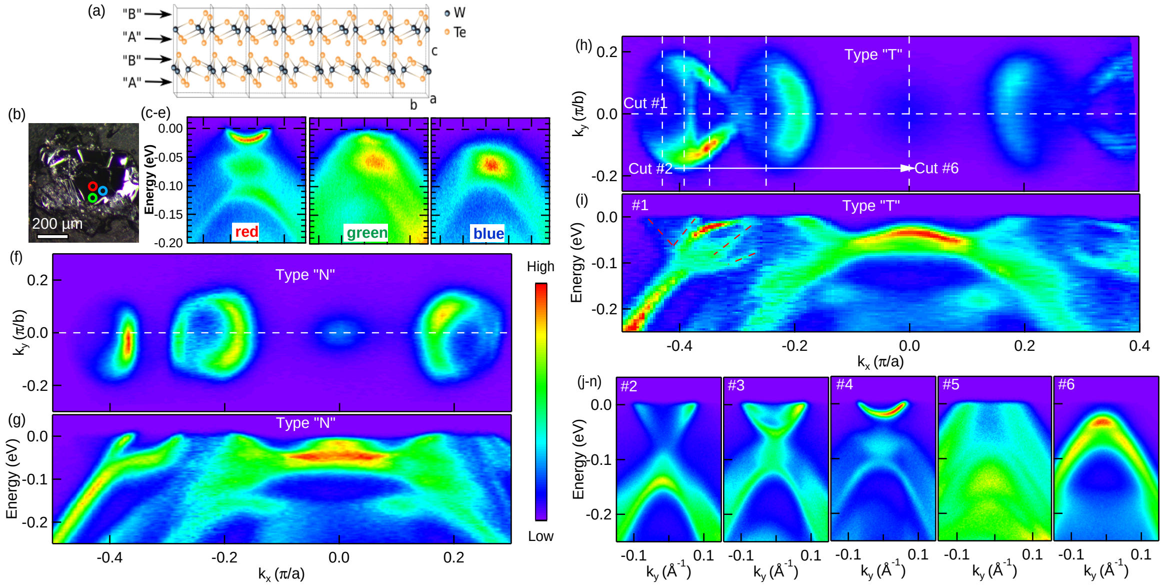

Figure 5.7 Two types of Fermi surface plot and band dispersion measured at photon energy of 6.7 eV. (a) Schematic drawing of the crystal structure of single unit cell layer with two possible cleaving sites marked by arrows. Note that these are not equivalent to “N” and “T” data types. (b) Optical image of the cleaved sample with three measured regions marked by circles. (c)–(e) Data measured in red, green, and blue regions marked in (b), respectively. (f) Type “N” Fermi surface plot of ARPES intensity integrated within 10 meV about the chemical potential measured at $T =$ 40 K. (g) Band dispersion along white dashed line cut in (f). (h) Type “T” Fermi surface plot of ARPES intensity integrated within 10 meV about the chemical potential measured at $T = 16$ K. (i)–(n) Band dispersions along cuts #1–#6 in (h). Red dashed lines in (i) mark the electron pocket and two left branches of the hole pockets.

The data from more than a dozen samples had both features present on cleaved surfaces. We also cleaved and measured the same piece of single crystal on both sides. We found the presence of both domains on each side. The presence of two types of domains on the same side of the sample is inconsistent with the scenario of two different surface terminations, as for a given piece of sample, cleaving it on one side should consistently yield either type “A” or “B”, but not both [see Fig. 5.7(a)]. Residual strain introduced by cutting and/or cleaving of the samples is responsible for the two different electronic structures. This is consistent with the theoretical prediction that the topological character of WTe_2 is highly sensitive to pressure and strain [44]. In particular, it was theoretically demonstrated that stretching the crystal along the a and c axis causes annihilation of the Weyl points and transition from topological to trivial semimetal. In type N (normal) domains the Fermi surface consists of two pairs of electron pockets and two pairs of hole pockets in agreement with previous studies [84, 118, 150] and bulk band calculations, where the Fermi arcs are absent. Those results are in contrast to the results from type T (topological) domains.

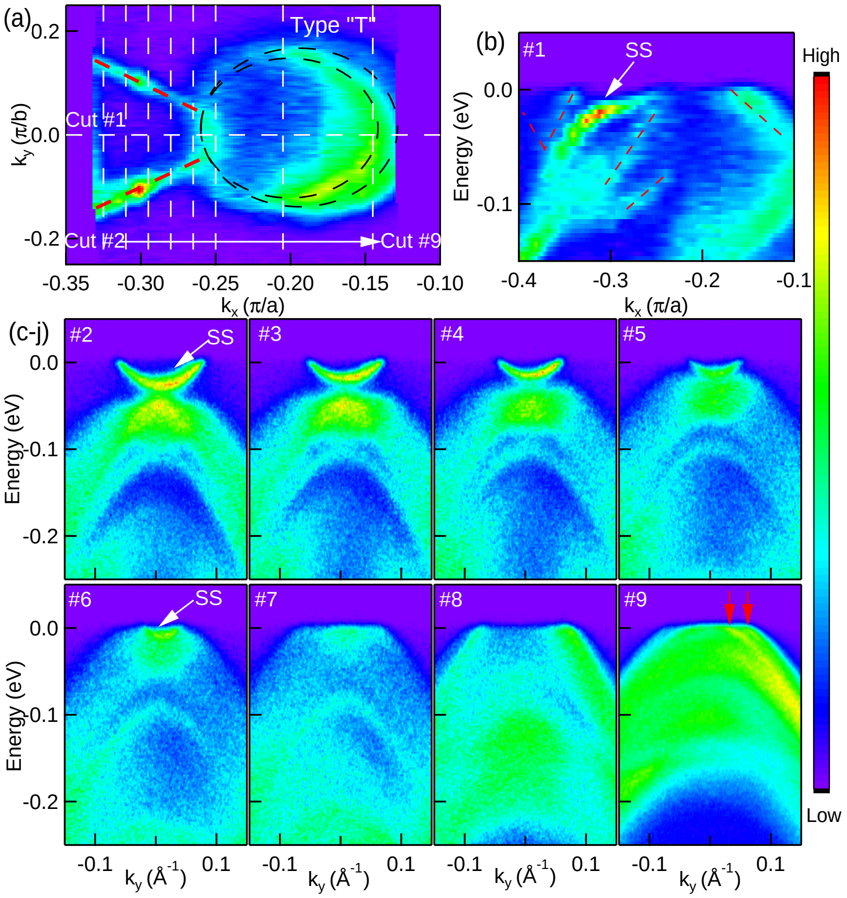

Figure 5.8 Fermi surface plot and band dispersion measured at $T = 16$ K and photon energy of 6.7 eV. (a) Fermi surface plot of ARPES intensity integrated within 5 meV about the chemical potential. The red dashed line marks the contour of the surface state (SS) and the black dashed lines mark the contour of the two bulk hole pockets. (b)–(j) Band dispersion along cuts #1–#9. Dashed lines in (b) mark the electron pocket and the two hole pockets. The white arrows point to the location of the SS. The red arrows in (j) point to the locations of the two hole bands crossing Fermi level.

Figure 5.8 shows details of the Fermi sheets and band dispersion of what we will show is an unusual surface state. In panel (a) we plot the ARPES intensity (integrated within 5 meV about the chemical potential) close to the momentum region, where the surface state connects to the hole pocket. The red dashed line and the black dashed lines in Fig. 5.8(a) mark the outline of the surface electron pockets and two almost degenerate hole pockets, respectively. The band dispersion along cut#1 is shown in Fig. 5.8(b), where the white arrow points to the location of the surface state. Detailed band dispersions along the white vertical cuts are shown in Figs. 5.8(c)–5.8(j). The bottom of this surface band dips only slightly below the E_F demonstrating its electron character. This band is much sharper than the lower energy broad, bulk hole bands, consistent with its surface origin. As we move towards the zone center, the electron band shrinks and moves closer to the Fermi level, while the lower hole bands move up. The Fermi arc surface state touches the hole bands at cut#5 [panel (f)] and is completely swallowed by the lower hole bands along cut#6 [panel (g)]. After cut#6, the hole bands continue moving up and finally cross the Fermi level and form a pair of hole pockets. We can clearly see the separation of the almost degenerate hole pockets along cut#9 [panel (j)], as marked by the red arrows pointing at the crossing points.

The merging between Fermi arcs and bulk electron pockets is shown in Fig. 5.9. Panel (a) shows the ARPES intensity integrated within 10 meV about the chemical potential and measured at $T = 160$ K. The black dashed line and red dashed line mark the location of the bulk electron pockets and Fermi arc band, respectively. In order to better show the details of the bulk electron pockets, we have plotted the ARPES intensity divided by the Fermi function along the white vertical cuts#1–#8 in Figs. 5.9(b)–5.9(i). At cut#1 [panel (b)], a single electron pocket is clearly observed that touches the top of the lower hole bands and forms the beginning of two Fermi arcs on either side. As we move away from the hole pockets, the band responsible for Fermi arcs moves to higher binding energy. Slightly further (cut#2) a bulk band becomes visible still above the E_F. Both bands are very clearly visible starting from cut #3, where they are indicated by white arrows and labelled. Closer to the center of the bulk electron pocket, the two bands eventually merge together. The detailed band evolution in Figs. 5.8 and 5.9 demonstrates that the Fermi arc states connect the bottom of the electron pockets

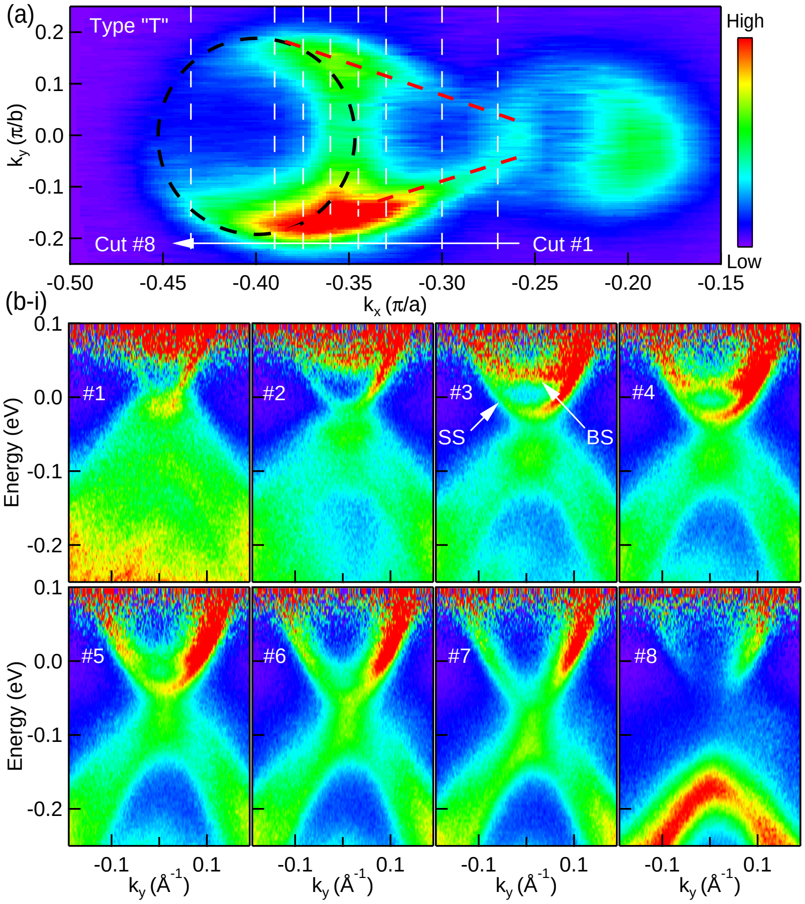

Figure 5.9 Fermi surface plot and band dispersion measured at $T = 160$ K and photon energy of 6.7 eV. (a) Fermi surface plot of ARPES intensity integrated within 10 meV about the chemical potential. The red dashed line marks the contour of the SS and black dashed line marks the contour of the bulk electron pocket. (b)–(i) Band dispersion along cuts #1–#8. The white arrows point to the location of the SS and the bulk state (BS).

and the top of the hole pockets, consistent with the previous theoretical prediction [44].

To verify the surface origin of the Fermi arc bands, we have carried out photon energy dependent measurements and present them in Fig. 5.10. Panels (a)–(c) show the ARPES intensity integrated within 10 meV about the chemical potential measured at photon energies of 6.7, 6.36, and 6.05 eV, respectively. We can clearly see that the shape of the bulk electron pockets and hole pockets change slightly with photon energy, but the Fermi arcs that connect them remain sharp and its central part does not. To better quantify our results, We have plotted the contour obtained by fitting to the data of the Fermi arc band in Fig. 5.10(d).

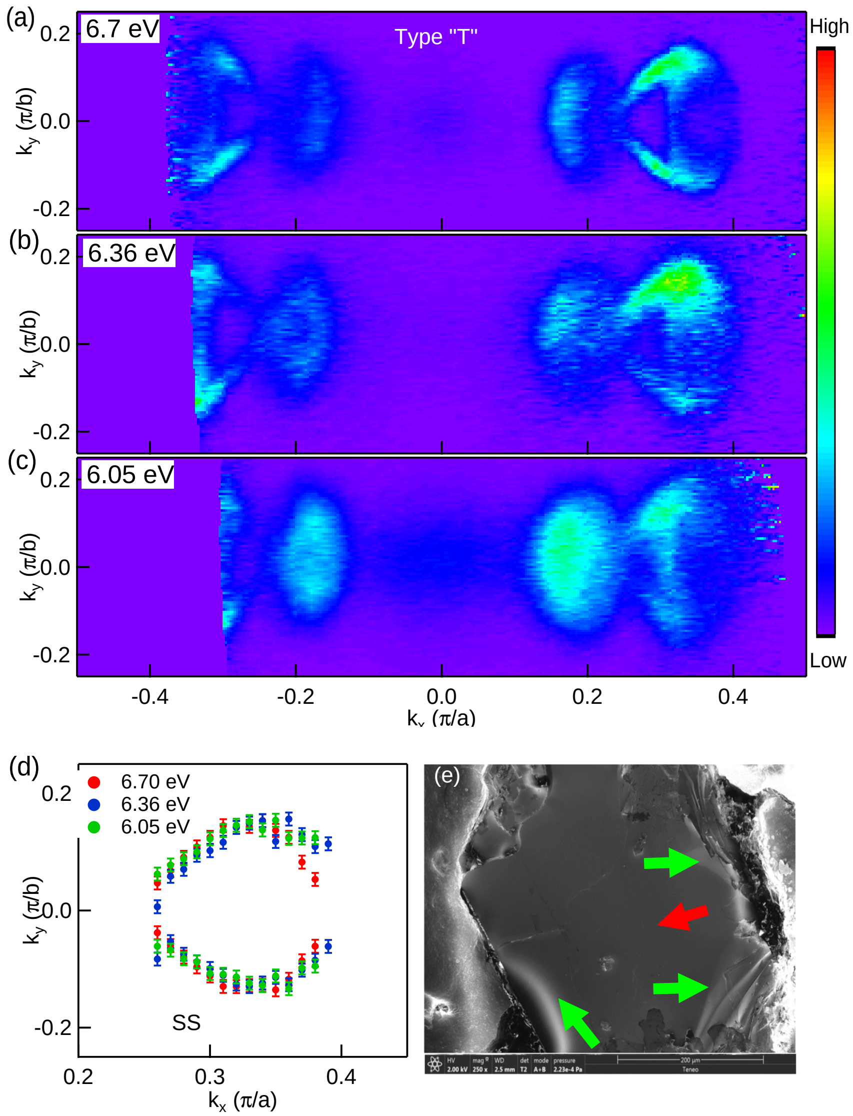

Figure 5.10 Fermi surface plot measured at T = 40 K. (a)-(c) Fermi surface plot of ARPES intensity integrated within 10 meV about the chemical potential measured at photon energies of 6.7, 6.36, and 6.05 eV, respectively. (d) Fermi surface contour extracted from peak positions of momentum dispersion curves. (e) Scanning electron microscopy (SEM) image of cleaved sample surface. The red arrow points to the flat area close to the sample center, while green arrows point to area away from the center where buckling and thus strain is present.

The outlines of the central section of the Fermi arcs remains the same for all three photon energies. As discussed previously [44, 141, 142], the electronic structure of WTe_2 and $MoTe_2$ may change significantly even if a small change in the lattice parameters (e.g., strain) is considered in band structure calculations. By performing high precision SEM measurements using various backscattering geometries we found that close to the center of the sample, the surface is relatively flat. Closer to the edges of the cleaved sample, where ARPES data shows mostly N-type domains, we observed buckling of the sample surface which demonstrates the presence of strain as shown in Fig. 5.10(e). These results are strong evidences that strain/pressure could be the cause of the topological phase transition in this material.

In summary, we have used ultrahigh resolution, tunable, laser-based ARPES to study the electronic properties of WTe_2, a compound that was predicted to be a type-II Weyl semimetal. We found two different cleave types that have distinct electronic structure. The first type is consistent with previous studies, while the second type displays clear Fermi arcs that connect the hole and electron pockets. The coexistence of the trivial and topological domains is most likely due to the presence of inhomogeneous strain, which can be tune topological properties of this material [44]. The Fermi arcs reported here are long sought after signatures of the type-II Weyl semimetallic state that ere predicted by theory [44].

Note added. Recently, we become aware of results presenting ARPES data that are consistent with ours [81, 82, 151]. We note that Bruno et al. [81] considers the observed surface state topologically trivial and inconclusive to establish the presence of a type-II Weyl state. While it is true that Weyl points in WTe_2 are too high above the E_F to be observed directly with ARPES, given the rarity of Fermi arcs in solid state and good agreement between data and theory prediction we argue that our interpretation is a very reasonable one. We are not aware of any other theory that could explain the presence of Fermi arcs in a trivial material.

5.2.4 Acknowledgements

We would like to thank Nandini Trivedi and Timothy McCormick for very useful discussions and Matthew Kramer for assistance with SEM experiments. Funding agencies are the same as presented in Section 5.1.4.

5.3 Three-dimensionality of the bulk electronic structure in WTe_2

The following context is to be submitted to peer-reviewed journal

5.3.1 Introduction

Extremely large magnetoresistance, i.e., dramatic increase in the resistance of a material at low temperatures and high magnetic fields, has attracted great interest recently [67, 100, 113]. Materials with this type of property can be potentially very useful for applications such as low temperature magnetic field sensors. Among the first few extremely large magnetoresistive materials, $PtSn_4$ [67] has been reported to host unusual Dirac node arc structures, that is the Dirac dispersion extending in momentum space in one dimension and gapped out at both ends [148]. Cd_3As_2 [113] was shown to be one of the first three-dimensional Dirac semimetals with linear energy momentum dispersion along all three directions [26, 29, 30, 32, 79]. WTe_2 [100] has been reported to exhibit pressure-induced superconductivity [106, 149], and pressure-induced Lifshitz phase transition was proposed to explain the emergence of the superconductivity [106]. Surprisingly, temperature-induced Lifshitz transition was recently observed in WTe_2. The significant shift of the chemical potential with moderate temperature change is caused by the close proximity of electron and hole densities of states near the Fermi energy [84]. More interestingly, WTe_2 was the first material proposed to be a type-II Weyl semimetal candidate [44]. Unlike the type-I Weyl semimetal [42, 43, 37, 38, 39, 40, 41], type-II Weyl semimetals have the Weyl points emerging at the touching points of the electron and hole pockets [44]. Recently, multiple ARPES measurements have been reported to have observed the Fermi arc surface states in these compounds [152, 47, 153, 144, 145, 146, 147, 81, 82, 83, 151]. Photon energy dependence measurements have been used to demonstrate the two-dimensionality (surface origin) of the Fermi arc states in WTe_2 [81, 83]. However, detailed measurements of three-dimensional bulk electronic structures are still lacking.

ARPES has been known as the most direct technique to probe the electronic structures of materials [60, 154]. Early ARPES and density-functional based augmented spherical wave calculations have revealed the semimetallic nature of WTe_2 [122]. However, no details close to the proximity of the Fermi level were clearly resolved. More recent and high resolution ARPES data has revealed one pair of electron pockets and one pair of hole pockets with similar size, supporting the electron-hole carrier compensation theory as the primary origin of the extremely large magnetoresistance [118]. By varying the incident photon energies from 40-70 eV, the k_z dispersion of the states were mapped out with some bands showing low dispersion and some showing variations in intensity, but no solid conclusion can be drawn from the data [118]. Another group with high energy and momentum resolution ARPES observed total of nine Fermi pockets. However, no significant photon energy dependence along the out of plane direction was observed due to the limited k_z range [150]. On the other hand, magnetoresistance measurements with varying magnetic field applied at an angle with respect to the c axis of the sample have led to the conclusion of three dimensional electronic structure in WTe_2 [155]. Furthermore, the results from quantum oscillations–another technique to probe the Fermi surface structure–have come to similar conclusions. Angle-resolved quantum oscillation measurements implied strong three-dimensionality of the band structure in this material [123]. Although quantum oscillation is a nice technique to measure extrema of the the Fermi surface topology, the oscillation frequencies obtained from fast Fourier transform (FFT) cannot be perfectly assigned to the correct electron/hole pockets. As in measurements performed under applied pressure, one group has assigned the peaks to one pair of electron and hole pockets [125]. However, the Hall effect measurements from another group found that only electron carriers survive under the high pressure [106], which is consistent with our temperature-induced phase transition in WTe_2 [156]. Thus, in order to demonstrate the three-dimensionality of the electronic structure in WTe_2, ultrahigh resolution ARPES measurements with fine tunable incident photon energies are necessary.

Here, we use the ultrahigh resolution, tunable VUV laser-based ARPES to probe the three-dimensionality of the bulk electronic structure in WTe_2. With the ability of fine tuning of the incident photon energy from 5.77 to 6.7 eV, we have obtained high resolution Fermi surface and band structure. For the incident photon energy of 6.7 eV, the bulk FS consists of two pairs of electron pockets and two pairs of hole pockets, with a hole band barely touching the Fermi level at the Γ point. When decreasing the incident photon energy to 6.36 eV, another pair of tiny electron pockets emerges close to the Γ point, which corresponds to the unaccounted for, super low oscillation frequency observed in the quantum oscillation measurements [125, 156]. Further decreasing the incident photon energy results in the disappearance of the tiny electron pockets, thus the bulk FS has only two pairs of electron and hole pockets left for this range of k_z momenta. Detailed band structure along high symmetry cuts measured using different incident photon energies were performed and demonstrate strong three-dimensionality of the electronic structure in WTe_2. These results are consistent with the band structure calculations and quantum oscillations [100, 125, 156]. Our photon energy dependent ARPES measurements have solved the mystery of the super low frequency peaks reported by several quantum oscillation measurements [125, 156].

5.3.2 Methods

5.3.2.1 Sample growth.

Sample growth is the same as described in Section 5.1.2.1.

5.3.2.2 ARPES measurements.

Samples were cleaved *in situ* at 40 K under ultrahigh vacuum (UHV). The data were acquired using a tunable VUV laser ARPES system that consists of a Scienta R8000 electron analyzer, picosecond Ti:Sapphire oscillator and fourth harmaonic generator[69]. Data were collected with a tunable photon energies from 5.3 eV to 6.7 eV. Momentum and energy resolution were set at ~ 0.005 Å^{-1} and 2 meV. The size of the photon beam on the sample was ∼30 μm.

5.3.3 Results and Discussion

Fig. 5.11 shows the ARPES intensity measured at the photon energy of 6.7 eV and temperature of 40 K. Figs. 5.11(a) and (b) show the constant energy contour intensity plots integrated within 10 meV of the chemical potential and at binding energy of 25 meV, respectively. The pockets marked by the black arrow shrink, while the pockets marked by the red arrows expand at higher binding energy, indicating their electron and hole characters, respectively. The hole pockets on the right hand side of the Γ point show clear degeneracy, which is more evident in

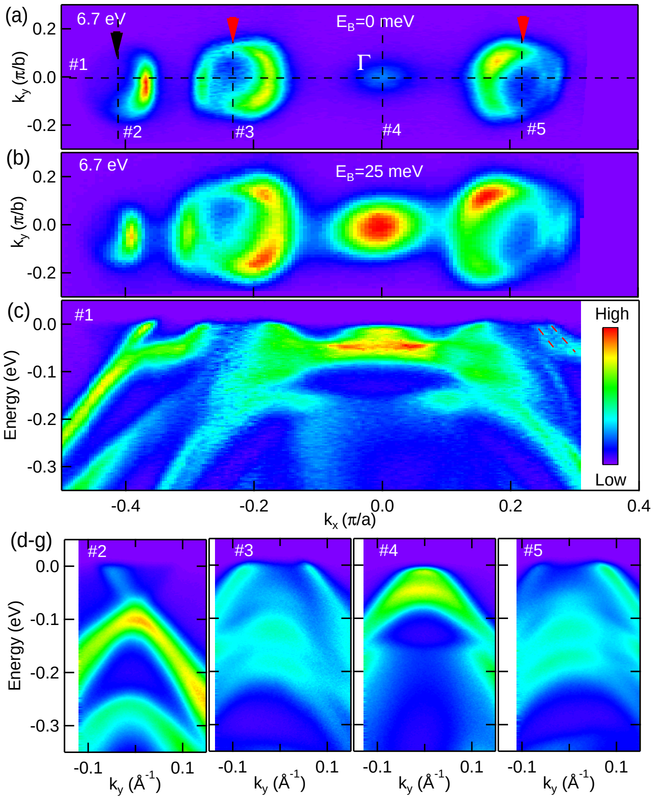

Figure 5.11 Constant energy contour plots and band dispersion measured at $T = 40$ K and photon energy of 6.7 eV. (a) Fermi surface plot of ARPES intensity integrated within 10 meV about the chemical potential. The red arrow points to the pair of electron pockets and the red arrows point to the pairs of hole pockets. (b) Constant energy contour of ARPES intensity integrated within 10 meV at the binding energy of 25 meV. (c)-(g) Band dispersion along cuts #1–5. Red dashed lines in (c) mark the two right branches of the two hole pockets.

the band dispersion along cut #1 as shown in Fig. 5.11(c). The red dashed lines in (c) mark the right two branches of the almost degenerate hole pockets. Unlike the previously reported ARPES measurements at the photon energy of 5.77 eV [156], the separation of the hole pockets at the left hand side of the Γ point is not that significant. Fig. 5.11(d) shows the band dispersion along cut #2, where the asymmetric intensity of the electron pockets is probably due to the matrix element effect. Fig. 5.11(f) shows the band dispersion along cut #4. No clear Fermi crossing is observed providing strong evidence that there are only two pairs of hole pockets and two pairs of electron pockets in the first Brillouin zone measured for the incident photon energy of 6.7 eV.

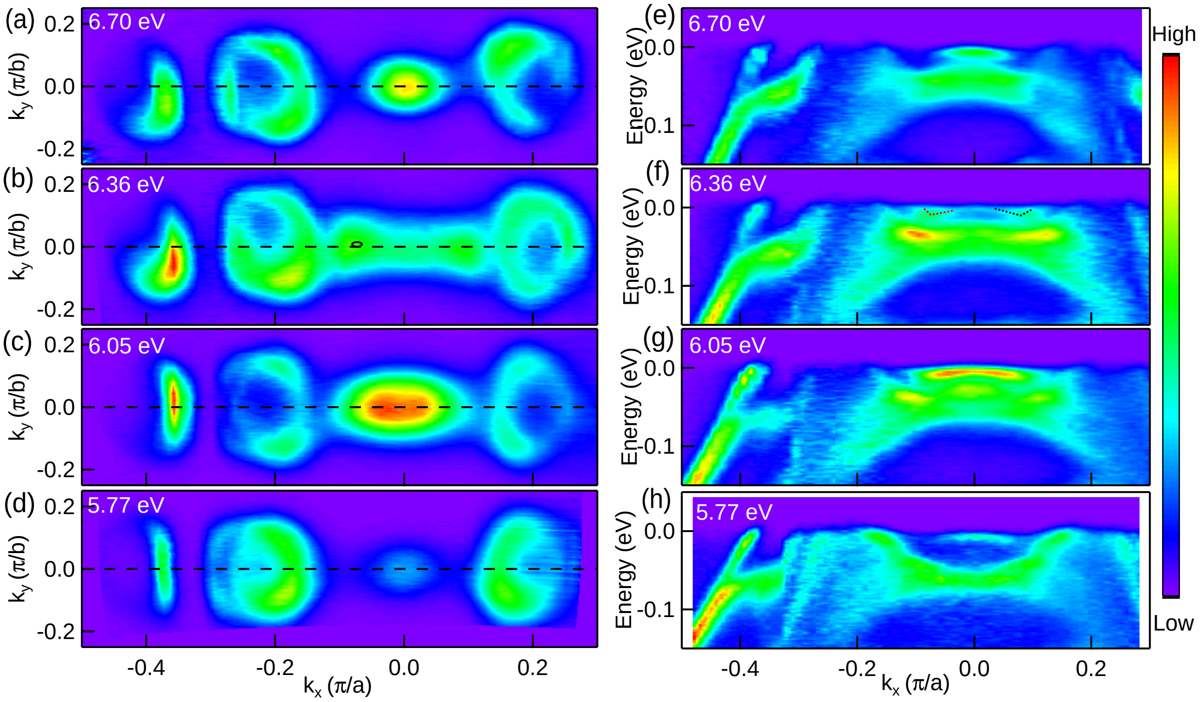

Figure 5.12 Fermi surface plots and band dispersion measured at different photon energies. (a)-(d) Fermi surface plots measured at photon energies of 6.70, 6.36, 6.05, and 5.77 eV, respectively. (e)-(h) Band dispersion along the black dashed lines in (a)-(d), respectively.

By varying the incident photon energies, we are able to map out the band dispersion along the out of plane, (k_z) direction [60, 154]. Synchrotron radiation based ARPES systems are often used for k_z dispersion mapping due to the large tunable range of the incident photon energies. However, tuning photon energies with coarse steps ≥ 1 eV would result in some important details being omitted along very important k_z dispersion [118, 150]. With the photon energy tunability from 5.7 eV to 7 eV with rather fine energy steps in our laser-based ARPES system, we mapped out the k_z dispersion of WTe_2 in great detail. Fig. 5.12 shows the FS and band dispersion measured using the incident photon energies of 6.70, 6.36, 6.05, and 5.77 eV, respectively as indicated at the top left corner of each plot. In Figs. 5.12(a)-(d), we can see that the FS of WTe_2 measured at different photon energies look similar, with two pairs of electron pockets and two pairs of hole pockets in the first BZ. However, significant difference is also observed. The hole band at the Γ point has different intensities and curvatures, although

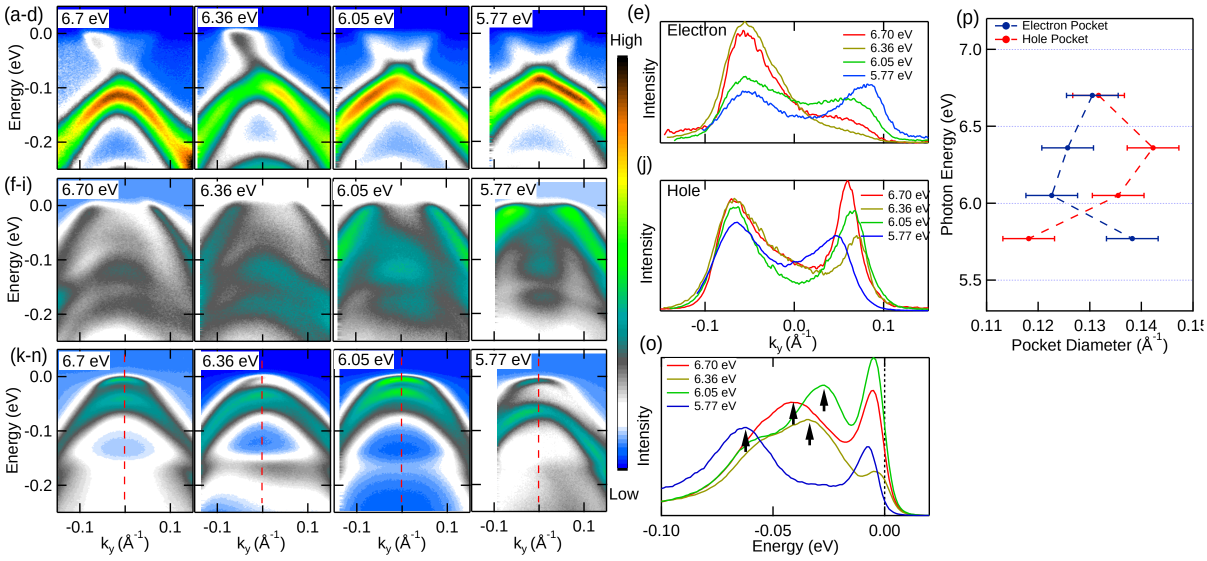

Figure 5.13 Band dispersion, momentum dispersion curves, and energy dispersion curves measured at different photon energies. (a)-(d) Band dispersion along the cut #2 in Fig. 5.11(a) measured at photon energies of 6.7, 6.36, 6.05, and 5.77 eV, respectively. (e) Momentum dispersion curves at the E_F of (a)-(d). (f)-(i) Band dispersion along the cut #3 in Fig. 5.11(a) measured at photon energies of 6.7, 6.36, 6.05, and 5.77 eV, respectively. (j) Momentum dispersion curves at the E_F of (f)-(i). (k)-(n) Band dispersion along the cut #4 in Fig. 5.11(a) measured at photon energies of 6.7, 6.36, 6.05, and 5.77 eV, respectively. (o) Energy dispersion curves along the red dashed lines in (k)-(n). Black arrows point to the locations of the lower hole bands in (k)-(n). (p) Diameters of the electron and hole pockets measured at different photon energies extracted from the momentum dispersion curves in (e) and (j).

none of them has crossed the Fermi level as shown in Figs. 5.12(e)-(h). Furthermore, the FS close to the Γ point in Fig. 5.12(b) shows a dumb-bell like structure, while all the other three FSs show only a single hole band at the Γ point. The band dispersion along the black dashed line in Fig. 5.12(b) is shown in (f). On both sides of the Γ point, one tiny electron pocket is clearly visible [marked by the red dotted lines in panel (f)], which is significantly different from the band dispersion measured at other photon energies. By re-examining the quantum oscillation data that we have published in the previous paper [156] and other group's results [125], we found that there is a super low frequency that was not assigned to any Fermi surface and initially was most likely attributed to noise. Furthermore, the electronic structure calculations after taking into account the spin-orbit coupling in WTe_2 clearly bring extra tiny electron pockets close to the Γ point [100]. Thus, our ARPES results have solved the mystery of this unaccounted for, low frequency in quantum oscillation peak. We should note that as the electronic structure of WTe_2 is very sensitivity to pressure/strain [106, 149, 44, 83] and even temperature [156], it is possible that these tiny electron pockets might be suppressed in some of the quantum oscillation measurements.

Fig. 5.13 shows the detailed band dispersion measured along high symmetry directions using various photon energies. Panels (a)–(d), (f)–(i), and (k)–(n) present the band dispersions measured using the photon energy of 6.7, 6.36, 6.05 and 5.77 eV, respectively, and correspond to the high symmetry cuts as marked #2, 3, and 4 in Fig. 5.11. In panels (a)–(d), only minor intensity differences can be seen between the four measurements. At the photon energy of 6.05 and 5.77 eV, the electron pockets are clear and symmetric. On the other hand, the electron pockets measured at the photon energy of 6.7 and 6.36 eV are not symmetric in intensity, probably due to the matrix elements effect. To quantify the electron pocket sizes in panels (a)–(d), we have plotted the momentum dispersion curves (MDCs) at the Fermi level E_F in Fig. 5.13(e). The peak locations of the MDCs show clear differences across these four photon energies (peak locations of the left branches are aligned for easy comparison). Panels (f)–(i) present the band dispersion from cut #3, which clearly shows that the hole pocket measured with 5.77 eV photons is significantly smaller than the other three. Panel (j) shows the MDCs at the E_F from panels (f)–(i), illustrating different hole pocket sizes [also left aligned as in (e)]. Panels (k)–(n) show the photon energy dependence of the hole bands at the Γ point (cut #4 in Fig. 5.11). Two hole bands can be clearly seen at the Γ point with different separations between them for different photon energies. Panel (o) shows the energy dispersion curves (EDCs) from panels (k)–(n), where the black arrows point to the peak locations in the lower hole bands. The top hole bands sit at roughly the same binding energy for these photon energies, but none of them crosses the Fermi level. On the other hand, the distance between the top and lower hole bands is very different across these photon energies, with 5.77 eV showing the maximum separation. By fitting two Lorentzian functions to the MDCs in panels (e) and (j), we calculate the electron/hole pocket sizes and summarize the results in panel (p). With the increasing incident photon energy, the size of the electron pocket decreases and then increases. On the other hand, the size of the hole pocket increases and then decreases. This trend is consistent with the band structure calculations shown in Ref. [100], where the hole pockets have a concave shape and the electron pockets have a convex shape along k_z direction toward the center of the zone.

In conclusion, we used the ultra high resolution laser based ARPES system to investigate the electronic structure of WTe_2. The photon energy dependence measurements with relatively fine energy steps have revealed the three-dimensional characteristic of the electron and hole pockets along the Γ-Z direction. With the increasing incident photon energy from 5.77 to 6.70 eV, the hole pocket expands and then shrinks, while the electron pocket displays opposite behavior. Strong photon energy dependence is also observed in the hole bands at the Γ point. Furthermore, we have revealed a pair of tiny electron pockets sitting at the opposite side of the Γ point at the photon energy of 6.36 eV, providing strong evidence for the low quantum oscillation frequency that was not accounted for in the previous studies.

5.3.4 Acknowledgements

Funding agencies are the same as presented in Section 5.1.4.

CHAPTER 6. DIRAC NODE ARC METAL $PtSn_4$

6.1 Dirac Node Arcs in $PtSn_4$

The following context is an extended version of the published work in
Nature Physics **12**, 667

6.1.1 Introduction

In topological quantum materials [20, 157, 158] the conduction and valence bands are connected at points or along lines in the momentum space. A number of studies have demonstrated that several materials are indeed Dirac/Weyl semimetals [28, 29, 37, 41, 80]. However, there is still no experimental confirmation of materials with line nodes, in which the Dirac nodes form closed loops in the momentum space [157, 158]. Here we report the discovery of a novel topological structure – Dirac node arcs – in the ultrahigh magnetoresistive material $PtSn_4$ using laser-based angle-resolved photoemission spectroscopy data and density functional theory calculations. Unlike the closed loops of line nodes, the Dirac node arc structure arises owing to the surface states and resembles the Dirac dispersion in graphene that is extended along a short line in the momentum space. We proposed that this reported Dirac node arc structure is a novel topological state that provides an exciting platform for studying the exotic properties of Dirac fermions.

The discovery of nontrivial surface states in topological insulators [20] attracted a lot of interest and initiated quests for diverse novel topological states in condensed matter. Topological nodal states with conduction and valence bands touching at points (Dirac/Weyl semimetals) or lines (line node semimetals) have been proposed to exist in multilayer heterostructures [157]. A possible extension of these states to three dimensional (3D) single crystals was proposed in

β-cristobalite BiO_2 (ref. [24]) and A_3Bi (A = Na, K, Rb; ref. [27]), which are thought to host bulk 3D Dirac points protected by crystal symmetry. Subsequently, Na_3Bi and Cd_3As_2 were experimentally demonstrated to be 3D Dirac semimetals [26, 28, 29, 30]. Subsequently, another type of massless particle–the Weyl fermion [139]–was found in states that were predicted to exist in a family of non-centrosymmetric transition metal TaAs, TaP, NbP and NbAs (refs [42, 30]). These materials were confirmed as Weyl semimetals by reports of Fermi arc states connecting the Weyl points as a unique signature [37, 41, 80]. Although experimental evidence supports the existence of Dirac semimetals and Weyl semimetals, clear signatures of semimetals with line nodes are yet to be discovered. Several groups proposed that line node structures may exist in graphene networks [54], rare earth monopnictides [159], antiperovskite Cu_3PdN/Cu_3ZnN (refs [160, 161], $SrIrO_3$ (ref. [162]), $TlTaSe_2$ (ref. [163]), Ca_3P_2 (ref. [164]) and CaAgX (X=P, As; ref. [165]), but so far no direct evidence has been reported. Several angle-resolved photoemission spectroscopy (ARPES) studies in $PbTaSe_2$ (ref. [53]) and ZrSiS (ref. [87]) presented some evidence of the existence of Dirac-like features and 'Drumhead'surface states, but further research is till needed to understand fully their significance and relation to Dirac line nodes.

Many topological nodal semimetals, such as Cd_3As_2 (ref. [113]), NbP (ref. [166]) and WTe_2 (ref. [100]), exhibit extremely large magnetoresistance. Before these discoveries, a similar effect was observed in $PtSn_4$ [67].

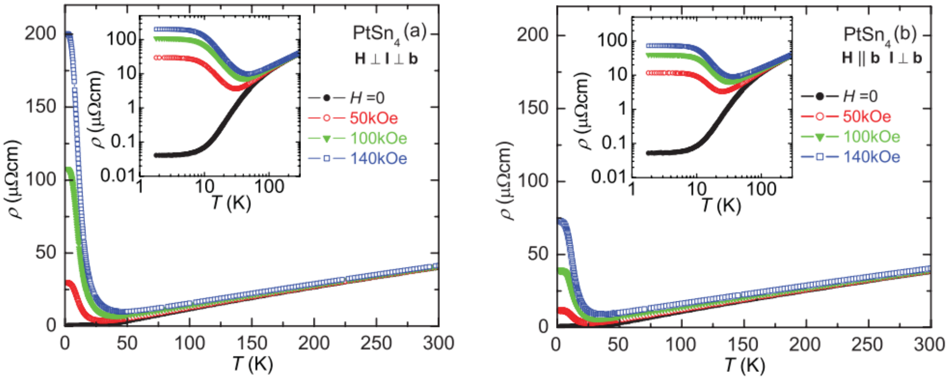

Figure 6.1 Resistivity measurements as a function of temperature and field of $PtSn_4$. (a) Temperature-dependent resistivity for an applied field along the **ac** plane ($\mathbf{H} \perp \mathbf{b}$). (b) The same as (a) with field along the **b** axis ($\mathbf{H} \parallel \mathbf{b}$). Insets (a) and (b) are $\rho(T)$ vs $\log(T)$ plot. (From Ref. [67])

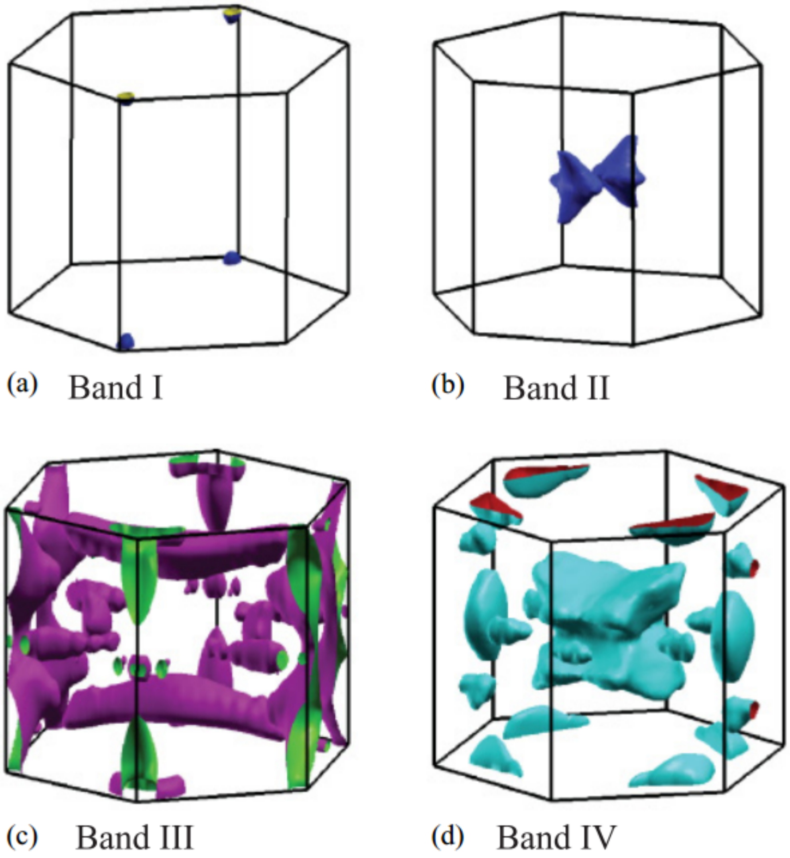

Figure 6.2 The theoretically calculated Fermi surface of $PtSn_4$. (From Ref. [67])

Fig. 6.1 shows the resistivity measurements as a function of temperature and field of $PtSn_4$ along two different directions: $\mathbf{H} \perp \mathbf{b}$ and $\mathbf{H} \parallel \mathbf{b}$. Although extremely large magnetoresistance has been observed along both directions, a strong anisotropy can be also clearly seen. The magnetoresistance along $\mathbf{H} \perp \mathbf{b}$ reaches up to $5 \times 10^5\%$ at 1.8 K and 140 kOe, while the other direction only $1.4 \times 10^5\%$ [67].

As shown in Fig. 6.2, the bulk Fermi surface of $PtSn_4$ is three dimensional, and very complex with Fermi surface pockets spreading across the Brillouin zone [67]. As we have already illustrated in Figs. 2.5 and 2.9, strong three-dimensionality in the Fermi surface close to the zone center is observed. These results are consistent with the complex band structure calculations in Fig. 6.2. Here we demonstrate that, despite its complex FS in the centre region of the Brillouin zone, there are also very interesting features close to the boundary of the zone, that is, the Z and X points, which are the signatures of a topological quantum material. Whereas most of the topological quantum materials were predicted by theory first and verified by experiment later, we present an opposite approach: we focused on ultrahigh non-saturating magnetoresistance, and on this basis we searched for topological states in $PtSn_4$ by means of ultrahigh resolution ARPES, followed with band structure calculations.

6.1.2 Methods

6.1.2.1 Sample growth.

Single crystals of $PtSn_4$ were grown out of a Sn-rich binary melt [92]. The constituent elements, with an initial stoichiometry of $Pt_{0.04}Sn_{0.96}$, were placed in an alumina crucible and sealed in a quartz tube under a partial Ar pressure. After the quartz ampoule was heated up to 600°C, the ampoule was cooled down to 350°C over 60 h (ref. [67]). To decant the Sn readily at this temperature, a frit-disc crucible was used [93].

6.1.2.2 Sample preparation and measurements.

ARPES measurements were carried out using a laboratory-based system consisting of a Scienta R8000 electron analyser and a a tunable vacuum ultraviolet (VUV) laser light source consisting of picosecond Ti:Sapphire oscillator and fourth harmonic generator [69]. All Data were collected with a constant photon energy of 6.7 eV, except for Fig.6.6g (6.36 eV) and 6.6h (6.05 eV). The angular resolution was set at $\sim 0.05^\circ$ and 0.5° (0.005 Å^{-1} and 0.05 Å^{-1}) along and perpendicular to the direction of the analyser slit (and thus cut in the momentum space), respectively; and energy resolution was set at 1 meV. The size of the photon beam on the sample was ∼30 μm. Samples were cleaved *in situ* at a base pressure lower than 1×10^{-10} Torr. Samples were cooled using a closed-cycle He refrigerator and the sample temperature was measured using a silicon-diode sensor mounted on the sample holder. The energy corresponding to the chemical potential was determined from the Fermi edge of a polycrystalline Au reference in electrical contact with the sample. Samples were cleave at 40K and were kept at the cleaving temperature throughout the measurement.

6.1.2.3 Calculation method.

Density functional theory [94, 95] (DFT) calculations were done in the Vienna *Ab initio* Simulation Package (VASP; refs [96, 97]) using the Perdew-Burke-Ernzerhof (PBE; ref. [98]) exchange-correlation functional, a plane-wave basis set with projected augmented waves [99] and spin-orbital coupling (SOC) effect included. For bulk-band structure of $\mathrm{PtSn_4}$, we use the conventional orthorhombic cell of 20 atoms with a Monkhorst-Pack [167] $(8 \times 6 \times 8)$ k-point mesh. For surface-band structure, we use slabs up to 96 atomic layers or 320 atoms with a $(8 \times 1 \times 8)$ k-point mesh and at least a 12 Å vacuum. The kinetic energy cutoff is 230 eV. The convergence with respect to k-point mesh was carefully checked, with total energy converged, for example, well below 1 meV/atom. We use experimental lattice parameters [168] of $a = 6.418$ Å, $b = 11.366$ Å, and $c = 6.384$ Å with atoms fixed in their bulk positions.

6.1.3 Results and Discussion

The crystal structure, Fermi surface and band dispersion along key directions in the Brillouin zone (BZ) for $\mathrm{PtSn_4}$ are shown in Fig. 6.3. Figure 6.3b shows the ARPES intensity integrated within 10 meV of the chemical potential. High-intensity areas mark the contours of the FS sheets. The FS consists of at least one large electron pocket at the centre of BZ, surrounded by several other electron and hole FS sheets, consistent with the quantum oscillation result [67]. Figure 6.3c shows the calculated bulk FS, which matches the data well close to the centre of the zone and Z point in Fig. 6.3b, and is also consistent with the calculated FS using the full potential linearized augmented plane wave (FLAPW) method within the local density approximation (LDA; ref. [67]). However, it does not predict the FS crossings close to the X point, missing a set of nearly parallel FS sheets that are present in Fig. 6.3b. On the other hand, these experimental features are reproduced well by a calculation of the surface sates using the slab method; results of which are shown in Fig. 6.3d. Band dispersions along several cuts in proximity to the Z and X points are shown in Fig. 6.3e–l. Close to the Z point (Fig. 6.3e, g), the dispersion resembles a Dirac-like feature, but the intensity within the band contour indicates a bulk origin and is consistent with corresponding band calculations shown in

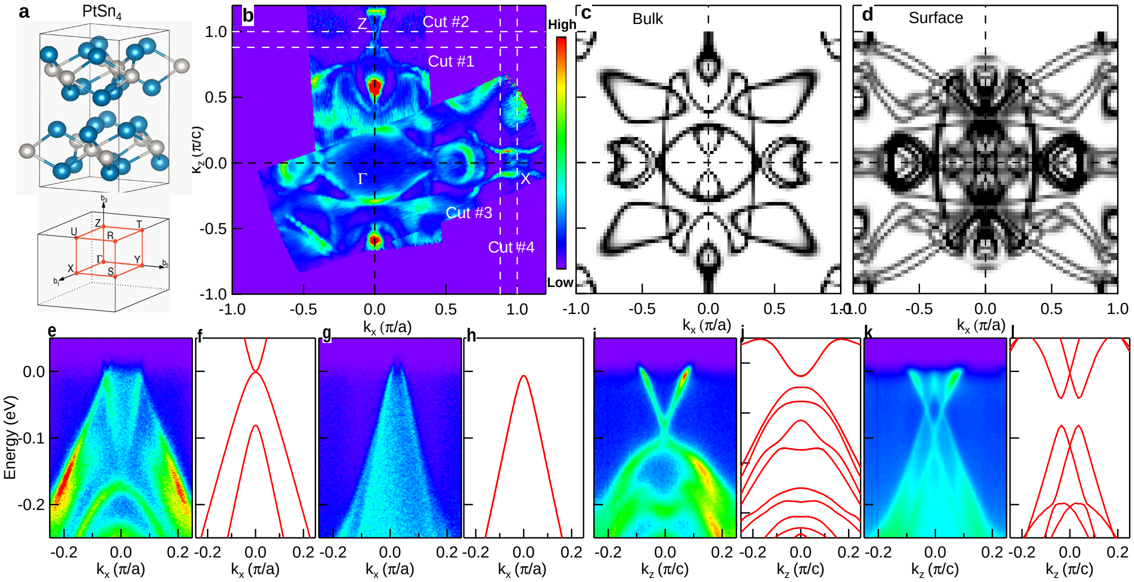

Figure 6.3 Experimental and calculated Fermi surface and band dispersion of PtSn$_4$. **a** Crystal structure (Pt: white spheres, Sn: blue spheres) and Brillouin zone of PtSn$_4$. **b** Fermi-surface plot of ARPES intensity integrated within 10 meV of the chemical potential along $\Gamma - Z$ and $\Gamma - X$. **c** DFT-calculated bulk FS slice at $k_y = 0.284\ \pi/b$. **d** Calculated surface FS with a 24-layer slab. **e** Band dispersion at $k_z = 0.88\ \pi/c$ along cut #1 in **b**. **f** Calculated bulk-band dispersion at $k_z = 0.88\ \pi/c$ and $k_y = 0.284\ \pi/b$. **g** Band dispersion at $k_z = \ \pi/c$ along cut #2 in **b**. **h** Calculated bulk-band dispersion at $k_z = \ \pi/c$ and $k_y = 0.284\ \pi/b$. **i** Band dispersion at $k_x = 0.88\ \pi/a$, similar to cut #3 in **b**. **j** Calculated surface-band dispersion at $k_x = 0.88\ \pi/a$ with 42-layer slab. **k** Band dispersion at $k_x = \ \pi/a$ along cut #4 in **b**. **l** Calculated surface-band dispersion at $k_x = \ \pi/a$ with 42-layer slab.

Fig. 6.3f, h. Close to the X point (Fig. 6.3i, k), the band dispersion is also Dirac-like, but very sharp, and thus more likely to be due to surface states; moreover, it is consistent with the slab calculation shown in Fig. 6.3j, l. The data in Fig. 6.3 demonstrate that the experimentally observed band structure has both bulk and surface components. The former dominate the Fermi surface close to the Z point, and the latter is prominent close to the X point. The linear dispersion and gapless band crossings strongly suggest that both bulk and surface features at the edge of the Brillouin zone may have topological character, possibly linked to the ultrahigh magnetoresistance, similar to Cd$_3$As$_2$ (ref. [29]), NbP (ref. [80]) and WTe$_2$ (ref. [156]).

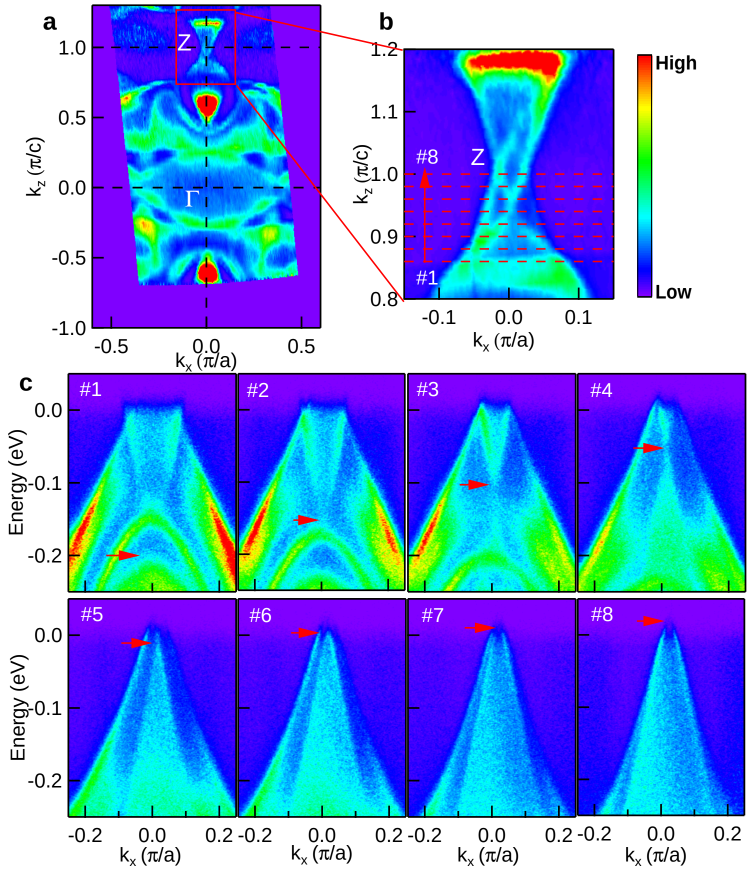

Figure 6.4 Fermi surface and band dispersion in the proximity of the Z point. **a** Fermi surface plot of ARPES intensity integrated within 10 meV of the chemical potential along $\Gamma - Z$. **b** Zoom in image of the red box in Fig.6.4**a**, red dashed lines mark the cut #1 – #8. **c** Band dispersion along cut #1 – #8. Cut #8 is cutting through the Z point. The red arrows mark the Dirac nodes.

In Fig. 6.4 we focus on the interesting features near the Z point in more detail. An enlarged image from the red box in Fig. 6.4a is shown in panel b, where two triangular-shaped FS sheets are observed. The detailed evolution of band dispersions along cuts no. 1 to no. 8 is shown in Fig. 6.4c. A sharp linear dispersion starts to cross at a binding energy of $\sim$ 200 meV in cut no. 1, and the Dirac point moves up in energy in cuts no. 2– no. 5, finally reaching the Fermi level in cut no. 6, as indicated by red arrows. The the Dirac point moves up above the Fermi level and becomes a sharp, shallow hole pocket in cuts no. 7 and no. 8. This movement of the Dirac nodes forms a line in the energy-momentum space in the proximity of Z.

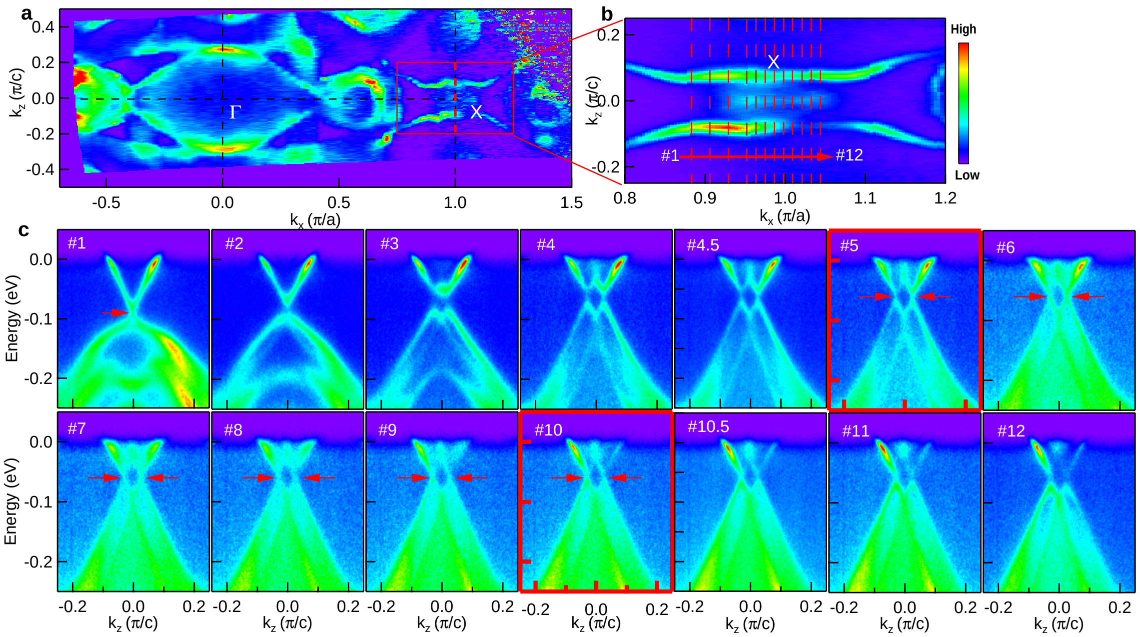

Figure 6.5 Fermi Surface plot and band dispersion close to the X point. **a** Fermi surface plot of ARPES intensity integrated within 10 meV of the chemical potential along $\Gamma - X$. **b** Zoom in image of the red box in Fig.6.5**a**, red dashed lines mark the cut #1 – #12. **c** Band dispersion along cut #1 – #12. Cut #8 is cutting through the X point. The red arrows mark the Dirac nodes. #5 and #10 (in red box) are the dispersion at the end point of the Dirac node arcs.

Whereas the behaviour described above has previously been predicted by theory, the structure in the proximity of the X point is far more interesting. We now examine the Fermi surface and band dispersion in a small area in the part of the Brillouin zone that is marked by the red box in Fig. 6.5a. The Fermi surface in this region consists of a short arc along the symmetry line and two longer, nearly parallel segments on either side of this arc. Detailed band dispersion along cuts no. 1 to no. 12 are shown in Fig. 6.5c. The data along cut no. 1 show Dirac-like dispersion, with the top and bottom bands merging at a single gapless point. The band is very sharp, consistent with its surface origin. As we move closer to the X point, two things happen: a gap develops between top and bottom bands and both top and bottom bands split into two parts symmetric about the k_z=0 line (cuts no. 2–no. 4). Before reaching the X point, the gap vanishes and there are two gapless Dirac-like features in close proximity to the X point. The inner bands of the two Dirac features merge along the symmetry line and form an arc at the chemical potential visible in Fig. 6.5b. The two gapless, Dirac-like features extend along one direction in the proximity of the X point between $k_x \approx 0.95\pi/a$ and $1.05\pi/a$ (cuts no. 5 and no. 10 marked by the red frame in Fig. 6.5c). Outside this momentum range a gap develops, separating the upper and lower portion of the band that is, cuts no. 4.5 and no. 10.5 are already gapped. This gives rise to two arcs of Dirac nodes located at a binding energy of ~ 60 meV, one on each side of the $\Gamma - X$ symmetry line, which we named Dirac node arcs.

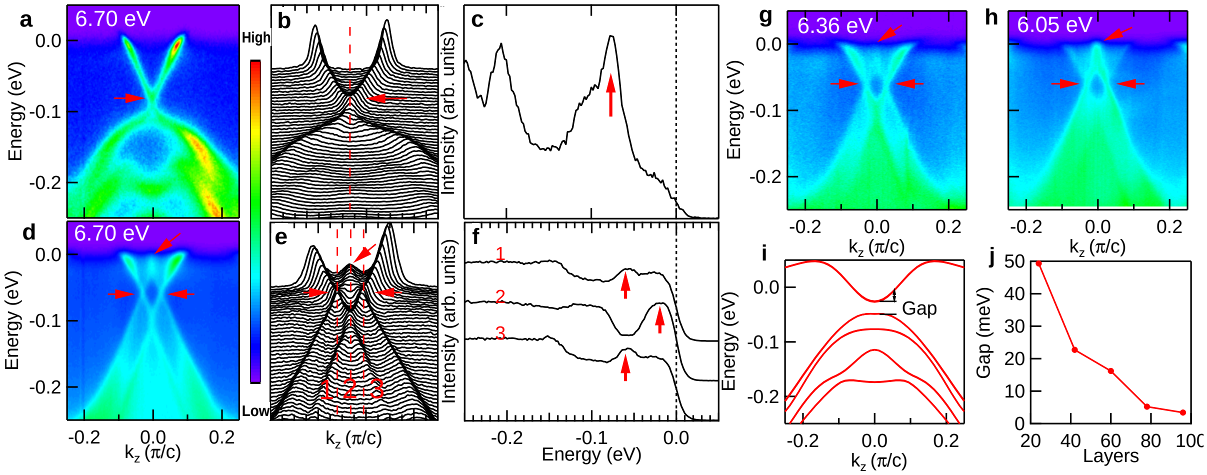

Figure 6.6 Two types of gapless Dirac-like dispersion close to X point. **a** Band dispersion along cut #1 in Fig.6.5**b** measured at photon energy of 6.70 eV. **b** Momentum Dispersion Curves (MDC) of **a**. **c** Energy Dispersion Curve (EDC) along the red dashed line in **b**. **d** Band dispersion along cut #8 in Fig.6.5**b** measured at photon energy of 6.70 eV. **e** Momentum Dispersion Curves (MDC) of **d**. **f** Energy Dispersion Curves (EDC) along the red dashed lines in **e**. **g** Band dispersion along cut #8 in Fig.6.5**b** measured at photon energy of 6.36 eV. **h** Band dispersion along cut #8 in Fig.6.5**b** measured at photon energy of 6.05 eV. **i** Calculated surface band along cut at $k_x = 0.88\ \pi/a$, similar to cut #3 in **b**, with a 42-layer slab. **j** Energy-gap evolution with increasing number of layers in the slab.

We now proceed to demonstrate that the Dirac-like dispersion shown in Fig. 6.5 is gapless by plotting the momentum dispersion curves (MDCs) and energy dispersion curves (EDCs). Figure 6.6c shows the EDC extracted along the red dashed line in 4b. The red arrow marks the peak located at roughly 90 meV below the Fermi level (Fig. 6.6a), and demonstrates the absence of an energy gap in this single Dirac-like feature. In Fig. 6.6d, we show the double Dirac-like features along cut no. 8 (Fig. 6.5c). The EDCs shown in 4f are extracted along the red dashed lines marked as 1, 2, 3 in Fig. 6.6e. The red arrows in Fig. 6.6e,f mark the locations of the peaks at a binding energy of ∼60 meV, and show the gapless nature of these dispersions. The same cut measured at two other photon energies (6.36 eV and 6.05 eV) is shown in Fig. 6.6g and h, respectively. It is clear that the band dispersion does not vary with the incident photon energy (within 16% of the Brillouin zone), demonstrating its surface origin. As such, those states do not have dispersion along a direction perpendicular to the sample surface (that is, k_y). The surface-state calculation using a 42-layer slab shows that the conduction and valence bands are separated by roughly 23 meV in the single Dirac feature. However, a further increase in the layer number reduces the gap size significantly, as shown in Fig. 6.6j.

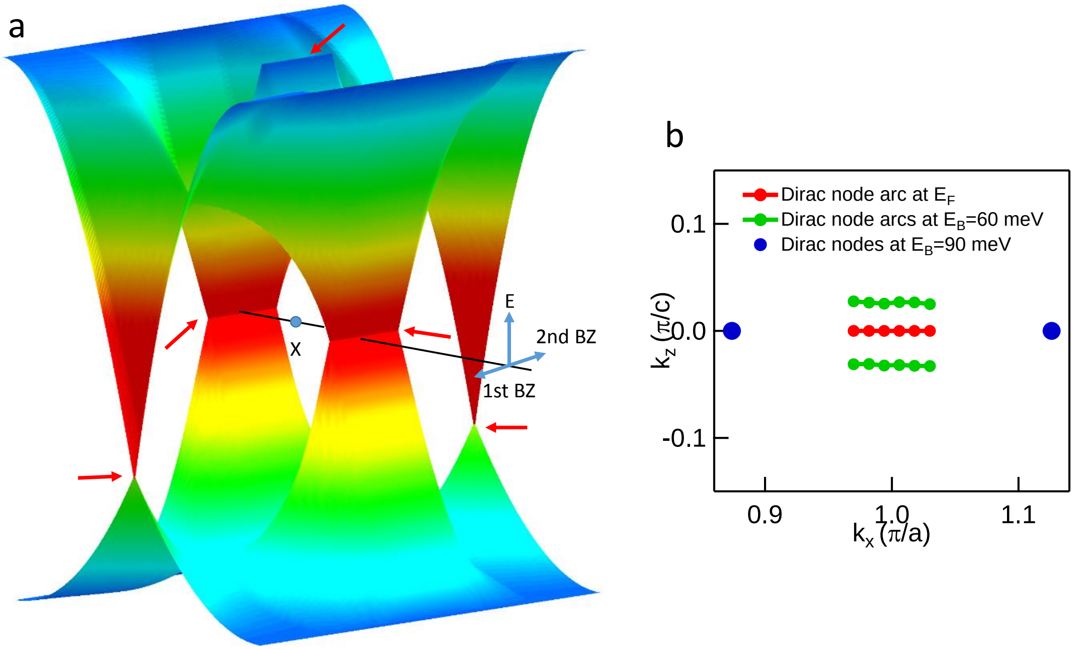

Figure 6.7 Schematic of Dirac node arcs in $\mathrm{PtSn_4}$ close to X point. **a** Schematic of Double Dirac node arc structure. Red arrows mark the double single nodes and double node arcs. **b** Locations of the Dirac nodes extracted from the peak positions of the MDCs as marked by the red dashed lines in **a** and **d**. The blue dots denote the two single Dirac nodes at $\mathrm{E}_B \sim 90$ meV. The green dots denote the two Dirac node arcs at $\mathrm{E}_B \sim 60$ meV. The red dots denote the Dirac node arc at E_F.

In Fig. 6.7a, the schematic of the double Dirac node arc structure is shown, with two Dirac dispersions extending along one dimension in momentum space. To better illustrate the Dirac node arc structure, we plot the location of the Dirac nodes in momentum space in Fig. 6.7b by extracting the peak positions of the MDCs at each node (that is, at a binding energy of 90 meV in the single Dirac dispersion and 60 meV at the proximity of the X point in the double Dirac dispersion, as marked by the red dashed lines in Fig. 6.6a, d).

Our results show that, near the X point, the single Dirac dispersion evolves into two gapped dispersions and, before reaching the X point, the gaps close and two gapless Dirac-like feature emerge extending along one dimension in momentum space, forming a Dirac node arc. These novel features differ from previously predicted Dirac line nodes that form closed loops in momentum space. We proposed that this novel topological nodal structure could be an ideal platform for studying the exotic properties of Dirac fermions. Finally, we note that most of the recently discovered ultrahigh magnetoresistive materials [113, 166, 100] seem to also possess Dirac or Weyl features in the band dispersions [29, 80, 156]. As we have demonstrated, this opens an avenue for discovering and identifying novel topological states and relativistic behaviour based on rudimentary transport measurements.

6.1.4 Acknowledgements

This work was supported by the US Department of Energy, Office of Science, Basic Energy Sciences, materials Science and Engineering Division. Ames Laboratory is operated for the US Department of Energy by Iowa State University under contract No. DE-AC02-07CH11358.

BIBLIOGRAPHY

[1] N.W. Ashcroft and N.D. Mermin. *Solid State Physics.* Saunders College, Philadelphia, 1976.

[2] K. v. Klitzing, G. Dorda, and M. Pepper. New method for high-accuracy determination of the fine-structure constant based on quantized Hall resistance. *Phys. Rev. Lett.*, 45:494–497, Aug 1980.

[3] Yuanbo Zhang, Yan Tan, Horst L. Stormer, and Philip Kim. Experimental observation of the quantum Hall effect and Berry's phase in graphene. *Nature (London)*, 438:201–204, 2005.

[4] KSA Novoselov, Andre K Geim, SVb Morozov, Da Jiang, MIc Katsnelson, IVa Grigorieva, SVb Dubonos, and AAb Firsov. Two-dimensional gas of massless Dirac fermions in graphene. *nature*, 438(7065):197–200, 2005.

[5] Konstantin S Novoselov, Z Jiang, Y Zhang, SV Morozov, HL Stormer, U Zeitler, JC Maan, GS Boebinger, P Kim, and AK Geim. Room-temperature quantum Hall effect in graphene. *Science*, 315(5817):1379–1379, 2007.

[6] D. J. Thouless, M. Kohmoto, M. P. Nightingale, and M. den Nijs. Quantized Hall conductance in a two-dimensional periodic potential. *Phys. Rev. Lett.*, 49:405–408, Aug 1982.

[7] M. V. Berry. Quantal phase factors accompanying adiabatic changes. *Proceedings of the Royal Society of London A: Mathematical, Physical and Engineering Sciences*, 392(1802):45–57, 1984.

[8] Charles Kane and Joel Moore. Topological insulators. *Physics World*, 24(02):32, 2011.

[9] Xiao-Liang Qi and Shou-Cheng Zhang. The quantum spin Hall effect and topological insulators. *Physics Today*, 63(1):33–38, 2010.

[10] B. Andrei Bernevig, Taylor L. Hughes, and Shou-Cheng Zhang. Quantum spin Hall effect and topological phase transition in HgTe quantum wells. *Science*, 314(5806):1757–1761, 2006.

[11] Liang Fu and C. L. Kane. Topological insulators with inversion symmetry. *Phys. Rev. B*, 76:045302, Jul 2007.

[12] Markus König, Steffen Wiedmann, Christoph Brüne, Andreas Roth, Hartmut Buhmann, Laurens W. Molenkamp, Xiao-Liang Qi, and Shou-Cheng Zhang. Quantum spin Hall insulator state in HgTe quantum wells. *Science*, 318(5851):766–770, 2007.

[13] D Hsieh, D Qian, L Wray, Y Xia, Y S Hor, R J Cava, and M Z Hasan. A topological Dirac insulator in a quantum spin Hall phase. *Nature*, 452(7190):970–974, apr 2008.

[14] Haijun Zhang, Chao-Xing Liu, Xiao-Liang Qi, Xi Dai, Zhong Fang, and Shou-Cheng Zhang. Topological insulators in Bi_2Se_3, Bi_2Te_3 and Sb_2Te_3 with a single Dirac cone on the surface. *Nat. Phys.*, 5(6):438–442, 2009.

[15] D. Hsieh, Y. Xia, D. Qian, L. Wray, J. H. Dil, F. Meier, J. Osterwalder, L. Patthey, J. G. Checkelsky, N. P. Ong, A. V. Fedorov, H. Lin, A. Bansil, D. Grauer, Y. S. Hor, R. J. Cava, and M. Z. Hasan. A tunable topological insulator in the spin helical Dirac transport regime. *Nature (London)*, 460:1101–1105, 2009.

[16] Y. L. Chen, J. G. Analytis, J.-H. Chu, Z. K. Liu, S.-K. Mo, X. L. Qi, H. J. Zhang, D. H. Lu, X. Dai, Z. Fang, S. C. Zhang, I. R. Fisher, Z. Hussain, and Z.-X. Shen. Experimental Realization of a Three-Dimensional Topological Insulator, Bi_2Te_3. *Science*, 325(5937):178–181, 2009.

[17] D. Hsieh, Y. Xia, D. Qian, L. Wray, F. Meier, J. H. Dil, J. Osterwalder, L. Patthey, A. V. Fedorov, H. Lin, A. Bansil, D. Grauer, Y. S. Hor, R. J. Cava, and M. Z. Hasan.

Observation of Time-Reversal-Protected Single-Dirac-Cone Topological-Insulator States in Bi_2Te_3 and Sb_2Te_3. *Phys. Rev. Lett.*, 103:146401, Sep 2009.

[18] Liang Fu. Hexagonal Warping Effects in the Surface States of the Topological Insulator Bi_2Te_3. *Phys. Rev. Lett.*, 103:266801, Dec 2009.

[19] Y. H. Wang, D. Hsieh, D. Pilon, L. Fu, D. R. Gardner, Y. S. Lee, and N. Gedik. Observation of a Warped Helical Spin Texture in Bi_2Se_3 from Circular Dichroism Angle-Resolved Photoemission Spectroscopy. *Phys. Rev. Lett.*, 107:207602, Nov 2011.

[20] M. Z. Hasan and C. L. Kane. *Colloquium* : Topological insulators. *Rev. Mod. Phys.*, 82:3045–3067, Nov 2010.

[21] Qin Liu, Chao-Xing Liu, Cenke Xu, Xiao-Liang Qi, and Shou-Cheng Zhang. Magnetic impurities on the surface of a topological insulator. *Phys. Rev. Lett.*, 102:156603, Apr 2009.

[22] Y L Chen, J-H Chu, J G Analytis, Z K Liu, K Igarashi, H-H Kuo, X L Qi, S K Mo, R G Moore, D H Lu, M Hashimoto, T Sasagawa, S C Zhang, I R Fisher, Z Hussain, and Z X Shen. Massive Dirac fermion on the surface of a magnetically doped topological insulator. *Science*, 329(5992):659–662, 2010.

[23] C. L. Kane and E. J. Mele. Quantum Spin Hall Effect in Graphene. *Phys. Rev. Lett.*, 95:226801, Nov 2005.

[24] S. M. Young, S. Zaheer, J. C. Y. Teo, C. L. Kane, E. J. Mele, and A. M. Rappe. Dirac semimetal in three dimensions. *Phys. Rev. Lett.*, 108:140405, Apr 2012.

[25] M. Zahid Hasan, Su-Yang Xu, and Madhab Neupane. *Topological Insulators, Topological Dirac semimetals, Topological Crystalline Insulators, and Topological Kondo Insulators*, pages 55–100. Wiley-VCH Verlag GmbH & Co. KGaA, 2015.

[26] Zhijun Wang, Hongming Weng, Quansheng Wu, Xi Dai, and Zhong Fang. Three-dimensional Dirac semimetal and quantum transport in Cd_3As_2. *Phys. Rev. B*, 88:125427, Sep 2013.

[27] Zhijun Wang, Yan Sun, Xing-Qiu Chen, Cesare Franchini, Gang Xu, Hongming Weng, Xi Dai, and Zhong Fang. Dirac semimetal and topological phase transitions in A_3Bi (A =Na, K, Rb). *Phys. Rev. B*, 85:195320, May 2012.

[28] Z. K. Liu, B. Zhou, Y. Zhang, Z. J. Wang, H. M. Weng, D. Prabhakaran, S.-K. Mo, Z. X. Shen, Z. Fang, X. Dai, Z. Hussain, and Y. L. Chen. Discovery of a Three-Dimensional Topological Dirac Semimetal, Na3Bi. *Science*, 343(6173):864–867, 2014.

[29] Madhab Neupane, Su Xu, Raman Sankar, Nasser Alidoust, Guang Bian, Chang Liu, Ilya Belopolski, Tay Chang, Horng Jeng, Hsin Lin, Arun Bansil, Fangcheng Chou, and M. Zahid Hasan. Observation of a three-dimensional topological Dirac semimetal phase in high-mobility Cd3As2. *Nat Commun*, 5, 2014.

[30] Z. K. Liu, J. Jiang, B. Zhou, Z. J. Wang, Y. Zhang, H. M. Weng, D. Prabhakaran, S-K. Mo, H. Peng, P. Dudin, T. Kim, M. Hoesch, Z. Fang, X. Dai, Z. X. Shen, D. L. Feng, Z. Hussain, and Y. L. Chen. A stable three-dimensional topological Dirac semimetal Cd_33As_2. *Nat Mater*, 13(7):677–681, 2014.

[31] Hemian Yi, Zhijun Wang, Chaoyu Chen, Youguo Shi, Ya Feng, Aiji Liang, Zhuojin Xie, Shaolong He, Junfeng He, Yingying Peng, Xu Liu, Yan Liu, Lin Zhao, Guodong Liu, Xiaoli Dong, Jun Zhang, M. Nakatake, M. Arita, K. Shimada, H. Namatame, M. Taniguchi, Zuyan Xu, Chuangtian Chen, Xi Dai, Zhong Fang, and X. J. Zhou. Evidence of Topological Surface State in Three-Dimensional Dirac Semimetal Cd3As2. *Sci. Rep.*, 4, 2014.

[32] Sergey Borisenko, Quinn Gibson, Danil Evtushinsky, Volodymyr Zabolotnyy, Bernd Büchner, and Robert J. Cava. Experimental Realization of a Three-Dimensional Dirac Semimetal. *Phys. Rev. Lett.*, 113:027603, Jul 2014.

[33] A. A. Burkov and Leon Balents. Weyl semimetal in a topological insulator multilayer. *Phys. Rev. Lett.*, 107:127205, Sep 2011.

[34] Oskar Vafek and Ashvin Vishwanath. Dirac Fermions in Solids: From High-Tc Cuprates and Graphene to Topological Insulators and Weyl Semimetals. *Annual Review of Condensed Matter Physics*, 5(1):83–112, 2014.

[35] Xiangang Wan, Ari M. Turner, Ashvin Vishwanath, and Sergey Y. Savrasov. Topological semimetal and Fermi-arc surface states in the electronic structure of pyrochlore iridates. *Phys. Rev. B*, 83:205101, May 2011.

[36] H.B. Nielsen and Masao Ninomiya. The Adler-Bell-Jackiw anomaly and Weyl fermions in a crystal. *Physics Letters B*, 130(6):389 – 396, 1983.

[37] Su-Yang Xu, Ilya Belopolski, Nasser Alidoust, Madhab Neupane, Guang Bian, Chenglong Zhang, Raman Sankar, Guoqing Chang, Zhujun Yuan, Chi-Cheng Lee, Shin-Ming Huang, Hao Zheng, Jie Ma, Daniel S. Sanchez, BaoKai Wang, Arun Bansil, Fangcheng Chou, Pavel P. Shibayev, Hsin Lin, Shuang Jia, and M. Zahid Hasan. Discovery of a Weyl fermion semimetal and topological Fermi arcs. *Science*, 349(6248):613–617, 2015.

[38] L. X. Yang, Z. K. Liu, Y. Sun, H. Peng, H. F. Yang, T. Zhang, B. Zhou, Y. Zhang, Y. F. Guo, M. Rahn, D. Prabhakaran, Z. Hussain, S. Mo, C. Felser, B. Yan, and Y. L. Chen. Weyl semimetal phase in the non-centrosymmetric compound TaAs. *Nat Phys*, 11:728–732, 2015.

[39] B. Q. Lv, N. Xu, H. M. Weng, J. Z. Ma, P. Richard, X. C. Huang, L. X. Zhao, G. F. Chen, C. E. Matt, F. Bisti, V. N. Strocov, J. Mesot, Z. Fang, X. Dai, T. Qian, M. Shi, and H. Ding. Observation of Weyl nodes in TaAs. *Nat Phys*, 11:724–727, 2015.

[40] B. Q. Lv, H. M. Weng, B. B. Fu, X. P. Wang, H. Miao, J. Ma, P. Richard, X. C. Huang, L. X. Zhao, G. F. Chen, Z. Fang, X. Dai, T. Qian, and H. Ding. Experimental Discovery of Weyl Semimetal TaAs. *Phys. Rev. X*, 5:031013, Jul 2015.

[41] Suyang Xu, Nasser Alidoust, Ilya Belopolski, Zhujun Yuan, Guang Bian, Tay Chang, Hao Zheng, Vladimir N. Strocov, Daniel S. Sanchez, Guoqing Chang, Chenglong Zhang, Daixiang Mou, Yun Wu, Lunan Huang, Chi Lee, Shin Huang, BaoKai Wang, Arun Bansil, Horng Jeng, Titus Neupert, Adam Kaminski, Hsin Lin, Shuang Jia, and M. Zahid Hasan. Discovery of a Weyl fermion state with Fermi arcs in niobium arsenide. *Nat Phys*, 11:748–754, 2015.

[42] Shin-Ming Huang, Su-Yang Xu, Ilya Belopolski, Chi-Cheng Lee, Guoqing Chang, BaoKai Wang, Nasser Alidoust, Guang Bian, Madhab Neupane, Chenglong Zhang, Shuang Jia, Arun Bansil, Hsin Lin, and M. Zahid Hasan. A Weyl Fermion semimetal with surface Fermi arcs in the transition metal monopnictide TaAs class. *Nat Commun*, 6:7373, 2015.

[43] Hongming Weng, Chen Fang, Zhong Fang, B. Andrei Bernevig, and Xi Dai. Weyl semimetal phase in noncentrosymmetric transition-metal monophosphides. *Phys. Rev. X*, 5:011029, Mar 2015.

[44] Alexey A Soluyanov, Dominik Gresch, Zhijun Wang, QuanSheng Wu, Matthias Troyer, Xi Dai, and B Andrei Bernevig. Type-II Weyl semimetals. *Nature*, 527(7579):495–8, 2015.

[45] Yan Sun, Shu-Chun Wu, Mazhar N. Ali, Claudia Felser, and Binghai Yan. Prediction of Weyl semimetal in orthorhombic $\mathrm{MoTe_2}$. *Phys. Rev. B*, 92:161107, Oct 2015.

[46] Tay-Rong Chang, Su-Yang Xu, Guoqing Chang, Chi-Cheng Lee, Shin-Ming Huang, BaoKai Wang, Guang Bian, Hao Zheng, Daniel S Sanchez, Ilya Belopolski, Nasser Alidoust, Madhab Neupane, Arun Bansil, Horng-Tay Jeng, Hsin Lin, and M Zahid Hasan. Prediction of an arc-tunable Weyl Fermion metallic state in MoxW1-xTe2. *Nat Commun*, 7(10639), feb 2016.

[47] Lunan Huang, Timothy M McCormick, Masayuki Ochi, Zhiying Zhao, Michi-To Suzuki, Ryotaro Arita, Yun Wu, Daixiang Mou, Huibo Cao, Jiaqiang Yan, et al. Spectroscopic evidence for a type II Weyl semimetallic state in MoTe2. *Nature Materials*, 2016.

[48] Ilya Belopolski, Su-Yang Xu, Yukiaki Ishida, Xingchen Pan, Peng Yu, Daniel S. Sanchez, Hao Zheng, Madhab Neupane, Nasser Alidoust, Guoqing Chang, Tay-Rong Chang, Yun Wu, Guang Bian, Shin-Ming Huang, Chi-Cheng Lee, Daixiang Mou, Lunan Huang, You Song, Baigeng Wang, Guanghou Wang, Yao-Wen Yeh, Nan Yao, Julien E. Rault, Patrick Le Fèvre, Fran çois Bertran, Horng-Tay Jeng, Takeshi Kondo, Adam Kaminski, Hsin Lin, Zheng Liu, Fengqi Song, Shik Shin, and M. Zahid Hasan. Fermi arc electronic structure

and Chern numbers in the type-II Weyl semimetal candidate $\mathrm{Mo}_x\mathrm{W}_{1-x}\mathrm{Te}_2$. *Phys. Rev. B*, 94:085127, Aug 2016.

[49] Yuanping Chen, Yuee Xie, Shengyuan A. Yang, Hui Pan, Fan Zhang, Marvin L. Cohen, and Shengbai Zhang.

[50] Gang Xu, Hongming Weng, Zhijun Wang, Xi Dai, and Zhong Fang. Chern Semimetal and the Quantized Anomalous Hall Effect in $\mathrm{HgCr}_2\mathrm{Se}_4$. *Phys. Rev. Lett.*, 107:186806, Oct 2011.

[51] Tom Bzduek, QuanSheng Wu, Andreas Regg, Manfred Sigrist, and Alexey A. Soluyanov. Nodal-chain metals. *Nature (London)*, advance online publication:–, 2016.

[52] Chen Fang, Hongming Weng, Xi Dai, and Zhong Fang. Topological nodal line semimetals. *arXiv preprint arXiv:1609.05414*, 2016.

[53] Guang Bian, Tay-Rong Chang, Raman Sankar, Su-Yang Xu, Hao Zheng, Titus Neupert, Ching-Kai Chiu, Shin-Ming Huang, Guoqing Chang, Ilya Belopolski, Daniel S Sanchez, Madhab Neupane, Nasser Alidoust, Chang Liu, BaoKai Wang, Chi-Cheng Lee, Horng-Tay Jeng, Chenglong Zhang, Zhujun Yuan, Shuang Jia, Arun Bansil, Fangcheng Chou, Hsin Lin, and M Zahid Hasan. Topological nodal-line fermions in spin-orbit metal PbTaSe2. *Nat Commun*, 7, feb 2016.

[54] Hongming Weng, Yunye Liang, Qiunan Xu, Rui Yu, Zhong Fang, Xi Dai, and Yoshiyuki Kawazoe. Topological node-line semimetal in three-dimensional graphene networks. *Phys. Rev. B*, 92:045108, Jul 2015.

[55] Minggang Zeng, Chen Fang, Guoqing Chang, Yu-An Chen, Timothy Hsieh, Arun Bansil, Hsin Lin, and Liang Fu. Topological semimetals and topological insulators in rare earth monopnictides. *arXiv preprint arXiv:1504.03492*, 2015.

[56] Leslie M. Schoop, Mazhar N. Ali, Carola Straszer, Andreas Topp, Andrei Varykhalov, Dmitry Marchenko, Viola Duppel, Stuart S. P. Parkin, Bettina V. Lotsch, and Chris-

tian R. Ast. Dirac cone protected by non-symmorphic symmetry and three-dimensional Dirac line node in ZrSiS. *Nat Commun*, 7:11696, 2016.

[57] H. Hertz. Ueber einen einfluss des ultravioletten lichtes auf die electrische entladung. *Annalen der Physik*, 267(8):983–1000, 1887.

[58] P. Lenard. Ueber die lichtelektrische wirkung. *Annalen der Physik*, 313(5):149–198, 1902.

[59] A. Einstein. ber einen die erzeugung und verwandlung des lichtes betreffenden heuristischen gesichtspunkt. *Annalen der Physik*, 322(6):132–148, 1905.

[60] Andrea Damascelli, Zahid Hussain, and Zhi-Xun Shen. Angle-resolved photoemission studies of the cuprate superconductors. *Rev. Mod. Phys.*, 75:473–541, 2003.

[61] Carl Nordling, Evelyn Sokolowski, and Kai Siegbahn. Precision method for obtaining absolute values of atomic binding energies. *Phys. Rev.*, 105:1676–1677, Mar 1957.

[62] Wikipedia. X-ray photoelectron spectroscopy — wikipedia, the free encyclopedia, 2016. [Online; accessed 17-September-2016].

[63] Andrea Damascelli. Probing the Electronic Structure of Complex Systems by ARPES. *Physica Scripta*, 2004(T109):61, 2004.

[64] M. P. Seah and W. A. Dench. Quantitative electron spectroscopy of surfaces: A standard data base for electron inelastic mean free paths in solids. *Surface and Interface Analysis*, 1(1):2–11, 1979.

[65] gammadata. *User's Guide VUV5000 Source.* gammadata.

[66] Chang Liu. *Electronic structure of iron arsenic high temperature superconductors studied by angle resolved photoemission spectroscopy (ARPES).* PhD thesis, Iowa State University, 2011.

[67] Eundeok Mun, Hyunjin Ko, Gordon J. Miller, German D. Samolyuk, Sergey L. Bud'ko, and Paul. C. Canfield. Magnetic field effects on transport properties of $PtSn_4$. *Phys. Rev. B*, 85:035135, Jan 2012.

[68] Wikipedia. Synchrotron radiation — wikipedia, the free encyclopedia, 2016. [Online; accessed 21-September-2016].

[69] Rui Jiang, Daixiang Mou, Yun Wu, Lunan Huang, Colin D. McMillen, Joseph Kolis, Henry G. Giesber, John J. Egan, and Adam Kaminski. Tunable vacuum ultraviolet laser based spectrometer for angle resolved photoemission spectroscopy. *Review of Scientific Instruments*, 85(3):–, 2014.

[70] H. Mirhosseini and J. Henk. Spin Texture and Circular Dichroism in Photoelectron Spectroscopy from the Topological Insulator Bi_2Te_3: First-Principles Photoemission Calculations. *Phys. Rev. Lett.*, 109:036803, Jul 2012.

[71] Rui Jiang. *Laser-based angle-resolved photoemission spectroscopy (ARPES) and studies of topological insulators and heavy fermions.* PhD thesis, Iowa State University, 2014.

[72] Gammadata Scienta AB. *The Gammadata Scienta SES-2002 User's Manual.* Gammadata Scienta AB.

[73] Na Hyun Jo, Udhara S. Kaluarachchi, Yun Wu, Daixiang Mou, Lunan Huang, Valentin Taufour, Adam Kaminski, Sergey L. Bud'ko, and Paul C. Canfield. Anisotropic physical properties and pressure dependent magnetic ordering of $CrAuTe_4$. *Phys. Rev. B*, 94:184413, Nov 2016.

[74] L.W. Yang and G. Thummes. High frequency two-stage pulse tube cryocooler with base temperature below 20 K. *Cryogenics*, 45(2):155 – 159, 2005.

[75] PT415 Cryorefrigerator with Remote Motor Option, 2016. [Online; accessed 23-September-2016].

[76] Udhara S. Kaluarachchi, Weiwei Xie, Qisheng Lin, Valentin Taufour, Sergey L. Bud'ko, Gordon J. Miller, and Paul C. Canfield. Superconductivity versus structural phase transition in the closely related $Bi_2Rh_{3.5}S_2$ and $Bi_2Rh_3S_2$. *Phys. Rev. B*, 91:174513, May 2015.

[77] Leslie M. Schoop, Lilia S. Xie, Ru Chen, Quinn D. Gibson, Saul H. Lapidus, Itamar Kimchi, Max Hirschberger, Neel Haldolaarachchige, Mazhar N. Ali, Carina A. Belvin, Tian Liang, Jeffrey B. Neaton, N. P. Ong, Ashvin Vishwanath, and R. J. Cava. Dirac metal to topological metal transition at a structural phase change in Au_2Pb and prediction of Z_2 topology for the superconductor. *Phys. Rev. B*, 91:214517, Jun 2015.

[78] Y. Xia, D. Qian, D. Hsieh, L. Wray, A. Pal, H. Lin, A. Bansil, D. Grauer, Y. S. Hor, R. J. Cava, and M. Z. Hasan. Observation of a large-gap topological-insulator class with a single Dirac cone on the surface. *Nat. Phys.*, 5(6):398–402, 2009.

[79] A. Narayanan, M. D. Watson, S. F. Blake, N. Bruyant, L. Drigo, Y. L. Chen, D. Prabhakaran, B. Yan, C. Felser, T. Kong, P. C. Canfield, and A. I. Coldea. Linear Magnetoresistance Caused by Mobility Fluctuations in n-Doped $\mathrm{Cd_3As_2}$. *Phys. Rev. Lett.*, 114:117201, Mar 2015.

[80] Su-Yang Xu, Ilya Belopolski, Daniel S. Sanchez, Chenglong Zhang, Guoqing Chang, Cheng Guo, Guang Bian, Zhujun Yuan, Hong Lu, Tay-Rong Chang, Pavel P. Shibayev, Mykhailo L. Prokopovych, Nasser Alidoust, Hao Zheng, Chi-Cheng Lee, Shin-Ming Huang, Raman Sankar, Fangcheng Chou, Chuang-Han Hsu, Horng-Tay Jeng, Arun Bansil, Titus Neupert, Vladimir N. Strocov, Hsin Lin, Shuang Jia, and M. Zahid Hasan. Experimental discovery of a topological Weyl semimetal state in TaP. *Science Advances*, 1(10), 2015.

[81] F. Y. Bruno, A. Tamai, Q. S. Wu, I. Cucchi, C. Barreteau, A. de la Torre, S. McKeown Walker, S. Riccò, Z. Wang, T. K. Kim, M. Hoesch, M. Shi, N. C. Plumb, E. Giannini, A. A. Soluyanov, and F. Baumberger. Observation of large topologically trivial Fermi arcs in the candidate type-II Weyl semimetal $\mathrm{WTe_2}$. *Phys. Rev. B*, 94:121112, Sep 2016.

[82] Chenlu Wang, Yan Zhang, Jianwei Huang, Simin Nie, Guodong Liu, Aiji Liang, Yuxiao Zhang, Bing Shen, Jing Liu, Cheng Hu, Ying Ding, Defa Liu, Yong Hu, Shaolong He, Lin Zhao, Li Yu, Jin Hu, Jiang Wei, Zhiqiang Mao, Youguo Shi, Xiaowen Jia, Fengfeng Zhang, Shenjin Zhang, Feng Yang, Zhimin Wang, Qinjun Peng, Hongming Weng, Xi Dai,

Zhong Fang, Zuyan Xu, Chuangtian Chen, and X.J. Zhou. Spectroscopic Evidence of Type II Weyl Semimetal State in WTe2. pages 1–16, 2016.

[83] Yun Wu, Daixiang Mou, Na Hyun Jo, Kewei Sun, Lunan Huang, S. L. Bud'ko, P. C. Canfield, and Adam Kaminski. Observation of Fermi arcs in the type-II Weyl semimetal candidate WTe_2. *Phys. Rev. B*, 94:121113, Sep 2016.

[84] Yun Wu, Na Hyun Jo, Masayuki Ochi, Lunan Huang, Daixiang Mou, Sergey L. Bud'ko, P. C. Canfield, Nandini Trivedi, Ryotaro Arita, and Adam Kaminski. Temperature-Induced Lifshitz Transition in WTe_2. *Phys. Rev. Lett.*, 115:166602, Oct 2015.

[85] Sergey Borisenko, Daniil Evtushinsky, Quinn Gibson, Alexander Yaresko, Timur Kim, M. N. Ali, Bernd Buechner, Moritz Hoesch, and Robert J. Cava. Time-Reversal Symmetry Breaking Type-II Weyl State in YbMnBi2. *arXiv preprint arXiv:1507.04847v2*, 2015.

[86] Su-Yang Xu, Nasser Alidoust, Guoqing Chang, Hong Lu, Bahadur Singh, Ilya Belopolski, Daniel Sanchez, Xiao Zhang, Guang Bian, Hao Zheng, et al. Discovery of Lorentz-violating Weyl fermion semimetal state in LaAlGe materials. *arXiv preprint arXiv:1603.07318*, 2016.

[87] Leslie M Schoop, Mazhar N Ali, Carola Straßer, Viola Duppel, Stuart SP Parkin, Bettina V Lotsch, and Christian R Ast. Dirac Cone Protected by Non-Symmorphic Symmetry and 3D Dirac Line Node in ZrSiS. *arXiv preprint arXiv:1509.00861*, 2015.

[88] Fazel Fallah Tafti, Quinn Gibson, Satya Kushwaha, Jason W. Krizan, Neel Haldolaarachchige, and Robert Joseph Cava. Temperaturefield phase diagram of extreme magnetoresistance. *Proceedings of the National Academy of Sciences*, 113(25):E3475–E3481, 2016.

[89] Shanshan Sun, Qi Wang, Peng-Jie Guo, Kai Liu, and Hechang Lei. Large magnetoresistance in LaBi: origin of field-induced resistivity upturn and plateau in compensated semimetals. *New Journal of Physics*, 18(8):082002, 2016.

[90] Nitesh Kumar, Chandra Shekhar, Shu-Chun Wu, Inge Leermakers, Olga Young, Uli Zeitler, Binghai Yan, and Claudia Felser. Observation of pseudo-two-dimensional electron transport in the rock salt-type topological semimetal LaBi. *Phys. Rev. B*, 93:241106, Jun 2016.

[91] Peng-Jie Guo, Huan-Cheng Yang, Bing-Jing Zhang, Kai Liu, and Zhong-Yi Lu. Charge compensation in extremely large magnetoresistance materials LaSb and LaBi revealed by first-principles calculations. *Phys. Rev. B*, 93:235142, Jun 2016.

[92] P. C. Canfield and Z. Fisk. Growth of single crystals from metallic fluxes. *Philosophical Magazine Part B*, 65(6):1117–1123, 1992.

[93] Paul C. Canfield, Tai Kong, Udhara S. Kaluarachchi, and Na Hyun Jo. Use of frit-disc crucibles for routine and exploratory solution growth of single crystalline samples. *Philosophical Magazine*, 96(1):84–92, 2016.

[94] P. Hohenberg and W. Kohn. Inhomogeneous electron gas. *Phys. Rev.*, 136:B864–B871, Nov 1964.

[95] W. Kohn and L. J. Sham. Self-consistent equations including exchange and correlation effects. *Phys. Rev.*, 140:A1133–A1138, Nov 1965.

[96] G. Kresse and J. Furthmüller. Efficient iterative schemes for *ab initio* total-energy calculations using a plane-wave basis set. *Phys. Rev. B*, 54:11169–11186, Oct 1996.

[97] G. Kresse and J. Furthmller. Efficiency of ab-initio total energy calculations for metals and semiconductors using a plane-wave basis set. *Computational Materials Science*, 6(1):15 – 50, 1996.

[98] John P. Perdew, Kieron Burke, and Matthias Ernzerhof. Generalized gradient approximation made simple. *Phys. Rev. Lett.*, 77:3865–3868, Oct 1996.

[99] P. E. Blöchl. Projector augmented-wave method. *Phys. Rev. B*, 50:17953–17979, Dec 1994.

[100] Mazhar N. Ali, Jun Xiong, Steven Flynn, Jing Tao, Quinn D. Gibson, Leslie M. Schoop, Tian Liang, Neel Haldolaarachchige, Max Hirschberger, N. P. Ong, and R. J. Cava. Large, non-saturating magnetoresistance in WTe2. *Nature (London)*, 514:205–208, 2014.

[101] Yoshinori Okada, Maksym Serbyn, Hsin Lin, Daniel Walkup, Wenwen Zhou, Chetan Dhital, Madhab Neupane, Suyang Xu, Yung Jui Wang, R. Sankar, Fangcheng Chou, Arun Bansil, M. Zahid Hasan, Stephen D. Wilson, Liang Fu, and Vidya Madhavan. Observation of Dirac Node Formation and Mass Acquisition in a Topological Crystalline Insulator. *Science*, 341(6153):1496–1499, 2013.

[102] Ilija Zeljkovic, Yoshinori Okada, Cheng Huang, R. Sankar, Daniel Walkup, Wenwen Zhou, Maksym Serbyn, Fangcheng Chou, Wei Tsai, Hsin Lin, A. Bansil, Liang Fu, M. Zahid Hasan, and Vidya Madhavan. Mapping the unconventional orbital texture in topological crystalline insulators. *Nat Phys*, 10:572–577, 2014.

[103] Chang Liu, Takeshi Kondo, Rafael M. Fernandes, Ari D. Palczewski, Eun Deok Mun, Ni Ni, Alexander N. Thaler, Aaron Bostwick, Eli Rotenberg, Jorg Schmalian, Sergey L. Bud/'ko, Paul C. Canfield, and Adam Kaminski. Evidence for a Lifshitz transition in electron-doped iron arsenic superconductors at the onset of superconductivity. *Nat Phys*, 6:419–423, 2010.

[104] Chang Liu, A. D. Palczewski, R. S. Dhaka, Takeshi Kondo, R. M. Fernandes, E. D. Mun, H. Hodovanets, A. N. Thaler, J. Schmalian, S. L. Bud'ko, P. C. Canfield, and A. Kaminski. Importance of the Fermi-surface topology to the superconducting state of the electron-doped pnictide $\mathrm{Ba(Fe_{1-x}Co_x)_2As_2}$. *Phys. Rev. B*, 84:020509, Jul 2011.

[105] SL Bud'ko, AN Voronovskii, AG Gapotechenko, and ES Itskevich. The Fermi surface of cadmium at an electron-topological phase transition under pressure. *Sov. Phys. JETP*, 59(2):454–457, 1984.

[106] Defen Kang, Yazhou Zhou, Wei Yi, Chongli Yang, Jing Guo, Youguo Shi, Shan Zhang, Zhe Wang, Chao Zhang, Sheng Jiang, Aiguo Li, Ke Yang, Qi Wu, Guangming Zhang,

Liling Sun, and Zhongxian Zhao. Superconductivity emerging from a suppressed large magnetoresistant state in tungsten ditelluride. *Nat Commun*, 6, 2015.

[107] M. N. Baibich, J. M. Broto, A. Fert, F. Nguyen Van Dau, F. Petroff, P. Etienne, G. Creuzet, A. Friederich, and J. Chazelas. Giant Magnetoresistance of (001)Fe/(001)Cr Magnetic Superlattices. *Phys. Rev. Lett.*, 61:2472–2475, Nov 1988.

[108] G. Binasch, P. Grünberg, F. Saurenbach, and W. Zinn. Enhanced magnetoresistance in layered magnetic structures with antiferromagnetic interlayer exchange. *Phys. Rev. B*, 39:4828–4830, Mar 1989.

[109] A. Urushibara, Y. Moritomo, T. Arima, A. Asamitsu, G. Kido, and Y. Tokura. Insulator-metal transition and giant magnetoresistance in $\mathrm{La}_{1-x}\mathrm{Sr}_x\mathrm{MnO}_3$. *Phys. Rev. B*, 51:14103–14109, May 1995.

[110] Y. Moritomo, A. Asamitsu, H. Kuwahara, and Y. Tokura. Giant magnetoresistance of manganese oxides with a layered perovskite structure. *Nature (London)*, 380:141–144, 1996.

[111] A. P. Ramirez, R. J. Cava, and J. Krajewski. Colossal magnetoresistance in Cr-based chalcogenide spinels. *Nature (London)*, 386:156–159, 1997.

[112] J.M. Daughton. {GMR} applications. *Journal of Magnetism and Magnetic Materials*, 192(2):334 – 342, 1999.

[113] Tian Liang, Quinn Gibson, Mazhar N. Ali, Minhao Liu, R. J. Cava, and N. P. Ong. Ultrahigh mobility and giant magnetoresistance in the Dirac semimetalCd3As2. *Nat Mater*, 14:280–284, 2015.

[114] Kefeng Wang, D. Graf, Lijun Li, Limin Wang, and C. Petrovic. Anisotropic giant magnetoresistance in NbSb2. *Sci. Rep.*, 4:7328, 2014.

[115] Yanfei Zhao, Haiwen Liu, Jiaqiang Yan, Wei An, Jun Liu, Xi Zhang, Huichao Wang, Yi Liu, Hua Jiang, Qing Li, Yong Wang, Xin-Zheng Li, David Mandrus, X. C. Xie,

Minghu Pan, and Jian Wang. Anisotropic magnetotransport and exotic longitudinal linear magnetoresistance in $\mathrm{WTe_2}$ crystals. *Phys. Rev. B*, 92:041104, Jul 2015.

[116] L. R. Thoutam, Y. L. Wang, Z. L. Xiao, S. Das, A. Luican-Mayer, R. Divan, G. W. Crabtree, and W. K. Kwok. Temperature-Dependent Three-Dimensional Anisotropy of the Magnetoresistance in $\mathrm{WTe_2}$. *Phys. Rev. Lett.*, 115:046602, Jul 2015.

[117] Xing-Chen Pan, Yiming Pan, Juan Jiang, Huakun Zuo, Huimei Liu, Xuliang Chen, Zhongxia Wei, Shuai Zhang, Zhihe Wang, Xiangang Wan, et al. Robust linear magnetoresistance in WTe2. *arXiv preprint arXiv:1505.07968*, 2015.

[118] I. Pletikosic, Mazhar N. Ali, A.$\tilde{\mathrm{V}}$. Fedorov, R.$\tilde{\mathrm{J}}$. Cava, and T. Valla. Electronic Structure Basis for the Extraordinary Magnetoresistance in $\mathrm{WTe_2}$. *Phys. Rev. Lett.*, 113:216601, Nov 2014.

[119] P. S. Alekseev, A. P. Dmitriev, I. V. Gornyi, V. Yu. Kachorovskii, B. N. Narozhny, M. Schütt, and M. Titov. Magnetoresistance in two-component systems. *Phys. Rev. Lett.*, 114:156601, Apr 2015.

[120] Shigeharu Kabashima. Electrical Properties of Tungsten-Ditelluride WTe2. *Journal of the Physical Society of Japan*, 21(5):945–948, 1966.

[121] L.H. Brixner. Preparation and properties of the single crystalline AB2-type selenides and tellurides of niobium, tantalum, molybdenum and tungsten. *Journal of Inorganic and Nuclear Chemistry*, 24(3):257 – 263, 1962.

[122] J. Augustin, V. Eyert, Th. Böker, W. Frentrup, H. Dwelk, C. Janowitz, and R. Manzke. Electronic band structure of the layered compound $\mathrm{Td}-\mathrm{WTe_2}$. *Phys. Rev. B*, 62:10812–10823, Oct 2000.

[123] Zengwei Zhu, Xiao Lin, Juan Liu, Benoît Fauqué, Qian Tao, Chongli Yang, Youguo Shi, and Kamran Behnia. Quantum Oscillations, Thermoelectric Coefficients, and the Fermi Surface of Semimetallic $\mathrm{WTe_2}$. *Phys. Rev. Lett.*, 114:176601, Apr 2015.

[124] Fei-Xiang Xiang, Menno Veldhorst, Shi-Xue Dou, and Xiao-Lin Wang. Multiple Fermi pockets revealed by Shubnikov-de Haas oscillations in WTe2. *EPL (Europhysics Letters)*, 112(3):37009, 2015.

[125] P. L. Cai, J. Hu, L. P. He, J. Pan, X. C. Hong, Z. Zhang, J. Zhang, J. Wei, Z. Q. Mao, and S. Y. Li. Drastic Pressure Effect on the Extremely Large Magnetoresistance in WTe_2: Quantum Oscillation Study. *Phys. Rev. Lett.*, 115:057202, Jul 2015.

[126] J. Jiang, F. Tang, X. C. Pan, H. M. Liu, X. H. Niu, Y. X. Wang, D. F. Xu, H. F. Yang, B. P. Xie, F. Q. Song, P. Dudin, T. K. Kim, M. Hoesch, P. Kumar Das, I. Vobornik, X. G. Wan, and D. L. Feng. Signature of Strong Spin-Orbital Coupling in the Large Nonsaturating Magnetoresistance Material WTe_2. *Phys. Rev. Lett.*, 115:166601, Oct 2015.

[127] B. E. Brown. The crystal structures of WTe_2 and high-temperature $MoTe_2$. *Acta Crystallographica*, 20(2):268–274, Feb 1966.

[128] Eundeok Mun, Sergey L Bud'ko, Milton S Torikachvili, and Paul C Canfield. Experimental setup for the measurement of the thermoelectric power in zero and applied magnetic field. *Measurement Science and Technology*, 21(5):055104, 2010.

[129] P. Blaha, K. Schwarz, G. K. H. Madsen, D. Kvasnicka, and J. Luitz. *WIEN2K, An Augmented Plane Wave + Local Orbitals Program for Calculating Crystal Properties.* Karlheinz Schwarz, Techn. Universität Wien, Austria, 2001.

[130] Arthur Mar, Stephane Jobic, and James A. Ibers. Metal-metal vs tellurium-tellurium bonding in WTe_2 and its ternary variants $TaIrTe_4$ and $NbIrTe_4$. *Journal of the American Chemical Society*, 114(23):8963–8971, 1992.

[131] Georg K.H. Madsen and David J. Singh. BoltzTraP. A code for calculating band-structure dependent quantities. *Computer Physics Communications*, 175(1):67 – 71, 2006.

[132] A. K. Geim and K. S. Novoselov. The rise of graphene. *Nat Mater*, 6:183–191, 2007.

[133] A.A. Varlamov, V.S. Egorov, and A.V. Pantsulaya. Kinetic properties of metals near electronic topological transitions (2 1/2-order transitions). *Advances in Physics*, 38(5):469–564, 1989.

[134] Ronald Derrick Barnard. *Thermoelectricity in metals and alloys.* Halsted Press, 1972.

[135] R. S. Dhaka, S. E. Hahn, E. Razzoli, Rui Jiang, M. Shi, B. N. Harmon, A. Thaler, S. L. Bud'ko, P. C. Canfield, and Adam Kaminski. Unusual Temperature Dependence of Band Dispersion in $\mathrm{Ba(Fe_{1-x}Ru_x)_2As_2}$ and its Consequences for Antiferromagnetic Ordering. *Phys. Rev. Lett.*, 110:067002, Feb 2013.

[136] V. Brouet, Ping-Hui Lin, Y. Texier, J. Bobroff, A. Taleb-Ibrahimi, P. Le Fèvre, F. Bertran, M. Casula, P. Werner, S. Biermann, F. Rullier-Albenque, A. Forget, and D. Colson. Large Temperature Dependence of the Number of Carriers in Co-Doped $\mathrm{BaFe_2As_2}$. *Phys. Rev. Lett.*, 110:167002, Apr 2013.

[137] Xiao-Liang Qi and Shou-Cheng Zhang. Topological insulators and superconductors. *Rev. Mod. Phys.*, 83:1057–1110, Oct 2011.

[138] Su-Yang Xu, Chang Liu, Satya K. Kushwaha, Raman Sankar, Jason W. Krizan, Ilya Belopolski, Madhab Neupane, Guang Bian, Nasser Alidoust, Tay-Rong Chang, Horng-Tay Jeng, Cheng-Yi Huang, Wei-Feng Tsai, Hsin Lin, Pavel P. Shibayev, Fang-Cheng Chou, Robert J. Cava, and M. Zahid Hasan. Observation of Fermi arc surface states in a topological metal. *Science*, 347(6219):294–298, 2015.

[139] Hermann Weyl. Elektron und gravitation. i. *Zeitschrift fr Physik*, 56(5-6):330–352, 1929.

[140] Zhijun Wang, Dominik Gresch, Alexey A Soluyanov, Weiwei Xie, S Kushwaha, Xi Dai, Matthias Troyer, Robert J Cava, and B Andrei Bernevig. MoTe2: Weyl and Line Node Topological Metal. *arXiv preprint arXiv:1511.07440*, 2015.

[141] Tay-Rong Chang, Su-Yang Xu, Guoqing Chang, Chi-Cheng Lee, Shin-Ming Huang, BaoKai Wang, Guang Bian, Hao Zheng, Daniel S Sanchez, Ilya Belopolski, et al. Arc-

tunable Weyl Fermion metallic state in Mo _x W _$\{1 - x\}$ Te _2. *arXiv preprint arXiv:1508.06723*, 2015.

[142] Ilya Belopolski, Su-Yang Xu, Yukiaki Ishida, Xingchen Pan, Peng Yu, Daniel S Sanchez, Madhab Neupane, Nasser Alidoust, Guoqing Chang, Tay-Rong Chang, et al. Unoccupied electronic structure and signatures of topological Fermi arcs in the Weyl semimetal candidate Mo _x W _$\{1 - x\}$ Te _2. *arXiv preprint arXiv:1512.09099*, 2015.

[143] Timothy M. McCormick, Itamar Kimchi, and Nandini Trivedi. Minimal models for topological Weyl semimetals. pages 1–13, 2016.

[144] Ke Deng, Guoliang Wan, Peng Deng, Kenan Zhang, Shijie Ding, Eryin Wang, Mingzhe Yan, Huaqing Huang, Hongyun Zhang, Zhilin Xu, et al. Experimental observation of topological Fermi arcs in type-II Weyl semimetal MoTe2. *arXiv preprint arXiv:1603.08508*, 2016.

[145] J Jiang, ZK Liu, Y Sun, HF Yang, R Rajamathi, YP Qi, LX Yang, C Chen, H Peng, C-C Hwang, et al. Observation of the Type-II Weyl Semimetal Phase in MoTe2. *arXiv preprint arXiv:1604.00139*, 2016.

[146] Aiji Liang, Jianwei Huang, Simin Nie, Ying Ding, Qiang Gao, Cheng Hu, Shaolong He, Yuxiao Zhang, Chenlu Wang, Bing Shen, et al. Electronic Evidence for Type II Weyl Semimetal State in MoTe2. *arXiv preprint arXiv:1604.01706*, 2016.

[147] N Xu, ZJ Wang, AP Weber, A Magrez, P Bugnon, H Berger, CE Matt, JZ Ma, BB Fu, BQ Lv, et al. Discovery of Weyl semimetal state violating Lorentz invariance in MoTe2. *arXiv preprint arXiv:1604.02116*, 2016.

[148] Yun Wu, Lin-Lin Wang, Eundeok Mun, D D Johnson, Daixiang Mou, Lunan Huang, Yongbin Lee, S L Bud/'ko, P C Canfield, and Adam Kaminski. Dirac node arcs in PtSn4. *Nat Phys*, 12:667, apr 2016.

[149] Xingchen Pan, Xuliang Chen, Huimei Liu, Yanqing Feng, Zhongxia Wei, Yonghui Zhou, Zhenhua Chi, Li Pi, Fei Yen, Fengqi Song, Xiangang Wan, Zhaorong Yang, Baigeng Wang,

Guanghou Wang, and Yuheng Zhang. Pressure-driven dome-shaped superconductivity and electronic structural evolution in tungsten ditelluride. *Nat Commun*, 6, 2015.

[150] J. Jiang, F. Tang, X. C. Pan, H. M. Liu, X. H. Niu, Y. X. Wang, D. F. Xu, H. F. Yang, B. P. Xie, F. Q. Song, P. Dudin, T. K. Kim, M. Hoesch, P. Kumar Das, I. Vobornik, X. G. Wan, and D. L. Feng. Signature of Strong Spin-Orbital Coupling in the Large Nonsaturating Magnetoresistance Material WTe_2. *Phys. Rev. Lett.*, 115:166601, Oct 2015.

[151] Baojie Feng, Yang-Hao Chan, Ya Feng, Ro-Ya Liu, Mei-Yin Chou, Kenta Kuroda, Koichiro Yaji, Ayumi Harasawa, Paolo Moras, Alexei Barinov, et al. Spin Texture in Type-II Weyl Semimetal WTe2. *arXiv preprint arXiv:1606.00085*, 2016.

[152] Ilya Belopolski, Su-Yang Xu, Yukiaki Ishida, Xingchen Pan, Peng Yu, Daniel S. Sanchez, Hao Zheng, Madhab Neupane, Nasser Alidoust, Guoqing Chang, Tay-Rong Chang, Yun Wu, Guang Bian, Shin-Ming Huang, Chi-Cheng Lee, Daixiang Mou, Lunan Huang, You Song, Baigeng Wang, Guanghou Wang, Yao-Wen Yeh, Nan Yao, Julien E. Rault, Patrick Le Fèvre, Fran çois Bertran, Horng-Tay Jeng, Takeshi Kondo, Adam Kaminski, Hsin Lin, Zheng Liu, Fengqi Song, Shik Shin, and M. Zahid Hasan. Fermi arc electronic structure and Chern numbers in the type-II Weyl semimetal candidate $\mathrm{Mo}_x\mathrm{W}_{1-x}\mathrm{Te}_2$. *Phys. Rev. B*, 94:085127, Aug 2016.

[153] A. Tamai, Q. S. Wu, I. Cucchi, F. Y. Bruno, S. Riccò, T. K. Kim, M. Hoesch, C. Barreteau, E. Giannini, C. Besnard, A. A. Soluyanov, and F. Baumberger. Fermi Arcs and Their Topological Character in the Candidate Type-II Weyl Semimetal MoTe_2. *Phys. Rev. X*, 6:031021, Aug 2016.

[154] J. C. Campuzano, M. R. Norman, and M. Randeria. *The Physics of Superconductors*, volume II. Springer, Berlin, 2004.

[155] L. R. Thoutam, Y. L. Wang, Z. L. Xiao, S. Das, A. Luican-Mayer, R. Divan, G. W. Crabtree, and W. K. Kwok. Temperature-Dependent Three-Dimensional Anisotropy of the Magnetoresistance in WTe_2. *Phys. Rev. Lett.*, 115:046602, Jul 2015.

[156] Yun Wu, Na Hyun Jo, Masayuki Ochi, Lunan Huang, Daixiang Mou, Sergey L. Bud'ko, P. C. Canfield, Nandini Trivedi, Ryotaro Arita, and Adam Kaminski. Temperature-Induced Lifshitz Transition in WTe_2. *Phys. Rev. Lett.*, 115:166602, Oct 2015.

[157] A. A. Burkov, M. D. Hook, and Leon Balents. Topological nodal semimetals. *Phys. Rev. B*, 84:235126, Dec 2011.

[158] T.T. Heikkil and G.E. Volovik. Dimensional crossover in topological matter: Evolution of the multiple Dirac point in the layered system to the flat band on the surface. *JETP Letters*, 93(2):59–65, 2011.

[159] Minggang Zeng, Chen Fang, Guoqing Chang, Yu-An Chen, Timothy Hsieh, Arun Bansil, Hsin Lin, and Liang Fu. Topological semimetals and topological insulators in rare earth monopnictides. *arXiv preprint arXiv:1504.03492*, 2015.

[160] Rui Yu, Hongming Weng, Zhong Fang, Xi Dai, and Xiao Hu. Topological Node-Line Semimetal and Dirac Semimetal State in Antiperovskite $\mathrm{Cu}_3\mathrm{PdN}$. *Phys. Rev. Lett.*, 115:036807, Jul 2015.

[161] Youngkuk Kim, Benjamin J. Wieder, C. L. Kane, and Andrew M. Rappe. Dirac line nodes in inversion-symmetric crystals. *Phys. Rev. Lett.*, 115:036806, Jul 2015.

[162] Chen Fang, Yige Chen, Hae-Young Kee, and Liang Fu. Topological nodal line semimetals with and without spin-orbital coupling. *Phys. Rev. B*, 92:081201, Aug 2015.

[163] Guang Bian, Tay-Rong Chang, Hao Zheng, Saavanth Velury, Su-Yang Xu, Titus Neupert, Ching-Kai Chiu, Daniel S Sanchez, Ilya Belopolski, Nasser Alidoust, et al. Drumhead Surface States and Topological Nodal-Line Fermions in TlTaSe2. *arXiv preprint arXiv:1508.07521*, 2015.

[164] Lilia S. Xie, Leslie M. Schoop, Elizabeth M. Seibel, Quinn D. Gibson, Weiwei Xie, and Robert J. Cava. A new form of Ca3P2 with a ring of Dirac nodes. *APL Mater.*, 3(8), 2015.

[165] Ai Yamakage, Youichi Yamakawa, Yukio Tanaka, and Yoshihiko Okamoto. Line-Node Dirac Semimetal and Topological Insulating Phase in Noncentrosymmetric Pnictides CaAgX (X = P, As). *Journal of the Physical Society of Japan*, 85(1):013708, 2016.

[166] Chandra Shekhar, Ajaya K. Nayak, Yan Sun, Marcus Schmidt, Michael Nicklas, Inge Leermakers, Uli Zeitler, Yurii Skourski, Jochen Wosnitza, Zhongkai Liu, Yulin Chen, Walter Schnelle, Horst Borrmann, Yuri Grin, Claudia Felser, and Binghai Yan. Extremely large magnetoresistance and ultrahigh mobility in the topological Weyl semimetal candidate NbP. *Nat Phys*, 11:645–649, 2015.

[167] Hendrik J. Monkhorst and James D. Pack. Special points for Brillouin-zone integrations. *Phys. Rev. B*, 13:5188–5192, Jun 1976.

[168] Bernd Knnen, Dirk Niepmann, and Wolfgang Jeitschko. Structure refinements and some properties of the transition metal stannides Os3Sn7, Ir5Sn7, Ni0.402(4)Pd0.598Sn4, -PdSn2 and PtSn4. *Journal of Alloys and Compounds*, 309(12):1 – 9, 2000.